Factors Influencing Meiotic Recombination Revealed by Whole Genome Sequencing of Single Sperm◆

Authors: Anjali Gupta Hinch[1,#], Gang Zhang[1,#], Philipp W Becker[1], Daniela Moralli[1], Robert Hinch[1,2], Benjamin Davies[1], Rory Bowden[1], Peter Donnelly[1,3,*]

Affiliations:

[1]Wellcome Centre for Human Genetics, University of Oxford, Oxford, UK

[2]Big Data Institute, University of Oxford, Oxford, UK

[3]Department of Statistics, University of Oxford, Oxford, UK

[*] Corresponding author. Email: donnelly@well.ox.ac.uk

[#] These authors contributed equally to this work

Abstract: Recombination is critical to meiosis and evolution, yet many aspects of the physical exchange of DNA via crossovers remain poorly understood. We report an approach for single-cell whole-genome DNA sequencing and sequence 217 individual hybrid mouse sperm, providing a kilobase-resolution genome-wide map of crossovers. Combining this map with molecular assays measuring stages of recombination, we identify factors that affect crossover probability, including PRDM9 binding on the non-initiating template homologue and telomere proximity. These factors also influence the time for sites of recombination-initiating DNA double-strand breaks to find and engage their homologues, with rapidly-engaging sites more likely to form crossovers. We show that chromatin environment on the template homologue affects positioning of crossover breakpoints and provide insights into recombination in the pseudoautosomal region.

One Sentence Summary: Molecular assays of initiation combined with a high-resolution map of crossovers identifies key determinants of meiotic recombination outcomes.

Main Text: Recombination is a fundamental component of meiosis, the process that creates gametes in sexually reproducing organisms, and ensures the correct segregation of homologous chromosomes into daughter cells (*1*). Along with mutation, it shapes patterns of genetic variation in populations, providing the substrate for natural selection.

In many species, recombination events occur mainly in narrow regions of the genome called recombination hotspots (*2*). In humans, mice, cattle, and likely many other vertebrates (*3*), an early step in recombination is the binding of DNA by the histone methyl transferase PRDM9 (*2*). A subset of PRDM9 binding sites are subject to the formation of programmed double-strand breaks (DSBs). These breaks are repaired by a specialized pathway, which involves the meiosis-specific protein DMC1, and uses the homologous chromosome as the template for repairing the break (*1*). How the correct

---

◆This manuscript has been accepted for publication in Science. This version has not undergone final editing. Please refer to the complete version of record at http://www.sciencemag.org/. The manuscript may not be reproduced or used in any manner that does not fall within the fair use provisions of the Copyright Act without the prior, written permission of AAAS.

homologous sequence is located efficiently amongst the bulk of chromatin-embedded nuclear DNA remains unclear (*4*). A subset of the breaks repaired via the homologue become crossovers, whilst the majority resolve without a crossover (*5*). Any remaining DSBs are likely repaired using the sister chromatid as template (*6*). Despite its fundamental importance, critical aspects of the meiotic recombination process remain poorly understood.

Most mammals make only a few crossovers per chromosome (*7*), even though the number of DSBs is substantially greater (*8*). This raises the question of how the cell determines which DSBs will be repaired as crossovers. While it is clear that not all DSBs are equally likely to resolve as a crossover (*9-13*), the factors affecting this decision remain largely unknown. Improper crossing-over leads to aneuploidy, which affects 20-30% of human eggs and 1-8% of human sperm (*14*).

There are currently two major challenges to understanding crossover formation. Firstly, pedigree-based maps in humans and mice only localize crossovers within tens to hundreds of kilobases (*15-17*). Cytological assays are informative about the staging of meiotic events (*18*), but crossovers can only be placed within large domains containing dozens if not hundreds of hotspots. An alternative approach, identifying recombinant molecules in sperm at targeted sites, has high precision but is limited to a small number of selected hotspots (*10*, *19*, *20*). Whole genome sequencing of single sperm can identify crossovers genome-wide, however existing methods have low resolution (*21*, *22*). Secondly, analyses of genetic maps can be complicated by allelic variation in *Prdm9*, which leads to distinct sets of hotspots, within and between populations (*17*, *23*, *24*). This makes it difficult to connect the initiation of recombination with the final outcome of crossovers.

A single-cell DNA sequencing method to identify crossovers in individual sperm

We have developed a method for amplifying and sequencing DNA from single cells, and applied it to sperm to identify crossovers with high resolution (*25*). We isolate a cell mechanically and amplify its DNA using RNA random priming and Klenow fragment synthesis (Fig. 1A, (*25*)). Our method achieves uniform coverage, with regions missed randomly, rather than systematically due to genomic features (Figs. S1-2).

This approach was applied to 217 sperm cells from a single adult F1 hybrid mouse, derived from a cross between the C57BL/6J (henceforth B6) and CAST/EiJ (henceforth CAST) inbred strains. The B6 mother is *Mus musculus domesticus* and is genetically altered at the *Prdm9* gene to be homozygous for an allele carrying the zinc-finger domain found in many human populations (*26*), which we refer to as *Prdm9*$^{\mathrm{HUM}}$. The CAST father is *Mus musculus castaneus* and homozygous for the mouse wild-type *Prdm9* allele we call *Prdm9*$^{\mathrm{CAST}}$. The F1 mouse (hereafter, hybrid) is thus heterozygous at *Prdm9*, which allows us to compare the properties of hotspots associated with the two *Prdm9* alleles. Since *Prdm9*$^{\mathrm{HUM}}$ is not found in mice, we can separate biological properties of recombination from species-specific evolutionary effects. We also chose this design for the high sequence divergence between the parental strains (*27*), which improves localization of crossovers, and often allows us to assign events specifically to one or other of the two homologous chromosomes.

We sequenced the individual sperm from the hybrid mouse to a median depth of 6.3X, which yielded a median genome coverage of 62% (Fig. 1B). The genome coverage was stable, with 90% of sperm having coverage between 48% and 70% of the genome (Fig. S1). All sperm were euploid and there were no significant differences between the number of sperm carrying the X (108) or the Y (109) chromosome.

Each chromosome in the sperm is expected to comprise one or more segments of B6 and CAST genomes, with transitions between the haplotypes representing crossovers. We developed a Hidden-Markov model-based computational approach that maps sequencing reads to the B6 or the CAST haplotype (*25*, *27*), and identifies the most likely haplotypes taking sequencing error into account (Fig. 1C). We applied this approach to identify 2649 crossovers in our 217 sperm samples. The median resolution of crossovers is 916 bp, with 386 crossovers localized within 250 bp (Fig. S3). This large study of crossovers localized at a fine-scale in mammals provides a resource for understanding crossover formation genome-wide.

Molecular Assays

Recombination is a multi-stage process (*2*). We draw attention here to aspects of five of those stages. PRDM9 binds DNA in a sequence-specific manner (stage 1) and places an H3K4me3 mark on nearby nucleosomes (stage 2). SPO11 makes double-strand breaks (stage 3), which are resected to form single-stranded DNA (ssDNA) decorated with the meiosis-specific strand-exchange protein DMC1 and other proteins. The ssDNA covered with DMC1 undergoes a search for its homologous sequence (stage 4) and invades the homologous chromosome. This results in the formation of joint molecules, a subset of which are resolved as crossovers (stage 5).

To identify the factors affecting this process, we used data measuring H3K4me3 (stage 2) (*28*) and performed assays for DMC1 bound to ssDNA (stage 4) in testes. We focus on processes after the SPO11-induced DSB. In analyses below in the B6 mouse we can compare counts of DSBs, as measured directly using the SPO11-oligos produced with each DSB (*29*), with downstream properties. However, SPO11-oligo measures require impractically large numbers of mice and are not available in our hybrid. H3K4me3 levels and SPO11-oligos have high biological correlation ($r \approx 0.83$, Fig. S4, (*25*)). Therefore, where necessary in the hybrid mouse, we use measures of the H3K4me3 mark at hotspots as a surrogate for DSB counts.

Two distinct factors affect ChIP-seq measures for DMC1 on ssDNA: the number of breaks; and how long the ssDNA remains unpaired, which leads to the persistence of DMC1 near the break-site (*25*). Our peak calling algorithm (*26*) identified 24,586 peaks for DMC1. We also called peaks in H3K4me3 (*25*). In addition to hotspots, H3K4me3 is found at transcription start sites, and other functional elements, due to its role in the regulation of gene expression.

Properties of Crossovers

Amongst the 2649 genome-wide crossovers identified, 2615 crossovers are autosomal, corresponding to an autosomal map length of 12.1M, similar to previous work (*16*, *30*). We confirm robust crossover assurance on the autosomes (Fig. 2A). The number of crossovers per cell is compatible with random segregation of homologous chromosomes and sister chromatids, with no evidence of systematic variation in the number of crossovers between gametes (Figs. S5, S6).

Most crossovers overlapped hotspots identified by DMC1 ChIP-seq (92%) or H3K4me3 ChIP-seq (94%). Nearly all crossovers (96%) overlapped at least one of these two sets of hotspots, which is unlikely to happen by chance (*25*). The expected number and localization of crossovers to known hotspots provides evidence that our single-sperm sequencing approach is effective. Conversely, this also shows that nearly all crossovers happen in hotspots, with little recombination in the rest of the genome.

Hotspots with greater H3K4me3 have more crossovers ($p<10^{-15}$, test for Pearson's correlation), as expected. Total H3K4me3 in hotspots is also a good predictor of the number of crossovers per chromosome ((*25*), Fig. S7). However, crossovers are seen disproportionately more frequently in hotspots with higher H3K4me3 (Fig. 2B). The most active hotspots have a 5-fold number of crossovers compared to a larger set of less active hotspots with the same total level of H3K4me3 (Fig. S8).

Whilst crossovers overlapped 1634 distinct autosomal hotspots in total, several hotspots showed a high concentration of crossovers (Fig. S9). Each of 17 specific hotspots had crossovers in over 5% of meioses (95% CI=[2%-11%]). One sub-telomeric hotspot on chromosome 19 exhibited crossovers in more than 9% (95% CI=[4%-15%]) of meioses (Fig. 2C). These appear to be the most active hotspots for crossover identified in a mammal to date (*10*, *19*, *20*, *31*).

PRDM9 variants exhibit unexpected dominance and often bind asymmetrically to homologous sites in hotspots

Recombination hotspots in the hybrid mouse consist of hotspots that are activated by $\text{PRDM9}^{\text{CAST}}$ or $\text{PRDM9}^{\text{HUM}}$ and those that are PRDM9-independent (*32*). We can identify, in most cases, which PRDM9 variant activates a hotspot (*25*), and the DNA sequence motif to which it binds (Fig. S10) (*33*). Amongst autosomal crossovers that overlapped hotspots, 2309 (92%) overlapped a single DMC1 hotspot, of which 1377 (60%) overlapped $\text{PRDM9}^{\text{CAST}}$ and 784 (34%) overlapped $\text{PRDM9}^{\text{HUM}}$ hotspots. The remaining 148 crossovers (6%) could not be confidently assigned to an allele, including some (29, or 1.3%) where PRDM9-dependent and independent hotspots overlapped. We saw no instances of crossovers in the autosomes that could definitively be assigned to a PRDM9-independent hotspot. $\text{PRDM9}^{\text{CAST}}$ is dominant over $\text{PRDM9}^{\text{HUM}}$ for crossovers (64:36, 95% CI=62%-66%), as it is for H3K4me3 (62:38) and DMC1 (68:32) (also observed independently in (*28*)).

Hotspots in hybrid mice can vary in their activity on the two homologues if sequence differences cause differences in PRDM9 binding affinity at that position (*26*, *32*, *34*). Some such sequence differences are random polymorphisms. Others result from degradation of PRDM9-binding sites for evolutionary reasons: as a species evolves with a particular *Prdm9* allele, the best binding sites for that allele are lost from the host genome due to meiotic drive favoring hotspot-disrupting mutations (*35*). As a result, a particular PRDM9 variant will bind chromosomes from another genome in preference to its own. For example, $\text{PRDM9}^{\text{CAST}}$ binding sites are lost on CAST chromosomes, with no systematic loss on B6 chromosomes. In the hybrid, this leads to a spectrum of "asymmetry" in $\text{PRDM9}^{\text{CAST}}$ binding, with reduced binding on the CAST chromosome in many hotspots (Fig. S11). Informally, asymmetry is a measure of the extent to which PRDM9 preferentially binds one of the two homologues at a particular hotspot (Figs. 2D,E). As expected, $\text{PRDM9}^{\text{HUM}}$ shows asymmetry in a smaller fraction of hotspots, with no overall bias towards either chromosome (Fig. S11): evolutionary loss of binding sites has not occurred for the engineered $\textit{Prdm9}^{\text{HUM}}$ allele and the observed asymmetry is due to stochastic variation in DNA sequence, which affects both homologues equally on average.

The dominance of PRDM9^{CAST} over PRDM9^{HUM} despite loss of its binding sites is surprising. Both alleles appear to have similar overall levels of expression (Fig. S12), but different distributions of H3K4me3 across hotspots, with PRDM9^{CAST} hotspots skewed towards greater H3K4me3 (Fig. S13). This suggests a functional difference between the alleles, such as a greater affinity of the PRDM9^{CAST} zinc finger domain for its binding sites.

PRDM9 binding on the non-initiating, template, homologue boosts resolution as a crossover

Crossovers require engagement of the two homologous chromosomes, so it is natural to ask whether PRDM9 binding on both chromosomes influences crossover formation. To check this, we first compare the asymmetry of hotspots with their crossover resolution probability, informally the probability that a particular DSB resolves as crossover, which we estimate using H3K4me3 as the measure of recombination initiation (*25*). We find that asymmetry correlates with a decrease in crossover resolution probability (Fig. 3A), an effect also observed independently in a mouse pedigree (*28*). DSBs in very asymmetric hotspots are only 31% (95% CI=[19%–52%]) as likely to resolve as a crossover as those in symmetric hotspots ($p=5x10^{-6}$, (*25*)). We observe comparable effects for PRDM9^{HUM} and PRDM9^{CAST} hotspots (Fig. S14). The strong observed excess of DMC1 in asymmetric hotspots (Fig. S15) rules out the possibility that these hotspots simply have fewer DSBs.

A previous study (*32*) noted that hotspots that form crossovers in F1 mice tend to have a lower density of polymorphisms than other hotspots, and proposed that local DNA sequence heterozygosity caused reduced crossover formation. We find a slight effect of heterozygosity (p=0.06, (*25*)), but a significant effect with asymmetry ($p=2x10^{-13}$, (*25*)). Since asymmetry and the presence of polymorphisms are correlated ($p=1.6x10^{-280}$, test for Pearson's correlation), and polymorphisms within the PRDM9-binding motif are usually the cause of asymmetry (*26*), we checked whether the effect of heterozygosity could be due to its impact on asymmetry. This is the case: there is no effect of heterozygosity once asymmetry is taken into account (p=1, Fig. 3B, Table S1).

Asymmetric hotspots are less likely to have both homologues bound by PRDM9 (Figs. 2D,E). Therefore, a possible explanation may be that PRDM9 binding on the template chromosome (hereafter, template) increases the chance of a DSB being repaired as a crossover. To investigate further, we assessed how frequently crossovers arise on the "less-bound" and "more-bound" homologues in asymmetric hotspots. We selected asymmetric hotspots with the property that the more-bound homologue was 20-fold more likely to be bound by PRDM9 than the less-bound homologue on average. We identified 60 crossovers occurring at such asymmetric hotspots for which we could also infer the initiating chromosome (*25*), that is the chromosome on which the break occurred. If the likelihood of repairing a break as a crossover were equal between the homologues, we would simply expect to find that 20-fold more of these crossovers initiated on the more-bound than the less-bound homologue. Analysis of these 60 cases, however, revealed that significantly fewer than expected initiated on the more-bound homologue (47/60, $p=5x10^{-6}$, binomial test). The crossover resolution probability shows a clear directional effect (Fig. 3C): when a DSB does occur on the less-bound homologue it is 6 times more likely to form a crossover than a DSB which occurs on the more-bound homologue ($p<10^{-4}$, (*25*)). The more asymmetric the hotspot, the greater is the difference in crossover resolution between the homologues (Fig. S16). Differences in DNA sequence between the homologues cannot explain this directional effect within hotspots. We also rule out the possibility that the increase in crossovers on the less-bound homologue is driven by an increase in DSBs, as there is less DMC1 than expected on it (Fig. 3D). Our data strongly suggest a model in which it is PRDM9 binding on the template which promotes crossover formation: when a DSB occurs on the less-bound homologue, it is likely that PRDM9 will have bound the template (Fig. 3E). Conversely, when the more-bound homologue is cut, the template will not often be bound by PRDM9 (Fig. 3E). In fact, DSBs initiating on the less-bound homologue are almost 2.5 times more likely than those at symmetric hotspots to resolve as a crossover despite the greater heterozygosity at asymmetric hotspots (p=0.006, (*25*)).

If our model is correct, PRDM9-binding on the template should increase crossover resolution in all hotspots, regardless of whether they are asymmetric or not. Consistent with this, the rate of crossovers originating from a fixed amount of H3K4me3 on the initiating chromosome increases with H3K4me3 on the template chromosome (Fig. 3F). Hotspots with the greatest PRDM9 binding on the template are 4-fold more likely to have crossovers than hotspots with the lowest binding on the template. This effect also helps explain the observation above that more active hotspots have a disproportionately greater number of crossovers (*25*).

Taken together, these lines of evidence lead us to conclude that PRDM9 binding on the template chromosome increases the chance that a DSB is resolved as a crossover. Our data also imply that PRDM9 binding on the template is probably not essential for crossover formation (Fig. 3A).

PRDM9 allele, GC-content, and proximity to the distal telomere strongly influence crossover resolution

To identify further, independent, effects on crossover formation, we created two sets of otherwise-matched hotspots by pairing each hotspot that has a crossover with a hotspot that does not have a crossover (*25*). The paired hotspots were matched on their PRDM9-dependent H3K4me3 enrichment on both homologues and chosen to be on the same chromosome (1592 pairs). We then asked whether the hotspot sets differed in additional features.

While PRDM9^{CAST} is dominant over PRDM9^{HUM} overall, PRDM9^{HUM} hotspots have significantly more crossovers than PRDM9^{CAST} hotspots matched for the same level of H3K4me3 and asymmetry (Table S2, odds ratio=1.32, $p=2.7\times10^{-4}$, Fisher's exact test). The difference between the variants is greater for more active hotspots than for less active hotspots (Table S3).

We then matched hotspots for the allele, in addition to the criteria mentioned above, and find that hotspots with crossovers have significantly greater GC-content within 500 bp of the hotspot center (Fig. 4A, $p=1.2\times10^{-14}$, paired t-test). This is true of both PRDM9^{CAST} and PRDM9^{HUM} hotspots separately (Fig. S17), so cannot be explained by historical GC-biased gene conversion in PRDM9^{CAST} hotspots. The possible reasons for this observation are either an increase in DSBs, or a greater likelihood for a DSB to resolve as a crossover, in very local regions of higher GC. Previous data for SPO11-oligos in B6 (*29*) indicates that there is no significant effect of local GC-content on the number of breaks in hotspots (Fig. S18). Therefore, we conclude that greater GC-content is conducive to the repair of DSBs as crossovers.

Mouse chromosomes are acrocentric, and a well-known effect in male mice is a greater number of crossovers near distal telomeres (*16*), although the reason for this is not known. Crossover counts combine two different effects: the rate at which DSBs occur and the probability that a particular DSB resolves as a crossover. Analysis of SPO11-oligos in B6 establishes that the rate of DSBs within hotspots does not show spatial variation along a chromosome (Fig. S19), although the number of hotspots over broad scales may vary (*36*). On the other hand, our data show that the probability of DSB resolution as a crossover depends on the chromosomal location of a hotspot, increasing 5-fold from the centromere to the distal telomere (Figs. 4B, S20, S21). This chromosome-wide effect, which is strongest near the distal-telomere, cannot be explained solely by suppression of crossovers at the centromere (*11*, *12*).

The GC-and telomere effects are both observed with and without accounting for H3K4me3 (Figs. S22, S23). Additional analyses show that the four effects, namely, PRDM9 binding on the template, proximity to the distal telomere, PRDM9 allele and local GC-content, are distinct (Figs. S24-S26, (*25*)).

Factors that boost crossover probability also lead to faster homologue engagement

Each DSB results in a pair of long-lived SPO11 oligos, therefore quantitative sequencing of these oligos provides a direct measure of the number of DSBs (*29*). In contrast, the assay for DMC1 measures its *transient* association with the ssDNA near each DSB (*37*). As a result, it depends on both the number of DSBs and on how long DMC1 remains bound to the ssDNA. Therefore, comparison of DMC1 with SPO11-oligos allows an assessment of the time until DMC1 is no longer associated with ssDNA (*36*). Since this happens after successful strand invasion takes place and the homologues become locally engaged near the DSB site, we refer to the ratio of DMC1 to SPO11-oligos as a measure of "homologue-engagement time" (*25*).

The B6 mouse is the only one in which assays of H3K4me3, SPO11, and DMC1 are all currently available. From these data we find that, across hotspots, homologue-engagement time decreases as H3K4me3 levels increase, with DSBs at the most active hotspots engaging the fastest (Fig. 5A). Therefore, we can conclude that homologue-engagement time is affected by PRDM9-binding on the template chromosome (Fig. S27). Interestingly, even on the non-pseudoautosomal region of the X chromosome, where the sister chromatid is thought to be used as the template (*6*, *38*), repair is faster for hotspots with the highest levels of H3K4me3 (Fig. S28).

It is known that DMC1 relative to SPO11 is lower in the 5Mb adjacent to the centromere-distal telomere relative to the rest of the chromosome in B6 (*36*). Extending this finding, we show that the average DMC1 per hotspot increases further from the centromere-distal telomere (Fig. S29), although the rate of DSBs and the width of DMC1 loading near break-sites remain stable (Figs. S19, S30). Indeed, we find that homologue-engagement time increases continuously as a function of distance from the distal telomere (Fig. 5B), with engagement time for breaks furthest from the distal telomere 25% longer than for the nearest ones. Homologue-engagement time also decreases with increase in local GC-content in B6 (Fig. 5C).

Measurements of SPO11 are not available in our, or indeed in any, hybrid mouse, so to see whether the results from B6 extend to our hybrid, we approximate homologue-engagement time by using H3K4me3 in lieu of SPO11-oligos. Recapitulating the B6 findings, estimated homologue-engagement time in our hybrid mouse also decreases with increasing H3K4me3 on the template (Figs. S15, S31). In asymmetric hotspots, DSBs on the more-bound homologue take almost four times as long to repair as DSBs on the less-bound homologue (Fig. 5D). Similar results on the impact of PRDM9 on DMC1 have been seen in several F1 mice (*26*). As in B6, estimated homologue-engagement time in the hybrid increases with distance from the telomere ($p=10^{-31}$,(*25*)) and decreases with local GC-content ($p=2x10^{-15}$,(*25*)). Finally, for PRDM9^{HUM} hotspots, estimated homologue-engagement time is 18% lower on average relative to PRDM9^{CAST} hotspots (Fig. S32).

In summary, four factors influence homologue-engagement time and in each case they strongly and consistently influence crossover probability (*25*).

Crossover breakpoints are modulated by the chromatin environment on the template chromosome

Crossover breakpoints, which are the points at which sperm DNA switches from one parental chromosome to the other, have been shown to be contained within the extent of H3K4me3 modification (*39*) and of DMC1 binding (*29*) in a small number of hotspots. However, detailed knowledge of breakpoints has been elusive. Our data allow a genome-wide examination of the fine-scale distribution of crossover breakpoints.

For crossovers in symmetric PRDM9^{CAST} hotspots, we see a strongly multi-modal pattern of breakpoints (Fig. 6A). Breakpoints appear to flank positions occupied by nucleosomes around the PRDM9 binding site, with clear peaks in the first, second, and third nucleosome depleted regions (NDRs). In asymmetric hotspots, we also see a multi-modal pattern; however, it is shifted from that of symmetric hotspots (Fig. 6B). For hotspots that are not particularly symmetric or asymmetric, the peaks merge into a more continuous distribution (Fig. S33), as might be expected from a mix of both situations.

Nucleosome positions are known to exhibit a phase shift concomitant with PRDM9 binding (*39*). The homologue on which the DSB occurs is bound by PRDM9, regardless of whether the hotspot is symmetric or asymmetric (Figs. 6C,D). However, the template is much more likely to have been bound by PRDM9 in symmetric, compared to asymmetric, hotspots, and thus have a different nucleosome profile. The shift in crossover breakpoints that we observe between symmetric and asymmetric hotspots is consistent with the shift in nucleosomes between bound and unbound sites, and with a model in which crossover breakpoints avoid nucleosome positions (Figs. 6A,B, Fig. S34, (*25*)). We conclude that crossover resolution is modulated by nucleosome positioning on the template chromosome.

Crossover breakpoints also avoid nucleosomes in symmetric PRDM9^{HUM} hotspots (Fig. S35) although, in contrast with symmetric PRDM9^{CAST} hotspots, there does not seem to be a peak in the first NDR from the motif site (Figs. 6A, S36). This may be due to PRDM9^{CAST} binding the template more strongly or for longer than PRDM9^{HUM}, thereby, for example, creating a greater barrier to Holliday junction migration. Alternatively, this may point to differences in the *a priori* histone binding energies in regions that each allele prefers to bind, making nucleosomes more or less difficult to evict. Indeed, while PRDM9^{CAST} preferentially binds sites that are occupied by a nucleosome *a priori*, PRDM9^{HUM} preferentially binds sites that are depleted in nucleosomes (Fig. S37). The overall differences in crossover breakpoints between the two alleles (Fig. S38) reflect both differences at symmetric hotspots, and the different proportions of symmetric and asymmetric hotspots for each allele.

Crossovers in the Pseudoautosomal Region

The pseudoautosomal region (PAR) is a short region of homology between the X and Y chromosomes, which must have a crossover in males for successful segregation of these chromosomes during meiosis. The precise PAR region varies in mouse subspecies – it is ~700 kb long in B6 and 430 kb longer in CAST (*40*) (Fig. S39). A crossover in the PAR is achieved partly by an increased DSB rate, which is thought to be the result of a disproportionally long axis in this region (*41*). However, it is not known whether these biological properties of the PAR are determined by *cis*- or *trans*-acting factors. Specifically, it is not clear if the PARs on both chromosomes in the hybrid behave differently, retaining the properties of their parental strains, or if one of the parental strains is dominant.

We compare the DMC1 signal in hotspots in the region that is pseudoautosomal in CAST but not B6 (henceforth het-PAR, Fig. S39). Most of these hotspots have an excess of DMC1 on the CAST relative to the B6 chromosome, with 7-fold greater DMC1 on the CAST chromosome on average (Fig. 7A, $p<10^{-4}$,(*25*)). This is not explained by any artefactual differences in sequence mapping between the haplotypes (Fig. 7A, p=0.85,(*25*)). The effect could be explained by a greater number of DSBs on the CAST chromosome or by DSBs initiating on the CAST chromosome taking longer to engage their homologue, or both. Either way, it follows that the CAST and B6 regions behave differently, which implies that the PAR is determined by factors that can distinguish between them, likely cis-acting factors.

We identified 34 PAR crossovers in 217 sperm, all of which are in the het-PAR (Fig. S40). These crossovers demonstrate that any potential structural differences between the two homologues in this region do not preclude reciprocal exchange between them. The number of crossovers we identified is roughly in line with the proportional size of the het-PAR within the whole PAR (34 out of 108.5, which is expected if there is one crossover per meiosis). We do not have power to detect crossovers outside the het-PAR due to lack of adequate sequence assembly.

While previous research has shown the co-existence of PRDM9-dependent and independent hotspots near the PAR (*42*), their relative importance in crossover formation within the PAR remains unclear (*42*, *43*). We found that 19 crossovers overlapped PRDM9-independent hotspots, 4 overlapped $\text{PRDM9}^{\text{CAST}}$, and none overlapped $\text{PRDM9}^{\text{HUM}}$ hotspots. PRDM9-independent hotspots have 53% of the DMC1 signal among het-PAR hotspots, yet the concentration of crossovers in them is substantially greater (83%, p=0.016, (*25*)). This suggests differences in the timing or processing of DSBs in PRDM9-independent hotspots. The dominance of PRDM9-independent hotspots over $\text{PRDM9}^{\text{HUM}}$ hotspots also proves that it is not simply a consequence of the evolutionary erosion of PRDM9 binding motifs in this region. Genome-wide the hotspot with the greatest number of crossovers is in the het-PAR, and PRDM9-independent, with crossovers in 11% of meioses (Fig. 7B). While the mechanism controlling PRDM9-independent hotspots is not currently known, we note that the number of DSBs in these hotspots is disproportionately elevated genome-wide in *Atm*$^{-/-}$ mice (Fig. S41). This shows a role, either direct or indirect, for the ATM pathway in modulating the use of PRDM9-independent hotspots.

Discussion

Recombination via the formation of crossovers is a central part of meiosis. We have identified four distinct factors that affect the probability that a particular DSB is resolved as a crossover: (1) whether PRDM9 is or has bound at the same position on the homologous chromosome; (2) distance from the centromere-distal telomere; (3) local GC-content around the DSB; and (4) whether $\text{PRDM9}^{\text{HUM}}$ or $\text{PRDM9}^{\text{CAST}}$ bound the hotspot where the DSB occurred. Our work uniquely separates upstream effects (numbers of DSBs) from those downstream of the breaks, and implicates each of these four factors in an increase in the preferential use of the crossover pathway for DSB repair. The effect of these factors appears to be cumulative, so that hotspots with multiple favourable conditions are most likely to form crossovers (Fig. S42). Equally, the effect of an unfavorable condition in one factor may be mitigated by a favorable condition in another: for example, while breaks in asymmetric hotspots are less likely to resolve as crossovers overall, those in telomere-proximal asymmetric hotspots are more likely to do so than breaks in telomere-distal symmetric hotspots (Fig. S42).

We further show that the same four factors that increase the probability that a particular DSB is resolved as a crossover also decrease homologue-engagement time, namely the time until successful strand invasion takes place and DMC1 is no longer associated with ssDNA. The relative impact of these factors is also consistent for both, with the biggest effect being PRDM9 binding on the homologue, followed by telomere proximity, GC-content, and PRDM9 variant (*25*). Note that multiple lines of evidence establish that it is PRDM9 binding on the homologue, rather than polymorphisms or hotspot asymmetry *per se*, which affects outcomes for DSBs. The relative effect sizes are consistent with the presence of additional factors impacting the spatial localization of crossovers within a chromosome (*25*).

Each meiotic cell has to solve, for each DSB, the seemingly intractable problem of finding the homologous sequence amongst billions of bases of DNA (*4*). The factors we have identified, by virtue of their impact on homologue-engagement time, suggest potential mechanisms that affect this process. A natural explanation for the effect of PRDM9 binding on the homologue is that it facilitates homology search, either directly or indirectly. Possible mechanisms for this include its effect on the local chromatin environment (*44*), a role in bringing the template homologue to the chromosome axis (*45*) (thereby reducing the search space) or direct interaction between PRDM9 molecules at the DSB site and the template. Telomeres have distinct properties in meiosis which may facilitate homology search: they are physically bound to the nuclear envelope (*46*), and may thus be closer to each other *a priori* (*47*). They also engage in active movements during the phase of meiosis when the search for the homologue is taking place (*48*). The effect of GC-content could be mediated by its influence on the local chromatin environment (*49*).

Why are rapidly engaging breaks more likely to become crossovers? A compelling explanation is that delay in finding and engaging the homologue itself is a causal factor. There are several classes of mechanism, which are not mutually exclusive, with this property. In the first class, the earlier a DSB engages its homologue the more likely it is to be resolved as a crossover. For example, sites of early-engaging breaks may be more likely to appropriate and stabilize protein complexes that are essential for crossover formation (*50*). This view is consistent with cytological findings that crossover sites are correlated with those where formation of the synaptonemal complex nucleates (*18*, *51*, *52*). A second class of model posits a window of opportunity during which DSB sites can acquire the necessary protein complexes and become crossover-proficient (crossover licensing (*53*)): early-engaging breaks may resolve as crossovers more often by virtue of having found their homologue prior to the end of this period. If multiple breaks on a particular chromosome engage their homologue during this window, other factors may determine which will become crossovers (*18*). One possibility is that several (or all) breaks might initially proceed down the crossover repair pathway (*53*, *54*) but in the event of a surfeit in prospective crossovers, a subset of them could be re-designated down an alternative repair pathway (crossover designation (*53*, *55*)). A third class of model is that highly-delayed breaks, which may have failed to engage the homologue, are repaired from the sister, for example via a cut-off mechanism after which the cell switches from homologue-mediated to sister-mediated repair of the remaining breaks (*6*, *38*).

Previous research has shown the impact of nucleosomes on the initiating chromosome on strand-resection (*56*). We have shown that the distribution of crossover breakpoints differs depending on whether PRDM9 has bound the template and is affected by the template's chromatin environment. This suggests that PRDM9 often remains bound (and actively maintaining the local nucleosome environment) on the template until at least strand invasion and perhaps until Holliday junction resolution. Finally, our work sheds new light on how crossover is achieved in the PAR.

Methods Summary:

We harvested and isolated 217 sperm from an adult B6xCAST mouse, which has the *Prdm9* alleles *Prdm9*$^{\mathrm{HUM}}$ (*26*) and *Prdm9*$^{\mathrm{CAST}}$ (*32*). We developed a protocol for whole-genome amplification and DNA sequencing of single cells (*25*), which we applied to the sperm. Bulk sperm from the same animal was sequenced at high-depth and the DNA sequence was used to call variants *de novo.* We developed a computational approach to identify the most likely sequence of CAST and B6 haplotypes in each chromosome in each sperm (*25*). DMC1 ChIP-seq (*37*) was performed using testis tissue from the same animal, and hotspots were called using our previously published peak-calling algorithm (*26*). The PRDM9 variants activating hotspots (*25*) and the PRDM9-binding DNA sequence motifs in them (*33*) were identified. We developed a method for assessing the evidence of enrichment in H3K4me3 from ChIP-seq data (*25*). MNase-seq and H3K4me3 Mnase ChIP-seq were performed in testes from another animal with the same genetic background (*25*).

References and Notes:

1. F. Cole *et al.*, Homeostatic control of recombination is implemented progressively in mouse meiosis. *Nat. Cell Biol.* **14**, 424–430 (2012).
2. F. Baudat, Y. Imai, B. de Massy, Meiotic recombination in mammals: localization and regulation. *Nat Rev Genet*. **14**, 794–806 (2013).
3. Z. Baker *et al.*, Repeated losses of PRDM9-directed recombination despite the conservation of PRDM9 across vertebrates. *Elife*. **6**, e24133 (2017).
4. J. Renkawitz, C. A. Lademann, S. Jentsch, Mechanisms and principles of homology search during recombination. *Nat. Rev. Mol. Cell Biol.* **15**, 369–383 (2014).
5. F. Cole, S. Keeney, M. Jasin, Preaching about the converted: how meiotic gene conversion influences genomic diversity. *Ann. N. Y. Acad. Sci.* **1267**, 95–102 (2012).
6. J. P. Lao, N. Hunter, Trying to avoid your sister. *PLoS Biol*. **8**, e1000519 (2010).
7. B. L. Dumont, Variation and Evolution of the Meiotic Requirement for Crossing Over in Mammals. *Genetics*. **205**, 155–168 (2017).
8. E. Martinez-Perez, M. P. Colaiácovo, Distribution of meiotic recombination events: talking

to your neighbors. *Curr. Opin. Genet. Dev.* **19**, 105–112 (2009).

9. S. Sarbajna *et al.*, A major recombination hotspot in the XqYq pseudoautosomal region gives new insight into processing of human gene conversion events. *Hum Mol Genet* (2012), doi:10.1093/hmg/dds019.

10. E. de Boer, M. Jasin, S. Keeney, Local and sex-specific biases in crossover vs. noncrossover outcomes at meiotic recombination hot spots in mice. *Genes Dev.* **29**, 1721–1733 (2015).

11. M. E. Serrentino, E. Chaplais, V. Sommermeyer, V. Borde, Differential association of the conserved SUMO ligase Zip3 with meiotic double-strand break sites reveals regional variations in the outcome of meiotic recombination. *PLoS Genet*. **9**, e1003416 (2013).

12. N. Vincenten *et al.*, The kinetochore prevents centromere-proximal crossover recombination during meiosis. *Elife*. **4**, 923 (2015).

13. K. R. Fowler, M. Sasaki, N. Milman, S. Keeney, G. R. Smith, Evolutionarily diverse determinants of meiotic DNA break and recombination landscapes across the genome. *Genome Res*. **24**, 1650–1664 (2014).

14. A. Capalbo, E. R. Hoffmann, D. Cimadomo, F. M. Ubaldi, L. Rienzi, Human female meiosis revised: new insights into the mechanisms of chromosome segregation and aneuploidies from advanced genomics and time-lapse imaging. *Hum. Reprod. Update*. **23**, 706–722 (2017).

15. C. Bhérer, C. L. Campbell, A. Auton, Refined genetic maps reveal sexual dimorphism in human meiotic recombination at multiple scales. *Nat Commun*. **8**, 14994 (2017).

16. E. Y. Liu *et al.*, High-resolution sex-specific linkage maps of the mouse reveal polarized distribution of crossovers in male germline. *Genetics*. **197**, 91–106 (2014).

17. A. Kong *et al.*, Fine-scale recombination rate differences between sexes, populations and individuals. *Nature*. **467**, 1099–1103 (2010).

18. N. Hunter, Meiotic Recombination: The Essence of Heredity. *Cold Spring Harb Perspect Biol*. **7**, a016618 (2015).

19. F. Cole, S. Keeney, M. Jasin, Comprehensive, fine-scale dissection of homologous recombination outcomes at a hot spot in mouse meiosis. *Mol Cell*. **39**, 700–710 (2010).

20. A. J. Webb, I. L. Berg, A. Jeffreys, Sperm cross-over activity in regions of the human genome showing extreme breakdown of marker association. *Proceedings of the National Academy of Sciences*. **105**, 10471–10476 (2008).

21. S. Lu *et al.*, Probing meiotic recombination and aneuploidy of single sperm cells by whole-genome sequencing. *Science*. **338**, 1627–1630 (2012).

22. J. Wang, H. C. Fan, B. Behr, S. R. Quake, Genome-wide Single-Cell Analysis of Recombination Activity and De Novo Mutation Rates in Human Sperm. *Cell*. **150**, 402–412

(2012).

23. I. L. Berg *et al.*, *PRDM9* variation strongly influences recombination hot-spot activity and meiotic instability in humans. *Nat Genet*. **42**, 859–863 (2010).

24. A. G. Hinch *et al.*, The landscape of recombination in African Americans. *Nature*. **476**, 170–175 (2011).

25. More information on materials, methods, and analyses are available as supplementary materials.

26. B. Davies *et al.*, Re-engineering the zinc fingers of PRDM9 reverses hybrid sterility in mice. *Nature*. **530**, 171–176 (2016).

27. T. M. Keane *et al.*, Mouse genomic variation and its effect on phenotypes and gene regulation. *Nature*. **477**, 289–294 (2011).

28. R. Li *et al.*, A high-resolution map of non-crossover events reveals impacts of genetic diversity on mammalian meiotic recombination. *biorxiv.org*, doi:10.1101/428987.

29. J. Lange *et al.*, The Landscape of Mouse Meiotic Double-Strand Break Formation, Processing, and Repair. *Cell*. **167**, 695–708.e16 (2016).

30. L. Froenicke, L. K. Anderson, J. Wienberg, T. Ashley, Male mouse recombination maps for each autosome identified by chromosome painting. *Am J Hum Genet*. **71**, 1353–1368 (2002).

31. F. Cole *et al.*, Mouse tetrad analysis provides insights into recombination mechanisms and hotspot evolutionary dynamics. *Nat Genet*. **46**, 1072–1080 (2014).

32. F. Smagulova, K. Brick, Y. Pu, R. D. Camerini-Otero, G. V. Petukhova, The evolutionary turnover of recombination hot spots contributes to speciation in mice. *Genes Dev.* **30**, 266–280 (2016).

33. N. Altemose *et al.*, A map of human PRDM9 binding provides evidence for novel behaviors of PRDM9 and other zinc-finger proteins in meiosis. *Elife*. **6**, e28383 (2017).

34. C. L. Baker *et al.*, PRDM9 drives evolutionary erosion of hotspots in Mus musculus through haplotype-specific initiation of meiotic recombination. *PLoS Genet*. **11**, e1004916 (2015).

35. G. Coop, S. R. Myers, Live hot, die young: transmission distortion in recombination hotspots. *PLoS Genet*. **3**, e35 (2007).

36. S. Yamada *et al.*, Genomic and chromatin features shaping meiotic double-strand break formation and repair in mice. *Cell Cycle*. **16**, 1870–1884 (2017).

37. P. P. Khil, F. Smagulova, K. M. Brick, R. D. Camerini-Otero, G. V. Petukhova, Sensitive mapping of recombination hotspots using sequencing-based detection of ssDNA. *Genome Res*. **22**, 957–965 (2012).

38. L.-Y. Lu, X. Yu, Double-strand break repair on sex chromosomes: challenges during male meiotic prophase. *Cell Cycle*. **14**, 516–525 (2015).

39. C. L. Baker, M. Walker, S. Kajita, P. M. Petkov, K. Paigen, PRDM9 binding organizes hotspot nucleosomes and limits Holliday junction migration. *Genome Res*. **24**, 724–732 (2014).

40. M. A. White, A. Ikeda, B. A. Payseur, A pronounced evolutionary shift of the pseudoautosomal region boundary in house mice. *Mammalian Genome*. **23**, 454–466 (2012).

41. L. Kauppi *et al.*, Distinct properties of the XY pseudoautosomal region crucial for male meiosis. *Science*. **331**, 916–920 (2011).

42. K. Brick, F. Smagulova, P. Khil, R. D. Camerini-Otero, G. V. Petukhova, Genetic recombination is directed away from functional genomic elements in mice. *Nature*. **485**, 642–645 (2012).

43. A. G. Hinch, N. Altemose, N. Noor, P. Donnelly, S. R. Myers, Recombination in the human Pseudoautosomal region PAR1. *PLoS Genet*. **10**, e1004503 (2014).

44. W. Kobayashi *et al.*, Chromatin architecture may dictate the target site for DMC1, but not for RAD51, during homologous pairing. *Scientific Reports*. **6**, 24228 (2016).

45. Y. Imai *et al.*, The PRDM9 KRAB domain is required for meiosis and involved in protein interactions. *Chromosoma*. **126**, 681–695 (2017).

46. H. Scherthan, Telomere attachment and clustering during meiosis. *Cell. Mol. Life Sci.* **64**, 117–124 (2007).

47. C.-S. Lee *et al.*, Chromosome position determines the success of double-strand break repair. *Proceedings of the National Academy of Sciences*. **113**, E146–54 (2016).

48. C.-Y. Lee *et al.*, Mechanism and regulation of rapid telomere prophase movements in mouse meiotic chromosomes. *Cell Rep*. **11**, 551–563 (2015).

49. J. Wang *et al.*, Sequence features and chromatin structure around the genomic regions bound by 119 human transcription factors. *Genome Res*. **22**, 1798–1812 (2012).

50. A. Reynolds, H. Qiao, Y. Yang, J. K. Chen, N. Jackson, RNF212 is a dosage-sensitive regulator of crossing-over during mammalian meiosis. *Nat Genet* (2013).

51. J. R. Gruhn *et al.*, Correlations between Synaptic Initiation and Meiotic Recombination: A Study of Humans and Mice. *Am J Hum Genet*. **98**, 102–115 (2016).

52. G. V. Börner, N. Kleckner, N. Hunter, Crossover/noncrossover differentiation, synaptonemal complex formation, and regulatory surveillance at the leptotene/zygotene transition of meiosis. *Cell*. **117**, 29–45 (2004).

53. R. Yokoo *et al.*, COSA-1 reveals robust homeostasis and separable licensing and

reinforcement steps governing meiotic crossovers. *Cell*. **149**, 75–87 (2012).

54. F. Baudat, B. de Massy, Regulating double-stranded DNA break repair towards crossover or non-crossover during mammalian meiosis. *Chromosome Res*. **15**, 565–577 (2007).

55. A. Woglar, A. M. Villeneuve, Dynamic Architecture of DNA Repair Complexes and the Synaptonemal Complex at Sites of Meiotic Recombination. *Cell*. **173**, 1678–1691.e16 (2018).

56. E. P. Mimitou, S. Yamada, S. Keeney, A global view of meiotic double-strand break end resection. *Science*. **355**, 40–45 (2017).

57. L. Zhang *et al.*, Whole genome amplification from a single cell: implications for genetic analysis. *Proc Natl Acad Sci USA*. **89**, 5847–5851 (1992).

58. A. Rimmer *et al.*, Integrating mapping-, assembly- and haplotype-based approaches for calling variants in clinical sequencing applications. *Nat Genet*. **46**, 912–918 (2014).

59. T. Billings *et al.*, DNA binding specificities of the long zinc finger recombination protein PRDM9. *Genome Biol.* **14**, R35 (2013).

60. Gunnar Blom. Transformations of the binomial, negative binomial, Poisson AND χ2 distributions. *Biometrika.* **41**, 302–316 (1954).

61. J. Lange *et al.*, ATM controls meiotic double-strand-break formation. *Nature*. **479**, 237–240 (2011).

62. M. S. Brown, D. K. Bishop, DNA Strand Exchange and RecA Homologs in Meiosis. *Cold Spring Harb Perspect Biol*. **7**, a016659 (2014).

63. V. Cloud, Y.-L. Chan, J. Grubb, B. Budke, D. K. Bishop, Rad51 Is an Accessory Factor for Dmc1-Mediated Joint Molecule Formation During Meiosis. *Science*. **337**, 1222–1225 (2012).

64. O. Da Ines, K. Abe, C. Goubely, M. E. Gallego, C. I. White, Differing Requirements for RAD51 and DMC1 in Meiotic Pairing of Centromeres and Chromosome Arms in Arabidopsis thaliana. *PLoS Genet*. **8**, e1002636 (2012).

65. G. Singh, O. Da Ines, M. E. Gallego, C. I. White, Analysis of the impact of the absence of RAD51 strand exchange activity in Arabidopsis meiosis. *PLoS ONE*. **12**, e0183006 (2017).

66. F. Smagulova *et al.*, Genome-wide analysis reveals novel molecular features of mouse recombination hotspots. *Nature*. **472**, 375–378 (2011).

67. K. J. Livak, T. D. Schmittgen, Analysis of relative gene expression data using real-time quantitative PCR and the 2(-Delta Delta C(T)) Method. *Methods*. **25**, 402–408 (2001).

Acknowledgments: We thank R. Li and C. Green for helpful discussions, and the High-Throughput Genomics team at the Wellcome Centre for Human Genetics for all sequencing work. We are grateful to

E. Hatton for analytical work in the early development of our single sperm sequencing protocol. **Funding:** Wellcome Trust grants 095552/Z/11/Z to PD and grants 090532/Z/09/Z and 20314/Z/16/Z as core support for the Wellcome Centre for Human Genetics. RH is supported by Wellcome Trust grant 106130/Z/14/Z. **Author Contributions:** P.D. designed the study. B.D. bred the mice. G.Z. developed the single-cell sequencing protocol with assistance from R.B. and performed the single-cell sequencing experiments. P.W.B. performed MNase ChIP-seq. D.M. performed cytological analysis. A.G.H. analyzed the data. R.H. contributed to the H3K4me3 peak caller. A.G.H. and P.D. wrote the paper with input from G.Z., P.W.B, R.H., and B.D. **Competing interests:** PD is founder and CEO of Genomics plc, and a partner in Peptide Groove LLP. G.Z., R.B. and P.D. are listed as co-inventors on a patent application for the single-cell DNA amplification and sequencing protocol. P.W.B is now an employee of GeneFirst Ltd.

Data and materials availability: Raw and processed data are available on the Gene Expression Omnibus website under SuperSeries accession GSE125327, comprising GSE125326 (sperm sequencing) and GSE124991 (DMC1). Code is available on Zenodo (DOI 10.5281/zenodo.2540356).

Supplementary Materials:

Materials and Methods

Supplementary Text

Figures S1-S43

Tables S1-S3

References *(57-67)*

Main manuscript figures (Figures 1-7)

Figure 1: Experimental design for inferring crossovers from single sperm cells.

A. An illustration of the method for whole-genome amplification (WGA) of isolated single sperm cells (*25*). Random RNA oligonucleotides act as primers for WGA mediated by Klenow fragment, which displaces adjacent synthesized fragments to form overlapping single-stranded DNA copies. These, in turn, serve as templates for primer annealing and chain extension. The resulting amplicons are converted into double-stranded DNA for sequencing.

B: Sequencing depth and genome coverage achieved for each of 217 sperm.

C: An Integrative Genomics Viewer (IGV) illustration of how a crossover was called by our method. The horizontal light gray lines show the reads that mapped in a region of chromosome 13 for a particular sperm. Vertical dark gray bars highlight variants found only in B6, while orange bars highlight variants found only in CAST. The crossover breakpoint lies within a region of uncertainty (green). This crossover overlapped a PRDM9^{HUM} hotspot, identified by DMC1 ChIP-seq (*25*), whose center was inferred to be at 113,864,493. A good match to the PRDM9^{HUM} binding motif occurs in the purple region.

Figure 2. Properties of crossovers and recombination hotspots.

A: Average number of crossovers called per chromosome per sperm (bars show 1 standard error), showing at least, and in many cases almost exactly, one crossover per chromosome per meiosis (equivalently 0.5 crossovers per haploid sperm).

B: Distribution of H3K4me3 intensity in all autosomal recombination hotspots identified by DMC1 ChIP-seq (blue), after removing hotspots showing evidence of PRDM9-independent H3K4me3 (e.g. transcription-start sites, (*25*)). If crossovers occurred in proportion to the hotspot heat, the distribution of H3K4me3 in hotspots with crossovers should be the corresponding size-biased distribution (green). The observed distribution of H3K4me3 in hotspots with crossovers (red) is skewed further towards hotspots with greater H3K4me3 ($p = 10^{-90}$).

C: The most active autosomal hotspot for crossover is on the centromere-distal end of chromosome 19. DMC1 binds the 3' ssDNA overhangs on either side of the DSB, which leads to a shift between DMC1 coverage on the forward (blue) and reverse (red) strands (200 bp smoothing). Regions containing the crossover breakpoint in each sperm are in black. Crossovers at the same locus in distinct sperm can have different resolution, depending on the actual sequencing coverage achieved in each case.

D: PRDM9 binding at a hotspot is a stochastic event in a cell. In a population of cells, some proportion of cells will have one, both, or neither homologue bound by PRDM9 (sky blue). Here we show the proportion of times each of these possibilities occurs at two illustrative symmetric hotspots. In the very active hotspot (top row), PRDM9 binds the B6 (red) and CAST (blue) homologues with probability 80% each. As a result, PRDM9 is bound to *both* homologues in the majority of cells (64%). In the less active hotspot, the probability of PRDM9 binding each homologue is 40%. The proportion of cells in which PRDM9 is bound to both homologues is lower (16%).

E. As in D, a comparison of the proportion of cells in which PRDM9 (sky blue) binds one or both homologues, B6 (red) and CAST (dark blue) but at an illustrative asymmetric hotspot. The probability of PRDM9 binding the B6 homologue is ~80% but only ~4% for the CAST homologue. This is due to a SNP (yellow) in the PRDM9 motif on the CAST homologue, which partially disrupts binding. Only a small minority of cells have PRDM9 bound to both homologues.

Figure 3. PRDM9 binding on the non-initiating, template homologue affects crossover resolution.

A: Hotspots were binned into five groups depending on the level of asymmetry in PRDM9 binding of the homologues (*25*). The crossover resolution probability, which accounts for differences in H3K4me3, in each bin (normalized relative to the bin with the most symmetric hotspots, y-axis, 1 standard error bars), is plotted against the mean asymmetry of hotspots in that bin (x-axis). Predicted effects on crossover resolution if PRDM9 binding on the template homologue was irrelevant (black) and if it was essential (red) are shown for comparison.

B: Hotspots were grouped into four bins depending on the number of SNP differences between B6 and CAST chromosomes in the central 200 bases of the hotspot. The crossover resolution probability in each bin (blue) was inferred relative to the bin containing hotspots with zero SNPs. Red points show the same quantity after correcting for asymmetry in PRDM9 binding. Bars show 1 standard error.

C: Crossover resolution probability is significantly higher for DSBs initiated on the “less-bound” homologue than the “more-bound” homologue in asymmetric hotspots. Crossover resolution probabilities for initiation on the more-bound (red, n=47) and less-bound homologues (blue, n=13), after accounting for differences in H3K4me3 on them. Probabilities were normalized against the average for symmetric hotspots (dashed black line), bars show 95% confidence intervals (*25*).

D: Fraction of crossovers (green), H3K4me3 (blue) and DMC1 (red) originating on the less-bound chromosome in asymmetric hotspots, with dashed line marking the proportion expected from H3K4me3. While the fraction of crossovers initiating on the less-bound chromosome is significantly greater than expected from H3K4me3 ($p=5x10^{-6}$), the fraction of DMC1 is significantly lower than expected from H3K4me3 ($p<10^{-16}$). Bars show 1 standard error.

E: Illustration that the probability of PRDM9 having bound the *template* depends on which homologue is initially cut for the same asymmetric hotspot as in Fig. 2E. A DSB is more likely to occur on the more-bound homologue B6 (red). When it does, fewer than 4% of cells (3/80) will have the template CAST homologue (blue) bound. In the less likely event that the CAST homologue is cut, the B6 homologue will have been bound in 75% of cells (3/4). (Note that cells with PRDM9 bound on both homologues are twice as likely to be cut at this hotspot than cells with only one homologue bound.)

F: Crossover resolution is influenced by PRDM9 binding on the template homologue. All potential sites for recombination initiation, i.e., the B6 and CAST homologous sites in each hotspot, were sorted according to the H3K4me3 on their respective template homologues. The initiating sites were then binned into 7 bins, such that the total H3K4me3 intensity on the initiating sites in each bin is the same. The proportion of crossovers that initiated in each bin (out of 685 crossovers where the initiating homologue could be inferred) is shown against the average H3K4me3 on the corresponding template homologues (x-axis). Dotted red line shows the expected relationship if H3K4me3 on the template were unrelated to crossover outcome.

Figure 4. Crossover resolution is affected by local GC-content and Telomere proximity.

A: Each autosomal hotspot with a crossover was paired with another hotspot lacking a crossover for the same PRDM9 variant, on the same chromosome and with very similar H3K4me3 on both homologues (*25*). The distribution of local GC-content (500 bp around the hotspot center) is compared between the two matched sets ($n=1355$, $p=1.2\times10^{-14}$, paired t-test).

B: Hotspots were divided into 7 bins depending on their distance from the distal telomere of their respective chromosome. Crossover resolution probability (relative to the leftmost bin) is shown for each bin (1 standard error bars). Chromosomes with more than one crossover in an individual sperm were removed to avoid confounding with crossover interference (see Figs. S20-S21 for additional views).

Figure 5. Factors affecting homologue-engagement time in the repair of DSBs.

A: Hotspots in the B6 mouse were ordered by their H3K4me3 intensity and divided into 10 bins. Average homologue-engagement time, the ratio of total DMC1 with total SPO11 per bin (y-axis), is shown relative to the average H3K4me3 per hotspot in each bin (x-axis).

B: Hotspots in the B6 mouse were divided into 8 bins depending on their distance from the distal telomere of their respective chromosome. Average homologue-engagement time (ratio of total DMC1 with total SPO11 in each bin) is shown (1 standard error bars).

C: Hotspots in the B6 mouse were divided into 6 bins depending on their local GC-content (± 500 bp around the hotspot center). Average homologue-engagement time per bin is shown (bars show 95% confidence intervals).

D: Comparison of estimated homologue-engagement time for the more-bound homologue (red) and less-bound homologue (blue) in asymmetric hotspots (corresponding to Fig. 3C, 95% confidence intervals, (*25*)). Estimated homologue-engagement time (ratio of DMC1 with H3K4me3) is normalized against the average for symmetric hotspots (dashed black line).

Figure 6. Positioning of crossover breakpoints is influenced by nucleosome positioning on the template chromosome.

A: Distribution of crossover breakpoints from the motif center (green) for crossovers that overlap symmetric PRDM9^{CAST} hotspots with a well-identified motif site, and have breakpoint resolution ≤250bp (n=132). To deal with the uncertainty in crossover breakpoint location in each sperm we assign equal weight to all possible breakpoint positions in that sperm (*25*). H3K4me3 ChIP-seq with MNase averaged over PRDM9^{CAST} hotspots in red (20bp smoothing). Red bars at top show average inferred positions of nucleosomes, black bar shows the PRDM9^{CAST} binding site.

B: As (A) but for crossovers that overlap asymmetric PRDM9^{CAST} hotspots (n=33). Average MNase-seq for the less-bound chromosome of asymmetric hotspots (blue, 50bp smoothing), with blue bars at top showing average inferred nucleosome positions. This is an estimate of the nucleosome positioning at hotspot sites when PRDM9 is not bound (*25*). The peak in MNase-seq at the hotspot center is consistent with the presence of a nucleosome in PRDM9^{CAST} hotspots in the absence of PRDM9 binding (Fig. S37).

C: Illustration of nucleosome positions when the template homologue is bound by PRDM9^{CAST}. DNA (dark brown) around histones (light brown), with red dots indicating H3K4me3 mark. Nucleosome positions on the DSB-initiating and template homologues are the same. This is more likely in symmetric hotspots (A).

D: Illustration of nucleosome positions when the template homologue is not bound by PRDM9^{CAST}. Colours as in (C). Typical nucleosome positioning at sites bound by PRDM9 is shifted relative to unbound sites, resulting in a difference between the DSB-initiating and template chromosomes. This is more likely in asymmetric hotspots (B). The shift in crossover breakpoints between (A) and (B) is consistent with the shift in nucleosome positions on the template homologue, as illustrated in (C) and (D).

Figure 7. Differences in recombination in the pseudoautosomal region.

A: Histogram of the fraction of DMC1 reads on the CAST chromosome across hotspots (red, n=38). For the same regions, the corresponding histogram for reads from sequencing of bulk sperm is shown (blue) as a control to assess potential mapping artefacts. While DMC1 is significantly biased towards the CAST haplotype ($p<10^{-4}$, (*25*)), there is no significant bias in bulk sequencing (median=0.51, p=0.85, (*25*)).

B: The most active hotspot for crossovers in the entire genome is in the het-PAR and is PRDM9-independent. DMC1 coverage (200bp smoothing) is shown for the forward (blue) and reverse (red) strands. Crossover breakpoints are in black. See Fig. S43 for a further het-PAR hotspot.

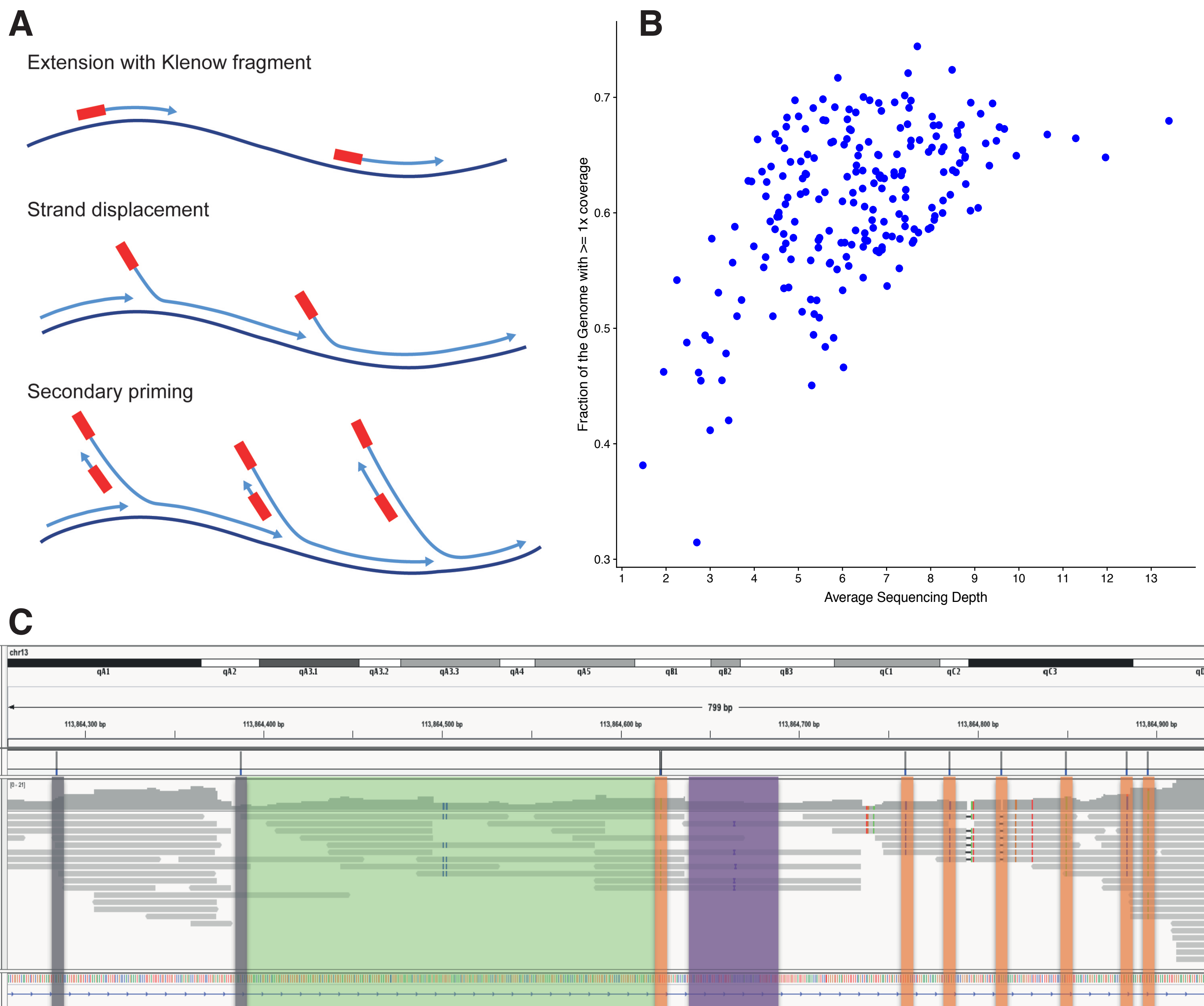
A
Extension with Klenow fragment
Strand displacement
Secondary priming
B
Fraction of the Genome with >= 1x coverage
0.3
0.4
0.5
0.6
0.7
1
2
3
4
5
6
7
8
9
10
11
12
13
Average Sequencing Depth
C
chr13
qA1
qA2
qA3.1
qA3.2
qA3.3
qA4
qA5
qB1
qB2
qB3
qC1
qC2
qC3
799 bp
113,864,300 bp
113,864,400 bp
113,864,500 bp
113,864,600 bp
113,864,700 bp
113,864,800 bp
113,864,900 bp
[0 - 21]

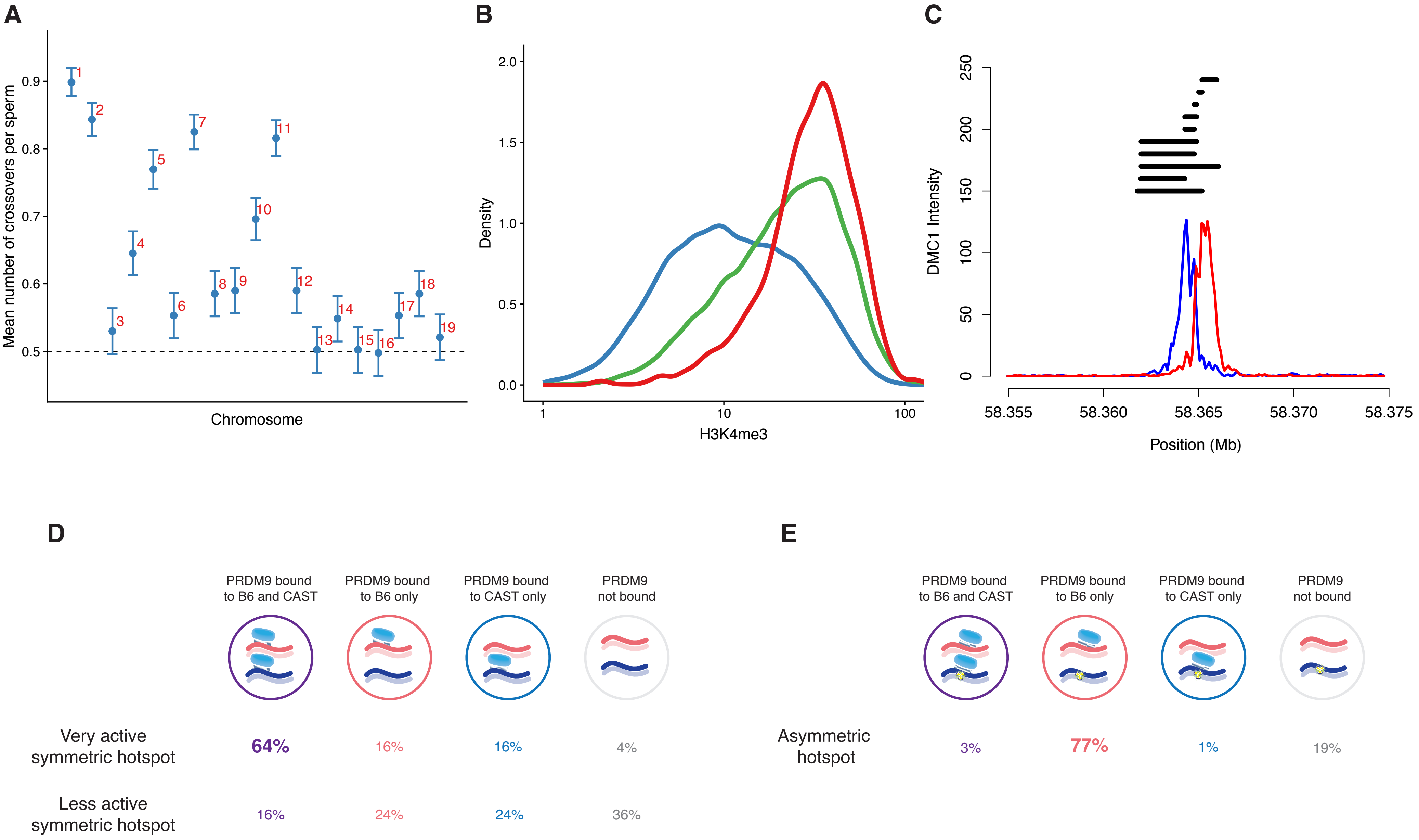
A
Mean number of crossovers per sperm
0.9
0.8
0.7
0.6
0.5
1
2
3
4
5
6
7
8
9
10
11
12
13
14
15
16
17
18
19
Chromosome
B
Density
2.0
1.5
1.0
0.5
0.0
1
10
100
H3K4me3
C
DMC1 Intensity
250
200
150
100
50
0
58.355
58.360
58.365
58.370
58.375
Position (Mb)
D
PRDM9 bound to B6 and CAST
PRDM9 bound to B6 only
PRDM9 bound to CAST only
PRDM9 not bound
Very active symmetric hotspot
64%
16%
16%
4%
Less active symmetric hotspot
16%
24%
24%
36%
E
PRDM9 bound to B6 and CAST
PRDM9 bound to B6 only
PRDM9 bound to CAST only
PRDM9 not bound
Asymmetric hotspot
3%
77%
1%
19%

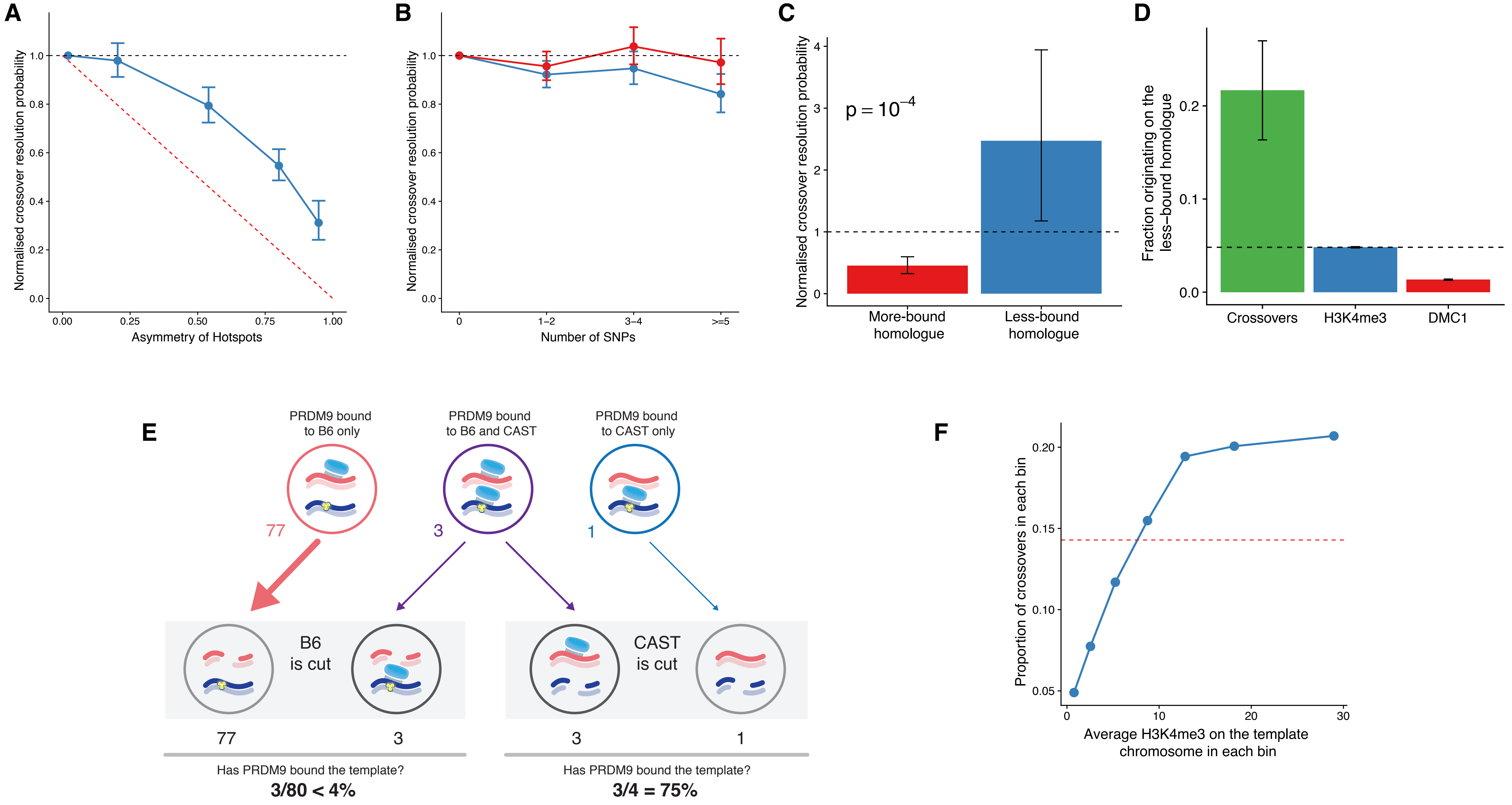
A
Normalised crossover resolution probability
1.0
0.8
0.6
0.4
0.2
0.0
0.00
0.25
0.50
0.75
1.00
Asymmetry of Hotspots
B
Normalised crossover resolution probability
1.0
0.8
0.6
0.4
0.2
0.0
0
1–2
3–4
>=5
Number of SNPs
C
Normalised crossover resolution probability
4
3
2
1
0
p = 10^−4
More-bound homologue
Less-bound homologue
D
Fraction originating on the less–bound homologue
0.2
0.1
0.0
Crossovers
H3K4me3
DMC1
E
PRDM9 bound to B6 only
PRDM9 bound to B6 and CAST
PRDM9 bound to CAST only
77
3
1
B6 is cut
CAST is cut
77
3
3
1
Has PRDM9 bound the template?
3/80 < 4%
Has PRDM9 bound the template?
3/4 = 75%
F
Proportion of crossovers in each bin
0.20
0.15
0.10
0.05
0
10
20
30
Average H3K4me3 on the template chromosome in each bin

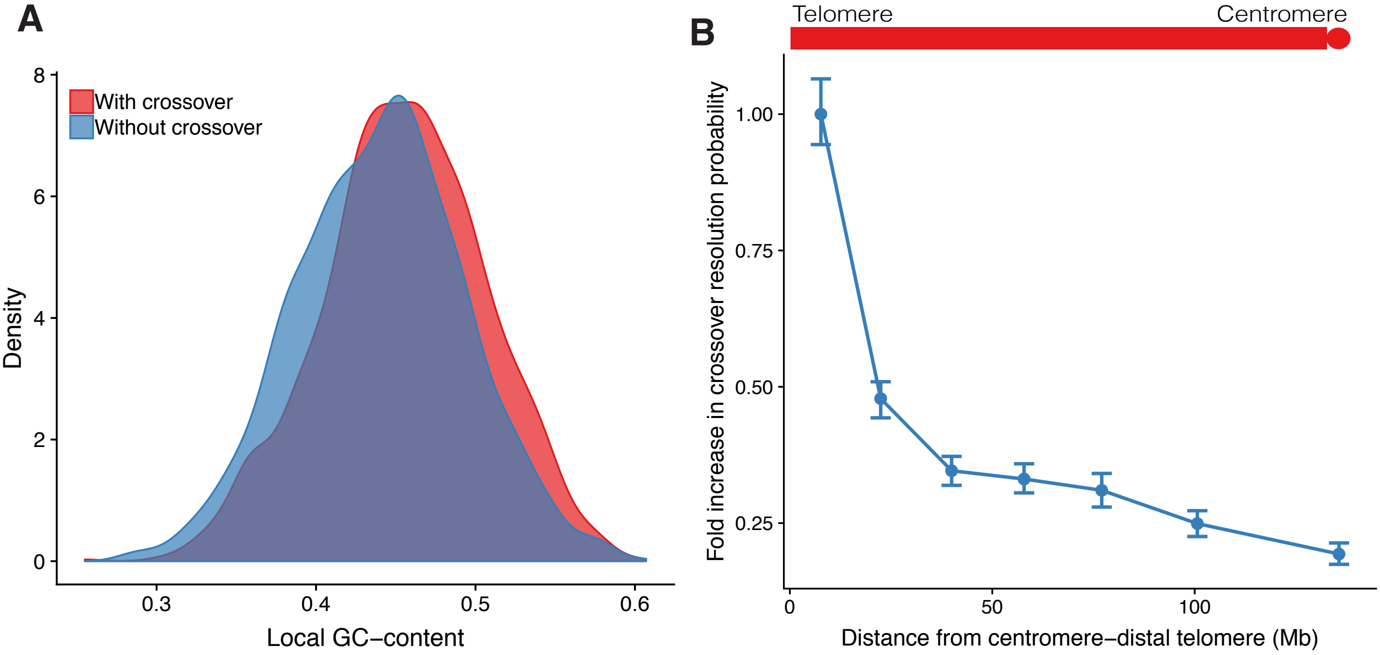
A
8
6
4
2
0
Density
With crossover
Without crossover
0.3
0.4
0.5
0.6
Local GC−content
B
Telomere
Centromere
1.00
0.75
0.50
0.25
Fold increase in crossover resolution probability
0
50
100
Distance from centromere−distal telomere (Mb)

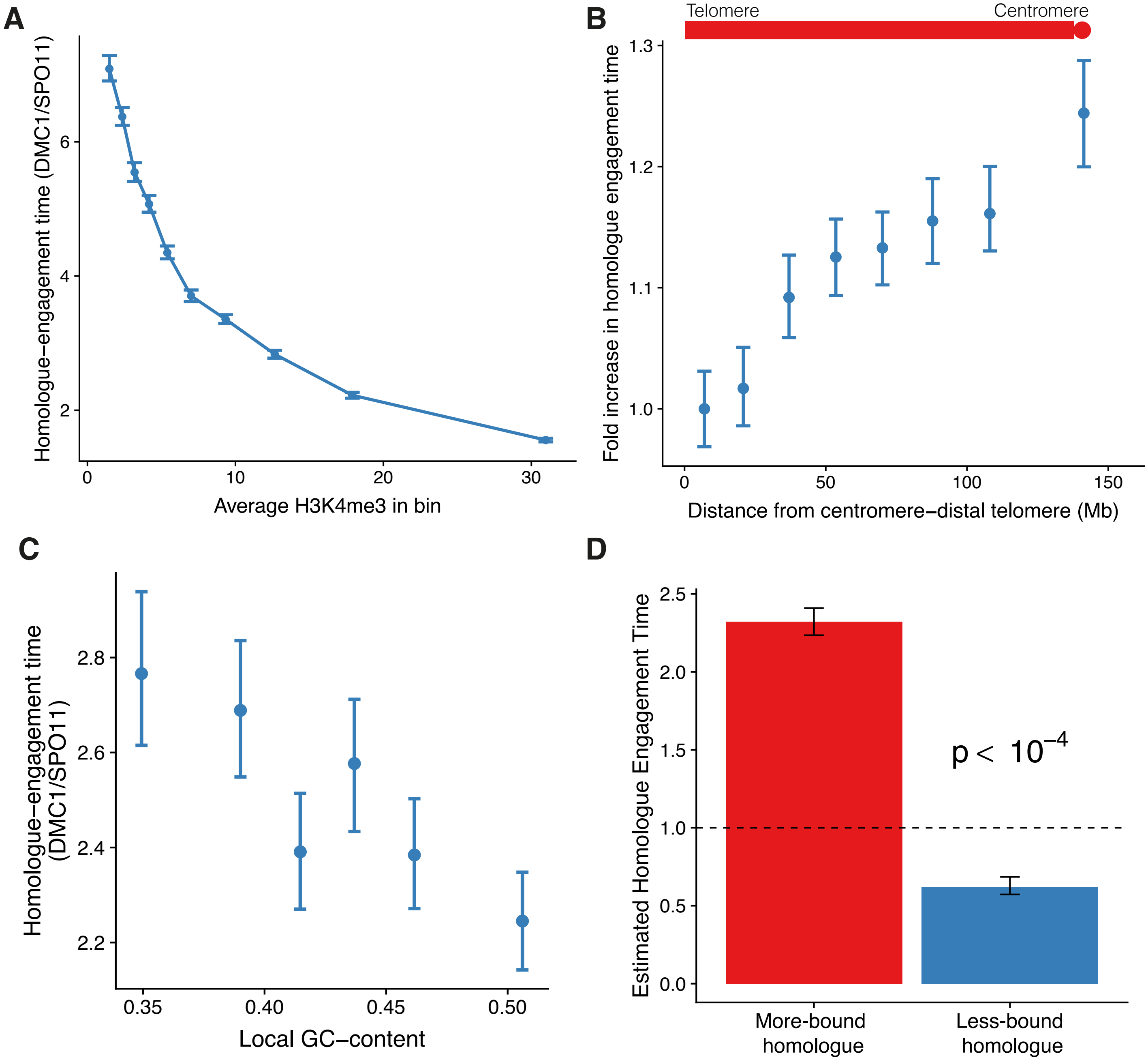
A
Homologue−engagement time (DMC1/SPO11)
6
4
2
0
10
20
30
Average H3K4me3 in bin
B
Telomere
Centromere
Fold increase in homologue engagement time
1.3
1.2
1.1
1.0
0
50
100
150
Distance from centromere−distal telomere (Mb)
C
Homologue−engagement time (DMC1/SPO11)
2.8
2.6
2.4
2.2
0.35
0.40
0.45
0.50
Local GC−content
D
Estimated Homologue Engagement Time
2.5
2.0
1.5
1.0
0.5
0.0
$p < 10^{-4}$
More-bound homologue
Less-bound homologue

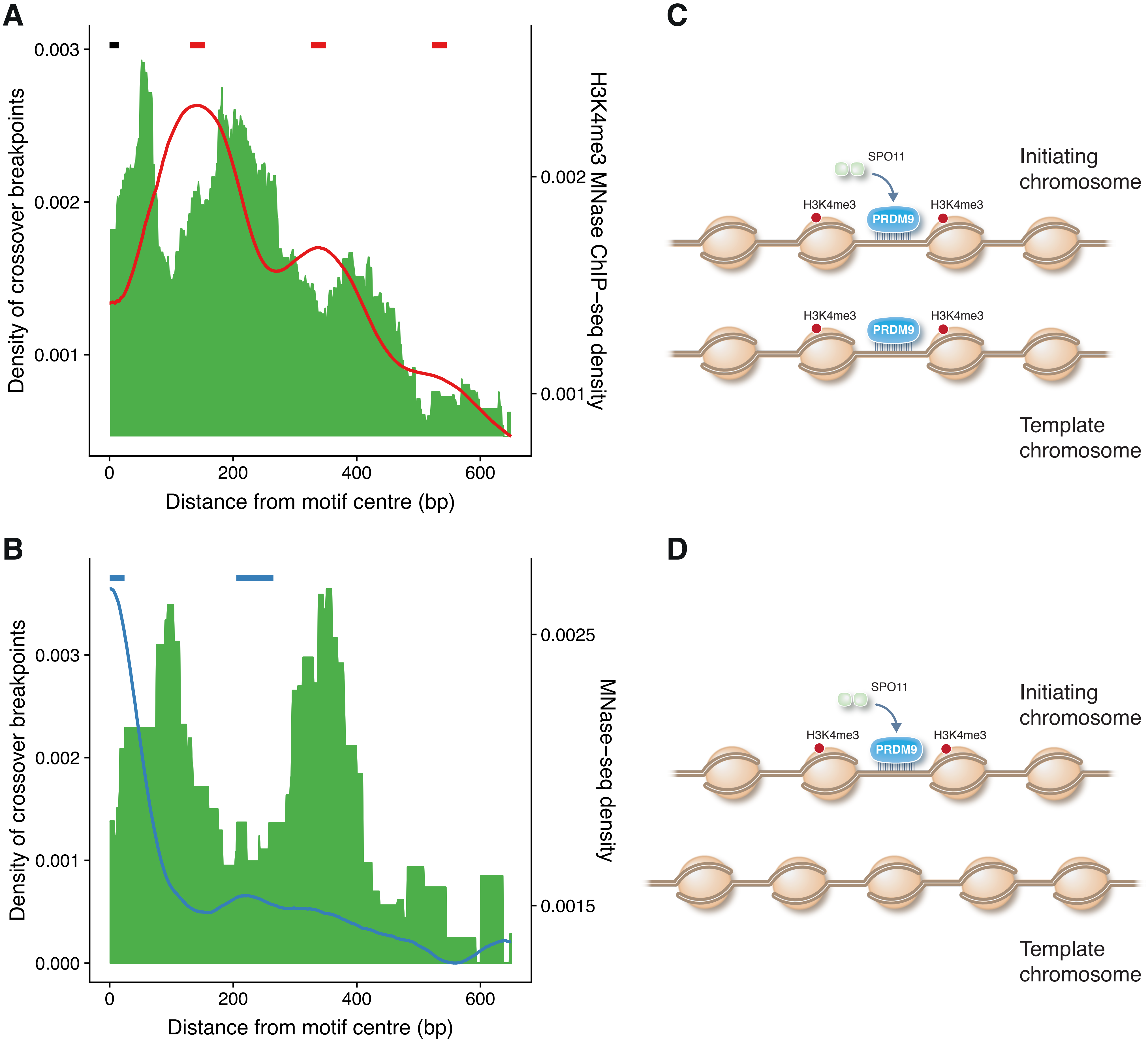
A
0.003
0.002
0.001
Density of crossover breakpoints
0.002
0.001
H3K4me3 MNase ChIP−seq density
0
200
400
600
Distance from motif centre (bp)
B
0.003
0.002
0.001
0.000
Density of crossover breakpoints
0.0025
0.0015
MNase−seq density
0
200
400
600
Distance from motif centre (bp)
C
SPO11
Initiating chromosome
H3K4me3
PRDM9
H3K4me3
H3K4me3
PRDM9
H3K4me3
Template chromosome
D
SPO11
Initiating chromosome
H3K4me3
PRDM9
H3K4me3
Template chromosome

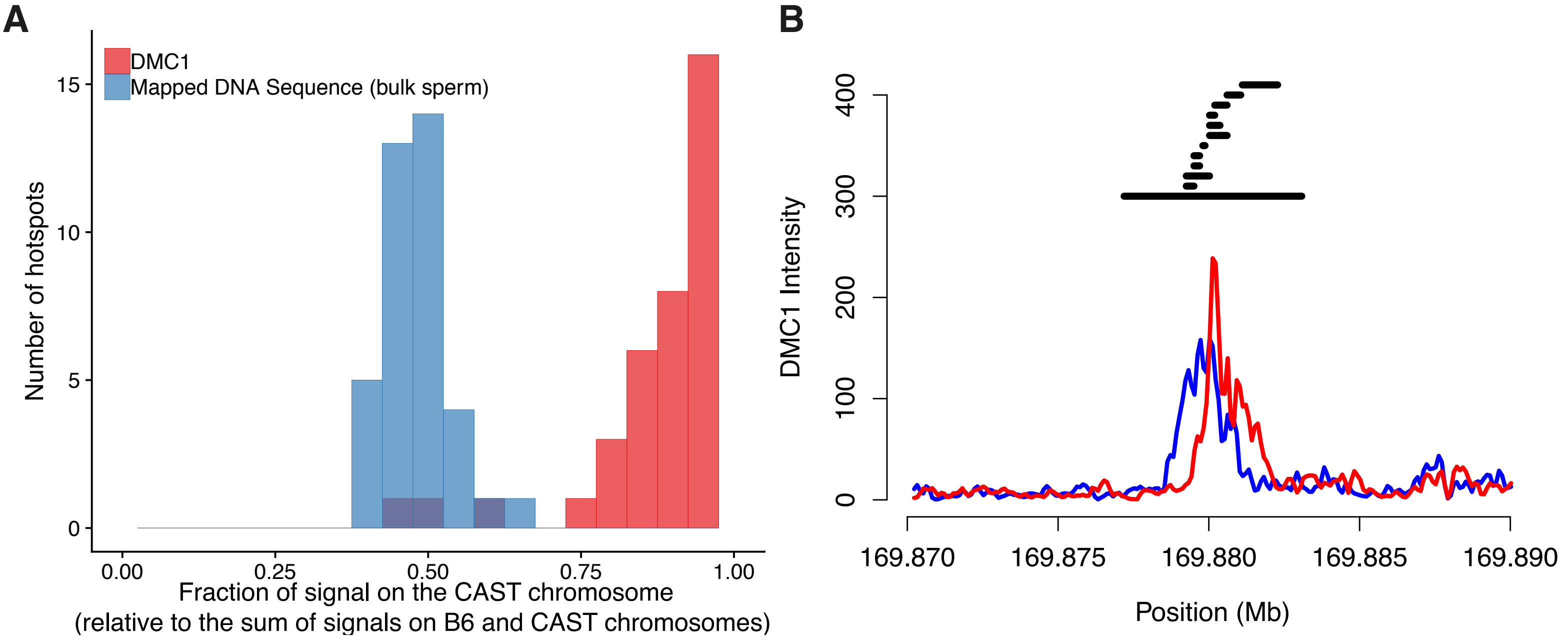
A
DMC1
Mapped DNA Sequence (bulk sperm)
Number of hotspots
0
5
10
15
0.00
0.25
0.50
0.75
1.00
Fraction of signal on the CAST chromosome
(relative to the sum of signals on B6 and CAST chromosomes)
B
DMC1 Intensity
0
100
200
300
400
169.870
169.875
169.880
169.885
169.890
Position (Mb)

Science
AAAS

Supplementary Materials for

Factors Influencing Meiotic Recombination Revealed by Whole Genome Sequencing of Single Sperm

Anjali Gupta Hinch, Gang Zhang, Philipp W Becker, Daniela Moralli, Robert Hinch, Benjamin Davies, Rory Bowden, Peter Donnelly

Correspondence to: donnelly@well.ox.ac.uk

This PDF file includes:

- Materials and Methods
- Supplementary Text
- Figs. S1 to S43
- Tables S1 to S3

Contents

1 Materials and Methods

1.1 Whole genome sequencing of single mouse sperm cells

1.1.1 Preparation of mouse sperm cells and testicle tissue

Mature sperm cells were isolated from the epididymis of a 10-week old male B6$^{\mathrm{HUM}}$ x CAST$^{\mathrm{CAST}}$ F1 mouse by incubating the tissue in 1ml of 1x PBS at 37°C for 30 minutes to allow individual mature sperm to swim out. The free sperm suspension was transferred to a fresh tube and supplemented with glycerol to a final concentration of approximately 10%. Aliquots of this sperm suspension were stored at -80°C as sample stock. Testes from the same mouse were also isolated to perform single stranded DNA sequencing analysis.

1.1.2 Isolation of individual mouse sperm cells

A proportion of the frozen mouse sperm cell stock was thawed at room temperature and then diluted with 100μl 0.9% NaCl. The sperm cell suspension was transferred on to a PEN 1.0 MembraneSlide (Zeiss), and a sperm cell smear was created by spreading the suspension across the membrane. Following incubation of the slide at room temperature for 10 minutes, the suspension was removed, and the slide was rinsed twice using 1ml 0.9% NaCl and once with ultrapure water. After shaking off the excessive liquid, the slide was allowed to dry at room temperature.

Individual intact sperm cells were isolated under 40x objective lens on a Zeiss PALM Laser Capture Microdissection microscope, and transferred to individual 0.2ml microfuge tubes containing 1μl of 0.25% polyvinylpyrrolidone. Isolated individual cells were kept on ice for further processing.

1.1.3 Cell lysis and DNA preparation

The isolated individual cells were lysed under alkaline conditions, broadly as described by Zhang *et al* *(57)*. In brief, 1 μl alkaline lysis solution (0.4 N KOH, 0.1 M DTT) was mixed with the collected individual cells. Following 10 minutes incubation on ice, the lysate was neutralised with 2 μl of neutralization solution (a mixture of 1ml 0.4 N HCl and 1 ml of 0.3 M Tris-HCl buffer, pH 8.0 at 25°C). Subsequently, 0.5 μl of proteinase K (4 mg/μl) was added to the neutralised cell lysate, and the mixture was incubated at 50°C for 12-16 hours, followed by 10 minutes at 65°C and then 10 minutes at 80°C. DNA in the treated lysate was directly used as template for whole genome amplification (WGA), as described below.

1.1.4 Whole genome amplification

To each of the prepared DNA samples from individual mouse sperm cells, 2 μl primer mix, containing 30 mM Tris-HCl (pH 8.0 at 25°C), 30 mM $MgCl_2$ and 200 μM random RNA decamer oligonucleotides, were added. The template/primer mixture was incubated at 94°C for 3 minutes, and then chilled to 0°C immediately. After mixing with 2 μl Klenow reaction mix, comprising 10 mM Tris-HCl (pH 8.0 at 25°C), 10 mM $MgCl_2$, 120 μM dNTP and 23u Klenow fragment, the samples were incubated sequentially at 30°C for 15 minutes, 37°C for 60 minutes and then 65°C for 5 minutes, followed by 94°C for 3 minutes. At the end of the incubation, the samples were chilled to 0°C immediately. To each sample, 2 μl DNA polymerase I reaction mix, consisting of 10 mM Tris-HCl (pH 8.0 at 25°C), 50 mM KCl, 120 μM dNTP and 8u E. coli DNA polymerase I, were applied. After sequential incubation at 30°C for 15 minutes, and then 37°C for 20 minutes, 40 μl Taq DNA polymerase mixture, comprising 10 mM Tris-HCl (pH 8.3 at 25°C), 50 mM KCl, 0.8 mM dNTP and 2u Taq DNA polymerase, were added to each sample. The reaction mixtures were incubated at 68°C for 20 minutes, resulting in amplified DNA.

1.1.5 Illumina sequencing library preparation and sequencing

To remove the RNA strand at the 5' end, the amplified DNA was subjected to nuclease digestion by adding 7.5 μl of S1 nuclease mix, containing 45u S1 nuclease, 50 mM NaAc (pH 4.5 at 25°C), 280 mM NaCl and 45 mM $ZnSO_4$, and incubating at 45°C for 10 minutes. At the end of the digestion, 8 μl of 100xTE, *i.e.*, 1 M Tris-HCl (pH 8.0 at 25°C) and 0.1 M EDTA, were used to stop the reaction, and DNA samples were purified using Ampure XP beads for selecting 250-500 bp DNA fragments.

Sequencing libraries were prepared essentially using a standard NEBNext library preparation protocol with some modifications: dA-tailing buffer was replaced with NEB T4 RNA ligase buffer and dATP at final concentration of 0.2 mM. After dA-tailing reaction, Klenow fragment (3'→5' exo) activity was inactivated by incubating at 65°C for 10 minutes, and the reaction mixes were directly used for ligation. Subsequently, 12 cycles of PCR were performed to generate individually indexed sequencing libraries. The individual libraries were pooled and sequenced to approximately 5x sequencing depth using Illumina HiSeq4000 150bp PE platform.

1.2 Calling variants in bulk and individual sperm

Sequencing reads for each sperm were aligned to the mouse genome assembly mm10 using `bwa v0.7.15`. Multiple bam files for the same sample were merged using `samtools v1.3` Duplicate reads were removed using `samtools rmdup` with default arguments.

1.2.1 Preparing a VCF file of variants heterozygous in the hybrid mouse

To identify the haplotype at each location for each sperm, we wished to identify the allele at every site that differs between the B6 and CAST genomes in the hybrid mouse in this study. In order to identify these sites, we sequenced bulk sperm from this mouse in two batches – a 2ng sample at 19.5X coverage and a 50ng sample at 9.4X coverage. We merged the sequencing reads from these experiments and called variants *de novo* using `platypus v0.5.2` *(58)* with default arguments. We filtered down to the variants that had the flag "PASS" for the variant call, with the variant call being heterozygous (0/1 or 1/0). We downloaded the VCF files from Mouse Genome Project (MGP) version 5 *(27)*, for single nucleotide polymorphisms (SNPs) in CAST/EiJ (`CAST_EiJ.mgp.v5.snps.dbSNP142.vcf`) and C57BL/6NJ (`C57BL_6NJ.mgp.v5.snps.dbSNP142.vcf`). We further filtered the *de novo* VCF file for variants that were homozygous reference in C57BL/6NJ (0/0) and homozygous alternative in CAST/EiJ (1/1).

1.2.2 Calling variants in each sperm

We used platypus to force-call the variants at each site identified above using the following parameters: `minPosterior` = `0`, `getVariantsFromBAMs` = `0`. Other parameters were the default parameters in `platypus v0.5.2`. This produces a VCF for each sperm sample with a variant call at each location in the filtered *de novo* VCF generated above (Section 1.2.1). Next, we called crossovers in 217 sperm, after excluding three sperm that showed evidence of contamination.

1.3 Calling crossover events

We used a Hidden Markov Model (HMM) to identify the most likely sequence of haplotypes while accounting for genotyping error in read calls. To identify crossovers in the PAR, the same approach was used, with the exception that all SNPs in the X-only region outside the het-PAR were removed (genome coordinates chrX:1-169542068) (Fig. S39). We retained SNPs in the het-PAR and B6 PAR. For each chromosome in each sperm, we did the following:

- *Sites.* In the VCF file for each sperm, all locations that were called heterozygous (0/1) or (1/0) were removed. This is because each sperm sample is expected to be haploid, and a heterozygous call is likely to be due to sequencing or mapping errors. Further, variant calls where the quality was flagged as “MQ”, “badReads” or “HapScore” were filtered out.

- *Observations.* Platypus generates a posterior log-likelihood for each variant call using a diploid model. Specifically, it outputs the posterior $\log_{10}$-likelihood of each of the three possible diploid states 00, 01 and 11 (where 0 represents the reference and 1 represents the alternative allele) based on the likelihood of sampling the observed reads and a prior on the diploid states. Since there is no information about allele frequencies in the VCF, the prior is assumed to be $p_{00} = 0.25, p_{01} = 0.5, p_{11} = 0.25$ at each site. We transform the log-likelihoods into haploid likelihoods by changing the prior to $p_{00} = 0.5, p_{11} = 0.5$. The ‘observations’ for this HMM are the transformed haploid likelihoods at each site: if the log-likelihoods from platypus at a particular site are $l_{00} : l_{01} : l_{11}$, the corresponding ‘observations’ are simply $d_1 = 10^{l_{11}}$ and $d_0 = 10^{l_{00}}$.

- *States.* Each euploid sperm is expected to be composed of segments of B6 and CAST genomes. This sequence of segments represents the underlying hidden states we wish to infer. At each site i, there are two possibilities for the hidden state s_i. If $s_i = 0$, it means that the B6 chromosome was inherited in this sperm at site i and $s_i = 1$ means the CAST chromosome was inherited.

- *Emission probabilities.* We assumed that there is additional uncertainty in the observed likelihoods above. We used an additional parameter e, to generate the emission matrix: the emission probabilities are $p(d_0, d_1|s = 1) \propto \frac{d_1+e}{d_1+d_0+2\times e}$ and conversely $p(d_0, d_1|s = 0) \propto \frac{d_0+e}{d_1+d_0+2\times e}$ We chose $e = 0.1$.

- *Transition probabilities.* For sites i and j, transition from $s_i = 0$ to $s_j = 1$ reflects a crossover event from B6 at site i to CAST at site j in the parental hybrid mouse. To avoid biasing the calling of crossover events, we picked a uniform transition matrix corresponding to a crossover rate of 1 cM per Mb for the autosomes and 50 cM per Mb for the PAR. The transition probability of a change in state between sites i and j is set to be $p_{ij} = 1 - e^{-d_{ij}\times 10^{-8}}$ on the autosomes and $p_{ij} = 1 - e^{-d_{ij}\times 10^{-8}\times 50}$ on the PAR where d_{ij} is the distance between the sites i and j (in bp).

- *Initial probabilities.* Since both haplotypes are equally likely to be transmitted *a priori* we set the initial probabilities $\pi(0) = \pi(1) = 0.5$.

We used the Viterbi algorithm to infer the most likely sequence of states in the Hidden Markov Model. Every change in state inferred using the Viterbi algorithm represents a putative crossover event. We often see “double” crossovers, with two transitions within a few SNPs of each other. While these may represent non-crossover events or genuine crossover events near each other, we take the conservative approach and filter out transitions within 100 SNPs of each other. Given that such double crossovers have $\leq$100 SNPs of support, and our sequencing data has generally low depth, it is more likely that they are false-positives. We also see an excess of multiple transitions in a region of chromosome 6 between $\sim$ 33Mb and $\sim$ 60 Mb. We note that this region is not fully inbred in CAST or B6, and therefore violates the assumptions made in our approach. We therefore require a higher burden of proof ($\geq$1000 SNPs) for double crossovers in this region. We require at least 30 SNPs of support to call a crossover at the ends of chromosomes.

1.4 DMC1 ChIP-seq and hotspot calling

We performed single-stranded DNA sequencing (SSDS) DMC1 ChIP-seq as previously described *(37)*, using testes from the same animal from whom sperm was harvested.

In brief, mouse testicle tissues were fixed in 1% formaldehyde and homogenised in a 15ml Dounce homogeniser using a tight fit pestle. Cells were then collected by centrifugation at 900g and washed with cold PBS. After lysis of the cells with buffer containing 0.25% Triton X-100, the nuclei fraction was suspended in shearing buffer containing 1% SDS, and sonicated for 15 cycles of 15s on and 45s off under high intensity using a Bioruptor, in order to fragment chromatin DNA to a peak size approximately 500-1000bp. The fragmented chromatin was centrifuged at 12,000g and 4°C for 10 minutes, and the supernatant was dialysed against buffer containing 0.01% SDS and 1% Triton X-100 for 4 hours. Dialysed chromatin was immunoprecipitated against anti-DMC1 antibody (sc-8973, Santa Cruz) overnight at 4°C.

Antibody bound chromatin was pulled down using Dynabeads Protein G, washed and then eluted from the beads by incubating the beads at 65°C in elution buffer containing 0.1M $NaHCO_3$ and 1% SDS, followed by reverse crosslinking at 65°C overnight.

The DNA was purified using MinElute PCR Purification kit, and used for SSDS library preparation. Following dA-tailing, DNA was incubated at 95°C for 3 minutes, and then chilled to room temperature quickly to enrich single stranded DNA. After adding sequencing adaptors, SSDS library was amplified for 12 cycles using Illumina TruSeq protocol. The amplified library was purified, and sequenced on HiSeq2500 using 50bp PE rapid run.

We ran a bioinformatic pipeline on the resulting reads for identifying single-stranded sequences *(37)*. Hotspot centres were called using our published peak-calling algorithm *(26)*. To assess overlap with crossovers, hotspot end points were defined as ± 1000 bp from the hotspot centre. For each hotspot, we also infer the fraction of reads that originated from the B6 and the CAST chromosomes respectively, as previously described *(26)*.

To identify false-positive hotspots, a list of ‘blacklisted’ peaks was generated by performing the steps of the ChIP-seq protocol, as above, but without use of a functional antibody against DMC1. This experiment was performed on the testes of a B6 wild-type mouse, and peaks were called using the peak-calling algorithm, as above. Any hotspot that overlapped one or more of these peaks was filtered out.

For analyses requiring quantitative measurements of PRDM9-dependent H3K4me3 in PRDM9$^{\text{CAST}}$ and PRDM9$^{\text{HUM}}$ hotspots, DMC1 hotspots that showed evidence of H3K4me3 independently of PRDM9 binding, for example, at some transcription-start sites, were filtered out. See Section 1.8 for how this evidence was assessed.

1.5 Inferring the PRDM9 variants activating DMC1 hotspots

The *Prdm9* alleles in the hybrid mouse in this work are *Prdm9*$^{\text{HUM}}$ and *Prdm9*$^{\text{CAST}}$. In addition, we anticipate that a subset of recombination hotspots may be activated independently of PRDM9 *(32)*. To infer which hotspots are activated by each of these PRDM9 variants, or independently of them, we leverage DMC1 hotspots from a range of mice with a variety of *Prdm9* alleles: CAST$^{\text{CAST}}$ *(32)*, B6$^{\text{HUM}}$ *(26)*, B6$^{\text{HUMxB6}}$ *(26)*, B6$^{\text{B6}}$ *(42)*, PWD$^{\text{PWD}}$ *(26)*, B6xCAST$^{\text{B6xCAST}}$*(26)*, CASTxB6$^{\text{B6xCAST}}$ *(32)*, B6xCAST$^{\text{HUMxCAST}}$*(26)*, PWDxB6$^{\text{B6xPWD}}$ *(26)*, B6xPWD$^{\text{B6xPWD}}$*(26)*, PWDxB6$^{\text{HUMxPWD}}$*(26)*, B6xPWD$^{\text{HUMxPWD}}$*(26)*, three (CAST/B6)F2$^{\text{B6xHUM}}$ mice *(26)*, a mouse with an additional *Prdm9* allele, and one mouse lacking any functional *Prdm9* allele B6$^{\text{KO}}$ *(42)*.

We created a superset of hotspots, which are combined across mice such that hotspots that have their centres within 600 bp of each other are merged to form a single hotspot. For each hotspot in the superset, we then created a maximal set of PRDM9 variants that could potentially be responsible for activating it. For example, if a hotspot overlaps hotspots in CASTxB6$^{\text{B6xCAST}}$, B6xCAST$^{\text{B6xCAST}}$, and B6xCAST$^{\text{HUMxCAST}}$, the potential set of variants that could activate the hotspot is $\{$PRDM9$^{\text{B6}}$, PRDM9$^{\text{CAST}}$, PRDM9$^{\text{HUM}}\}$. From the maximal set, we reduce to a minimal set that can explain all of the hotspots in the set. In this example, it is PRDM9$^{\text{CAST}}$. Hotspots for which the minimal set contains a single PRDM9 variant are inferred to be activated by it.

There are two special cases:

- Hotspots in B6$^{\text{KO}}$ are assumed to have arisen from a dummy allele, called PRDM9$^{\text{KO}}$
- PRDM9$^{\text{CAST}}$ and PRDM9$^{\text{PWD}}$ have similarities in their zinc finger arrays and a large number of overlapping hotspots *(32)*. If the maximal set contains both of them, we treat them as equivalent and interchangeable. For example, if a hotspot overlaps B6xCAST$^{\text{HUMxCAST}}$ and PWD$^{\text{PWD}}$, the maximal set contains PRDM9$^{\text{HUM}}$, PRDM9$^{\text{CAST}}$, and PRDM9$^{\text{PWD}}$. However, the minimal set is reduced to PRDM9$^{\text{CAST+PWD}}$, meaning either PRDM9$^{\text{CAST}}$or PRDM9$^{\text{PWD}}$.

It is not always possible to reduce the minimal set to a single PRDM9 variant. For example, if a hotspot is found in CASTxB6$^{\text{B6xCAST}}$, B6xCAST$^{\text{HUMxCAST}}$,CAST$^{\text{CAST}}$ and B6$^{\text{HUM}}$, then no single PRDM9 variant can explain all the hotspots. The minimal set cannot be reduced further from $\{$PRDM9$^{\text{CAST}}$, PRDM9$^{\text{HUM}}\}$. In this case, we take the following approach to assign alleles in the B6xCAST$^{\text{HUMxCAST}}$ mouse that is of interest in this work:

1. For hotspots where the minimal set contains both PRDM9$^{\text{CAST}}$ and PRDM9$^{\text{HUM}}$, but not PRDM9$^{\text{KO}}$, the type is unknown.

2. For hotspots where the minimal set contains PRDM9^{CAST}, but not PRDM9^{HUM} or PRDM9^{KO}, the type is PRDM9^{CAST}

3. For hotspots where the minimal set contains PRDM9^{HUM}, but not PRDM9^{CAST} or PRDM9^{KO}, the type is PRDM9^{HUM}

4. For hotspots where the minimal set contains PRDM9^{KO}, but not PRDM9^{CAST} or PRDM9^{HUM}, the type is PRDM9^{KO} (i.e. PRDM9-independent)

5. PRDM9-independent hotspots present a special case in that they are often present at low intensity in mice with functional PRDM9 variants, in addition to being present in B6^{KO}. In these cases, the minimal set will contain PRDM9^{KO} in addition to numerous other variants. In order to distinguish genuine PRDM9^{KO} hotspots from chance overlap with PRDM9^{HUM} or PRDM9^{CAST} hotspots, we take a conservative approach. We require that additional PRDM9 variants (e.g. PRDM9^{B6}) be present in the minimal set for the hotspot to be deemed PRDM9^{KO}. In other words, if the minimal set includes B6^{KO} and more than one variant in addition to the alleles PRDM9^{HUM} or PRDM9^{CAST}, we assign the type as PRDM9^{KO}, otherwise the type is unknown.

1.6 H3K4me3 ChIP-seq

H3K4me3 ChIP-seq was performed by Li et al *(28)*. Their method is reproduced with permission as follows:

“We performed ChIP-seq against H3K4me3 as previously described *(26)* with several important modifications that increased ChIP stringency (noted here). An 8-week-old male (B6^{HUM} x CAST^{CAST} F1) was culled and the testes were immediately removed. Each testis was processed separately as a replicate. The testis tunica was removed, and the tubules were dissociated with tweezers and fixed in 1% formaldehyde in PBS for 5 minutes followed by glycine quenching (125 mM final concentration) for 5 minutes at room temperature. Following washing steps, pellets were resuspended in 900 μl cold 1%SDSlysisbuffer(1% SDS, 10 mM EDTA, 50 mM Tris pH 8.0, 2x protease inhibitors), dounced 20 times and sonicated in 300 μl aliquots in a Bioruptor Twin sonication bath at 4°C for three 5-minute periods of 30s on, 30s off at high power, then cell debris were pelleted and removed and aliquots were pooled. Samples were then diluted 1:10 in IPwashbuffer (100 mM Tris pH 7.5, 500 mM LiCl,1% NP-40,1% Na deoxycholate, 2x Protease Inhibitor, filtered). For each sample, 100 μl of magnetic beads (with no primary antibody; Invitrogen Sheep Anti-Rabbit Dynabeads) were washed and resuspended three times in PBS/BSA (1X PBS, 5 mg/ml BSA, 1 tablet Roche Complete protease inhibitor per 50 ml, filtered with 0.45-micron filter) to a final volume of 100 μl and added to the chromatin samples for pre-clearing for 2 hours at 4°C with rotation. Beads were removed, and 100 μl of pre-cleared chromatin was set aside for the input control. 5 μl rabbit polyclonal anti-H3K4me3 antibody (Abcam ab8580) was added to the remaining pre-cleared chromatin and incubated overnight at 4°C with rotation. 50 μl fresh beads were washed and resuspended in PBS/BSA as before, then incubated with the chromatin samples for 2h at 4°C with rotation. Beads were then washed 5 times for 3 minutes each with cold IP wash buffer (with rotation), then washed once with cold 1X TE (10 mM Tris-HCl pH 7.5, 0.1 mM Na 2 -EDTA). Bead pellets were resuspended in 200 μl room-temperature IP elution buffer (1% SDS, 0.1 M NaHCO 3 , filtered with a 0.45-micron filter unit) and vortexed to mix. For input controls, 50 μl of pre-cleared chromatin was added to 150 μl IP elution buffer. Samples were incubated in a 65°C water bath for 1 hour with mixing at 15-minute intervals to uncouple beads from protein-DNA complexes. Samples were centrifuged (14,000 rpm, 3 mins) and placed on a magnet to pellet beads, and supernatants were isolated and then incubated at 65°C overnight to reverse crosslink. After de-crosslinking, samples were further incubated with 80 μg RNAse A at 37°C for 60 minutes and then with 80 μg Proteinase K at 55°C for 90 minutes. DNA was purified using a Qiagen MinElute reaction cleanup kit, yielding roughly 1 ng per testis (owing to higher stringency antibody incubation in wash buffer). ChIP and total chromatin DNA samples were sequenced in multiplexed paired-end Illumina HiSeq2500 libraries (rapid run), yielding 60-70 million 51-bp read pairs per replicate."

1.7 Quantifying the H3K4me3 intensity in DMC1 hotspots and calling H3K4me3 peaks *de novo*

We have developed an algorithm, which leverages the data above to quantify the evidence of enrichment in H3K4me3 in the ChIP sample while using the input control to account for sequencing biases and differences in mappability across the genome. We pooled the data from the two ChIP replicate samples above to get a single ChIP sample.

For brevity, we refer to the ChIP sample as 'signal' and the input background control sample as 'control'. Let N_s and N_c be the random variables representing the sequencing fragment coverage at any given location or region in the signal and control, respectively. We model N_s and N_c as samples from Poisson distributions:

$$N_c \sim \mathcal{P}(\lambda)$$

$$N_s \sim \mathcal{P}(\lambda\beta)$$

where λ is the underlying intensity of the number of reads in the control experiment. Our aim is to obtain an estimator for β, as it represents the fold-enrichment in signal above background.

Assuming a flat prior on λ, we have the likelihood

$$\begin{aligned} P(N_c = n_c, N_s = n_s|\beta) &\propto \int_0^\infty \frac{\lambda^{n_c}(\lambda\beta)^{n_s}e^{-\lambda(1+\beta)}}{n_c!n_s!}\mathrm{d}\lambda \\ &\propto \frac{\beta^{n_s}}{(1+\beta)^{n_c+n_s+1}}\binom{n_s+n_c}{n_c} \end{aligned}$$

where n_c and n_s are the observed fragment coverage in the control and signal respectively at the location of interest. The MLE for β is then given by:

$$\tilde{\beta}_{MLE} = \frac{n_s}{n_c+1}.$$

This estimator is problematic in that it is highly biased when n_c is small. Note that when $n_c = 0$, $P(N_c = n_c, N_s = n_s|\beta)$ does not form a proper distribution. One way to solve this problem is to put informative priors on β and λ, however, the subsequent estimate of β for small n_c becomes highly dependent on the choice of prior. An alternative way to estimate β is to consider the conditional distribution of N_c given N_s.

$$\begin{aligned} P(N_c = n_c|N_s = n_s, \beta) &= \frac{P(N_c = n_c, N_s = n_s)}{\sum_{k=0}^{\infty} P(N_c = k, N_s = n_s)} \\ &= \frac{\beta^{n_s+1}}{(1+\beta)^{n_c+n_s+1}}\binom{n_s+n_c}{n_c} \end{aligned}$$

where we have used the identity $\sum_{k=0}^{\infty}\alpha^k\binom{n+k}{k} = (1-\alpha)^{-n-1}$. For a given value of β, the distribution of N_c can be wide. To get a robust estimator, we choose $\tilde{\beta}$ so that the observed value of reads on the control lane n_c is the median of this distribution (we note that it is not necessary to use the median, and an alternative quantile may be used).

$$P(N_c \leq n_c|N_s = n_s, \tilde{\beta}) = 0.5.$$

We solve this equation for $\tilde{\beta}$ by searching for a root (using `uniroot`) in a reasonable interval. Note that this estimates β up to a re-scaling factor. A genome-wide re-scaling factor f is calculated as the ratio of the median depths of coverage in 500bp bins across the genome in the control and in the signal. Our estimate for the H3K4me3 intensity in signal is $\tilde{\beta} f$. We refer to this as force-calling H3K4me3 at a given location.

Our estimate of the H3K4me3 intensity at each DMC1 hotspot is, correspondingly, $\tilde{\beta} f$ in the 1 kb region centered at the DMC1 hotspot centre.

In the event that there continue to be outlying estimates due to n$_c$ being small, there are two options: (1) a more conservative quantile may be used genome-wide (2) the average number of reads from a larger interval centered around the region of interest could be used as the control (also genome-wide).

Separately, we also perform *de novo* peak calling for H3K4me3 without using DMC1 hotspots as reference. We calculate $\tilde{\beta}$ in 500bp moving windows, with a 100bp slide between the starting points of adjacent windows. In each window, we also calculate a p-value that the rate in the control is less than in the signal, i.e. $P(N_c \leq n_c | N_s = n_s, 1/f)$. We get an initial set of peaks by including all windows with p-value $< 10^{-6}$. We then merge overlapping peaks. Within every distinct non-overlapping merged region thus obtained, we identify the centres and intensities of individual peaks by performing hierarchical clustering using univariate Gaussian mixture models with variable variance using `mclust`. We called 144,290 H3K4me3 peaks in total, amongst which we inferred 66,352 to be due to PRDM9 binding. The reported start and end points of the peaks are the start and end points of the central 85% confidence intervals of each peak.

We also inferred the fraction of the H3K4me3 signal originating from each of the B6 and CAST chromosomes. We calculate the maximum likelihood estimate for the ratio following the same procedure as for DMC1, as described in *(26)*.

1.8 Identifying hotspots with PRDM9-independent H3K4me3

As discussed above, for autosomal analyses using quantitative estimates of PRDM9-dependent H3K4me3, we filter out hotspots that show evidence of PRDM9-independent H3K4me3, such as some promoters and enhancers. The reason for this is that the assay for H3K4me3 uses whole-testis preparation, which includes a substantial proportion of non-meiotic cells. The H3K4me3 signal at promoters and enhancers is often much greater than the signal at recombination hotspots, and dwarfs the biologically relevant value. To assess the evidence for PRDM9-independent H3K4me3, we use other mice with a variety of *Prdm9* alleles for comparison. For DMC1 hotspots which have PRDM9$^{\text{CAST}}$ but not PRDM9$^{\text{HUM}}$ in the minimal set (as described in Section 1.5), we force-call the H3K4me3 intensity in B6$^{\text{HUM}}$, B6$^{\text{HUMxB6}}$, B6$^{\text{B6}}$ and three (CAST/B6)F2$^{\text{B6xHUM}}$ mice *(26)*, none of which have the *Prdm9*$^{\text{CAST}}$ allele. If any of them has strong evidence of H3Kme3 enrichment, i.e., a p-value $< 10^{-20}$, we mark the hotspot as having PRDM9-independent H3K4me3. For DMC1 hotspots which have PRDM9$^{\text{HUM}}$ but not PRDM9$^{\text{CAST}}$ in the minimal set, we do the same analysis with B6$^{\text{B6}}$, PWDxB6$^{\text{B6xPWD}}$ and B6xPWD$^{\text{B6xPWD}}$ *(26)*, none of which have the *Prdm9*$^{\text{HUM}}$ allele. For hotspots where both are in the minimal set, we used only B6$^{\text{B6}}$. For hotspots which included PRDM9$^{\text{KO}}$ in the minimal set, we used H3K4me3 for mice whose allelic types did not overlap with any in the minimal set. This was not always possible, for example, in the case of hotspots that were found in all available mice (e.g. some of the most intense hotspots in the PAR). In those cases, the hotspots were marked as having PRDM9-independent H3K4me3.

1.9 *Prdm9* expression analysis

Oligo-dT primed cDNA from total testis RNA was prepared from three wild-type B6, three homozygous humanized B6 and three hybrid mice. Q-PCR analysis of *Prdm9* transcript levels was performed on this cDNA with three sets of exon spanning primer pair in order (5'- GCTATGAGTATGTGGATGGACAGG-3' and 5'-CCGGCAGGTTCGATAGAAGATT-3'; 5'-AAGGATTCACAGCAGGAAGAG-3' and 5'-CATTGCTGGCCTTGTCATTT-3'; 5'-GGGAAGCAAGATGAAGAAAGGA-3' and 5'-TGTTCCTGAAGCTGATCTGAAC-3'), normalizing against a housekeeping gene (*Hprt*; 5'-AGCTACTGTAATGATCAGTCAACG-3' and 5'-AGAGGTCCTTTTCACCAGCA-3') using the Power SYBR Green PCR Master mix (Applied Biosystems) and a BioRad CFX96 cycler as per manufacturer's instructions.

1.10 MNase-seq and MNase ChIP-seq

MNase-seq and MNase ChIP were performed as described previously with some modifications *(59)*. Whole, de-tunicated, fresh frozen testes of adult mice were thawed in 1% formaldehyde (Pierce) in PBS at room temperature and immediately homogenized in a Dounce tissue grinder with 10 strokes using the loose-fitting pestle. The homogenate was passed through a 70μm cell strainer, and after a total of 10 min, fixation was stopped by adding 2.5M glycine to a final concentration of 125mM followed by 5 min incubation at room temperature.

Cells were pelleted by centrifugation at 900g for 3 min, washed once in cold PBS and incubated in 5 ml hypotonic lysis buffer (10 mM Tris-HCL pH 8.0, 1 mM KCl, 1.5 mM $MgCl_2$) supplemented with EDTA-free Protease Inhibitor (Roche) for 15 min on ice. Next, cells were sheared in Dounce tissue grinder with 10 strokes using the tight-fitting pestle. Nuclei were pelleted by 10 min centrifugation at 10,000g, 4°C and resuspended in 780μl MNase buffer (50 mM Tris, 1 mM CaCl, 4 mM $MgCl_2$, 1% Triton X-100), supplemented with EDTA-free Protease Inhibitor. Chromatin was fragmented by digestion with 30 units of micrococcal nuclease (Thermo) for 4 min at 37°C after which it was chilled on ice and enzyme activity was inhibited by adding EDTA to a final concentration of 10 mM. Chromatin was clarified by 10 min centrifugation at 4°C, 17,000g and transferred to a new tube. Successful digestion to predominantly mononucleosomal levels was assessed by TapeStation (Agilent) analysis of purified DNA.

At this point 10μl of digested chromatin were reserved to perform MNase-seq, which also served as the input sample for MNase-ChIP.

Sheep Anti-Rabbit IgG Dynabeads (Thermo, 50μl M-280) were washed 3 times with cold 0.5% BSA in PBS and incubated with 5μg Rabbit Anti-H3K4me3 antibody (Abcam, ab8580) in 1 ml of cold 0.5% BSA in PBS for at least 1h on a rotating wheel. Afterwards, the beads were washed twice with cold 0.5% BSA in PBS, and resuspended in 100μl cold 0.5% BSA in PBS. Next, 500 μl TE buffer, 300 μl Binding Buffer (10% Triton X-100, 10% Sodium Deoxycholate, 10X Halt Protease Inhibitor Cocktail (Thermo)), and 200 μl 5M NaCl were added to the beads before 300μl chromatin were added and immunoprecipitation was performed overnight at 4°C on rotating wheel.

Beads were washed with Wash Buffer 1 (0.1% SDS, 1% Triton X-100, 2mM EDTA, 20mM Tris-HCl [ph = 8], 150 mM NaCl), Wash Buffer 2 (0.1% SDS, 1% Triton X-100, 2mM EDTA, 20mM Tris-HCl [ph = 8], 500 mM NaCl), and Wash Buffer 3 (2.5M LiCl, 1% IGEPAL-CA630, 1% Deoxycholic acid, 1mM EDTA, 10mM Tris-HCl [ph = 8]) for 5 min at 4°C each, followed by two brief washes with cold TE. Next, beads were incubated with 100μl Elution buffer (0.1M $NaHCO_3$, 1% SDS) for 30 min at 65°C after which the supernatant was collected in a new tube and NaCl was added to a final concentration of 200mM.

Samples were incubated at 65°C overnight for reverse crosslinking. At this stage reverse crosslinking was also performed for the Mnase-seq sample by adding 100 μl Elution buffer to the 10 μl of digested chromatin and incubating at 65°C overnight. Finally, both samples were digested with 60 μg Rnase for 30 min at 37°C and 60 μg Proteinase K for 45 min at 55°C, and purified using ChIP DNA Clean & Concentrator Kit (Zymo Research). Yield was measured using Qbit (Thermo).

2 Supplementary Text

2.1 Comparison of H3K4me3 and SPO11 measures in the B6 mouse

We leveraged two ChIP-seq experiments for H3K4me3 in the B6 mouse to estimate the magnitude of experimental uncertainty in these experiments, including one previously published experiment *(26)*. The H3K4me3 intensities for both experiments were estimated as per the procedure in Section 1.7. Data for the two experiments were pooled together, and H3K4me3 intensities using the pooled data were also estimated using the same procedure. The correlations between H3K4me3 experiments and between H3K4me3 and SPO11-oligo measures reported below, and in the main text, are performed with a log-transform, as per previous work *(29)*. The log-transform stabilises the variance *(60)*, and we checked that the residuals were well-modelled by a normal distribution.

Let H_1 and H_2 be the measurements in the two experiments above for the true underlying H3K4me3 measure H, where H_1 is the previously published experiment, and H_2 is the newly performed experiment. We assume that the experimental errors are independent, normally distributed random variables with mean zero, and variances σ_1^2 and σ_2^2 respectively:

$$H_1 = H + \epsilon_1, \epsilon_1 \sim N(0, \sigma_1^2)$$

$$H_2 = H + \epsilon_2, \epsilon_2 \sim N(0, \sigma_2^2).$$

We measure their correlation with each other, and with the SPO11-oligo intensities in the B6 mouse *(29)*. We denote the SPO11-oligo intensities as S_1. We denote the variance of random variable X as $\mathrm{Var}[X]$, the covariance between two random variables X and Y as $\mathrm{Cov}[X, Y]$, and their correlation as $\rho_{X,Y}$. The covariance between the two H3K4me3 experiments is

$$\mathrm{Cov}[H_1, H_2] = \mathrm{Cov}[H + \epsilon_1, H + \epsilon_2]$$

By the independence of H, ϵ_1 and ϵ_2, we have

$$\mathrm{Cov}[H_1, H_2] = \mathrm{Cov}[H, H] = \mathrm{Var}[H]$$

Therefore, we have for the correlation between H_1 and H_2,

$$\rho_{H_1,H_2} = \frac{\mathrm{Cov}[H_1, H_2]}{\sqrt{\mathrm{Var}[H_1]\mathrm{Var}[\mathrm{H}_2]}} = \frac{\mathrm{Var}[H]}{\sqrt{\mathrm{Var}[H_1]\mathrm{Var}[H_2]}} \tag{1}$$

For the correlation between H_1 and S_1, we have due to the independence of ϵ_1 and S_1

$$\rho_{H_1,S_1} = \frac{\mathrm{Cov}[H_1, S_1]}{\sqrt{\mathrm{Var}[H_1]\mathrm{Var}[\mathrm{S}_1]}} = \frac{\mathrm{Cov}[H, S_1]}{\sqrt{\mathrm{Var}[H_1]\mathrm{Var}[\mathrm{S}_1]}} \tag{2}$$

and similarly for H_2 and S_1,

$$\rho_{H_2,S_1} = \frac{\mathrm{Cov}[H_2, S_1]}{\sqrt{\mathrm{Var}[H_2]\mathrm{Var}[\mathrm{S}_1]}} = \frac{\mathrm{Cov}[H, S_1]}{\sqrt{\mathrm{Var}[H_2]\mathrm{Var}[\mathrm{S}_1]}} \tag{3}$$

We multiply the LHS and RHS in equations (2) and (3) to get

$$\rho_{H_1,S_1}\rho_{H_2,S_1} = \frac{\mathrm{Cov}[H, S_1]^2}{\mathrm{Var}[S_1]\sqrt{\mathrm{Var}[H_1]\mathrm{Var}[H_2]}} \tag{4}$$

By combining equations (1) and (4) and re-arranging, we have

$$\rho_{H,S_1} = \sqrt{\frac{\rho_{H_1,S_1}\rho_{H_2,S_1}}{\rho_{H_1,H_2}}} \tag{5}$$

The observed correlations in the respective experiments are $\rho_{H_1,H_2} = 0.91$, $\rho_{H_1,S_1} = 0.76$ and $\rho_{H_2,S_1} = 0.76$. We put in these values in equation (5) to get

$$\rho_{H,S_1} = 0.80$$

To estimate the reduction in correlation due to experimental error in H3K4me3, we calculate

$$\frac{\rho_{H,S_1}}{\rho_{H_1,S_1}} = \sqrt{\frac{\mathrm{Var}[H_1]}{\mathrm{Var}[H]}} = \sqrt{\frac{\mathrm{Var}[H+\epsilon_1]}{\mathrm{Var}[H]}} = \sqrt{1+\frac{\sigma_1^2}{\mathrm{Var}[H]}} = 1.05 \tag{6}$$

We re-arrange equation (6) to get

$$\frac{\sigma_1^2}{\mathrm{Var}[H]} = \left(\frac{\rho_{H,S_1}}{\rho_{H_1,S_1}}\right)^2 - 1 = 0.11$$

which is the ratio of the experimental noise with the underlying biological variance of H3K4me3.

While we have corrected for experimental error in H3K4me3, there is still experimental error in SPO11. While there is no replicate experiment available for the SPO11 data in the B6 wild-type mouse, we can approximate the uncertainty in it by using the two *Atm* proficient mice in the same publication *(29)*. These mice are fertile, have the same *Prdm9* allele, and their reported correlation in SPO11-oligo maps is 0.94, denoted $\rho_{S'_1,S'_2}$ below. Therefore, we estimate the underlying biological correlation between H3K4me3 H and SPO11-oligos S as:

$$\rho_{H,S} \approx \rho_{H,S_1}\sqrt{\frac{1}{\rho_{S'_1,S'_2}}} = 0.83.$$

2.2 Measurement of DMC1 associated with single-stranded DNA, comparison with SPO11, and homologue-engagement time

Each DSB in a cell is associated with a pair of SPO11-oligos *(29)*. These oligos are removed from the DSB-site, and are thought to be long-lived *(61)*, and the quantitative sequencing of these oligos provides a direct measure of the number of DSBs at each hotspot.

DMC1, on the other hand, has a transient association with DNA near the break-site. DMC1 decorates the single-stranded overhangs, which are generated by strand-resection near the break-site *(62)*. Once homology search is successful, and strand exchange takes place, DMC1 is no longer associated with single-stranded DNA, but with double-stranded DNA, from which it is also eventually removed. The assay for DMC1 *(37)* specifically enriches for single-stranded DNA, and is followed by a bioinformatic pipeline, which only retains sequences that show clear evidence of having being single-stranded at the time of ChIP. In summary, DMC1 ChIP-seq measures the amount of DMC1 associated with single-stranded DNA in cells, which is directly related to both the number of breaks and the length of the time taken to perform successful strand invasion.

The ratio of DMC1 and SPO11 measurements in a hotspot is therefore a measure of the average time taken, for DSBs occurring in that hotspot, to complete strand-invasion, engage with their homologous chromosome, and for DMC1 to be removed from the single-stranded DNA. Please note that this is separate from the timing of when the breaks themselves occur in the context of meiosis.

RAD51 is another protein which is associated with single-stranded DNA, and performs the role of strand invasion in mitotic cells. However, the extent of its role, if any, in strand invasion in mammalian meiotic cells is unknown. Current evidence in yeast and plants argues against a role for RAD51 in strand invasion *(63-65)*. We also note that Smagulova *et al (66)* have compared the ChIP-seq signals of RAD51 and DMC1 systematically genome-wide, and found them to be highly correlated (r=0.92 between the highest quality replicates). The correlations between RAD51 and DMC1 were similar to those between replicates of DMC1. This implies that our measure of homologue-engagement time is likely to be a good estimate even if RAD51 did play a role in strand invasion.

2.3 Overlap between crossovers and ChIP-seq peaks

ChIP-seq peaks for DMC1 overlap 92% of crossovers but occupy less than 2% of the autosomal genome. H3K4me3 peaks, including peaks at transcription-start sites (TSSs) and enhancers, cover a further 5% of the genome.

To account for the fact that hotspots are not distributed uniformly at random in the genome but tend to be present in more accessible gene-rich regions, we perform a further check. We compared with DMC1 hotspots called in the B6 wild-type mouse *(26)*, which has the *Prdm9*$^{\mathrm{B6}}$ allele, but neither of the two alleles (*Prdm9*$^{\mathrm{CAST}}$ and *Prdm9*$^{\mathrm{HUM}}$) found in the hybrid mouse. These hotspots occupied 1.4% of the genome and overlapped only 4% of crossovers, showing that the extremely high overlap of crossovers with hotspots in the hybrid mouse did not happen by chance.

2.4 Factors influencing the number of crossovers per autosome

As mentioned in the main text, the amount of H3K4me3 in recombination hotspots is a good predictor of the average number of crossovers in the autosomes (coefficient of Pearson's correlation $r = 0.8)$ in the hybrid. Correlation of H3K4me3 in hotspots in the B6 wild-type with the number of MLH1 foci (data from Froeniecke *et al (30)*) is also high $(r = 0.83)$. After accounting for an obligate crossover per chromosome pair and H3K4me3 in hotspots, there is no further effect of chromosome size on crossover rate (linear modelling with two explanatory variables). However, data from the B6 mouse indicates that the length of the synaptonemal axis in microns (also from *30*) is a better predictor of MLH1 foci ($r = 0.95$). There is no further significant effect of H3K4me3 after accounting for axis length (p=0.22, linear modelling). Axis length is also a better predictor of MLH1 foci than the number of DSBs (data from Lange *et al (29)*), and the effect of DSB number is also not significant after axis length is included in the model (p=0.98, linear modelling).

In contrast to the results for the number of crossovers, the best predictor of the total number of DSBs, amongst these factors, is the total H3K4me3. The length of the axis is not a significant predictor of DSBs after H3K4me3 is taken into account. This suggests that the length of the axis has an impact on crossover resolution downstream of breaks.

2.5 Density Plots

All density curves (Figs. 2B, 4A, S17) were plotted using the `geom_density` function in the `ggplot2` package in `R`. This function computes and draws a kernel density estimate, and we used the (default) gaussian kernel.

2.6 PRDM9-binding asymmetry, heterozygosity and modelling their effects on crossover resolution probability

For each hotspot, we estimated its PRDM9-binding symmetry, as a measure of the extent to which PRDM9 binds both homologues equally. We estimated, as discussed above, the fraction of the H3K4me3 signal that arises from the B6 and CAST chromosomes for each hotspot. If the fraction of reads arising from the B6 chromosome for hotspot i is $b_i \in [0, 1]$, we define symmetry s_i as

$$s_i = 4 \times b_i \times (1 - b_i)$$

and asymmetry a_i as

$$a_i = 1 - s_i.$$

In the event that equal numbers of reads arise from both chromosomes, i.e., $b_i = 0.5$, the hotspot is said to be totally symmetric and $s_i = 1$ and $a_i = 0$. In the event that only one of the two chromosomes is bound, i.e., $b_i = 0$ or $b_i = 1$, the hotspot is said to totally asymmetric and $s_i = 0$ and $a_i = 1$.

Here we define crossover resolution probability as the crossover rate conditional on recombination initiation as measured by H3K4me3. In order to model the effect of asymmetry on crossover resolution probability (Fig. 3A), we assigned all DMC1 hotspots into one of 5 bins in accordance with their asymmetry: [0,0.09], (0.09,0.36], (0.36,0.7], (0.7, 0.9], (0.9,1]. The average asymmetry of these bins was 0.02, 0.20, 0.54, 0.80 and 0.95 respectively, and the number of hotspots was 10158, 3338, 3102, 1754, and 447 respectively. We used a generalised linear modelling (GLM) approach to model crossover counts, namely a quasi-Poisson model. The quasi-Poisson model accommodates over-dispersion in the data by estimating an additional dispersion parameter from it. We employed the default log-link function for the GLM:

$$\log(\mathbb{E}[C|H,P,A]) = \alpha + \gamma\log(H) + \eta P + \sum_{i=1}^{5}\beta_i \mathbb{1}_{\{A=i\}}$$

where C is the number of crossovers observed in a hotspot, H and P are the H3K4me3 intensity and the PRDM9 variant controlling that hotspot, respectively. A is a categorical variable encoding the 5 asymmetry bins (defined above), and $\mathbb{1}_{\{A=i\}}$ is simply the indicator function of whether the hotspot occurs in bin i or not. The hotspots were filtered to exclude hotspots on the X chromosome (which do not have crossovers in the non-PAR region), or those without an allelic assignment. Hotspots that had evidence of overlap with PRDM9-independent H3K4me3 were also excluded, as discussed above.

The GLM was fitted using the `glm` function in R, with the family `quasipoisson`. The relative crossover likelihoods $\exp(\hat{\beta}_i)/\exp(\hat{\beta}_1)$ and standard errors, thus obtained for each bin are plotted in Fig. 3A. We normalised using the first bin, without loss of generality (wlog).

In order to model the effect of heterozygosity on crossover resolution probability, we took a similar approach. We assigned all DMC1 hotspots into one of 4 bins, depending on the number of SNP differences between the B6 and CAST chromosomes ± 100 bases from the hotspot centre, as determined by the centre of the PRDM9 motif. The four bins have 0, $[1, 2]$, $[3, 4]$, $[5, \infty)$ SNP differences respectively. As above, we performed the same filtering of hotspots, and take a GLM approach. In the first instance, we modelled the effect of heterozygosity without taking asymmetry into account:

$$\log(\mathbb{E}[C|H, P, d]) = \alpha + \gamma \log(H) + \eta P + \sum_{i=1}^{4} \beta_i \mathbb{1}_{\{d=i\}}$$

where, as above, C is the number of crossovers observed in a hotspot, H and P are the H3K4me3 intensity and the PRDM9 allele inferred for that hotspot, respectively. d is a categorical variable encoding the 4 heterozygosity bins (defined above), and $\mathbb{1}_{\{d=i\}}$ is simply the indicator function of whether the hotspot occurs in bin i or not. The GLM was fitted using the `glm` function in R, with the family `quasipoisson`. We normalised using the first bin, with 0 SNPs, wlog. The relative crossover likelihoods $\exp(\hat{\beta}_i)/\exp(\hat{\beta}_1)$ and standard errors, thus obtained for each bin are plotted in Fig. 3B in blue.

Next, we modelled the effect of heterozygosity while taking asymmetry into account:

$$\log(\mathbb{E}[C|H, P, d, a]) = \alpha + \gamma \log(H) + \eta P + \mu a_i + \sum_{i=1}^{4} \beta_i \mathbb{1}_{\{d=i\}}$$

where a_i is the PRDM9 binding asymmetry as defined above. The other variables are unchanged. We plot the relative crossover likelihoods $\exp(\hat{\beta}_i)/\exp(\hat{\beta}_1)$ and standard errors obtained here in red in Fig. 3B.

We also performed a version of these analyses without binning of hotspots, to facilitate comparison with Smagulova *et al (32)*. First, we fit the model for heterozygosity, without conditioning on asymmetry, for the same hotspots as above:

$$\log(\mathbb{E}[C|H, P, d]) = \alpha + \gamma \log(H) + \eta P + \beta m$$

where, as above, C is the number of crossovers observed in a hotspot, H and P are the H3K4me3 intensity and the PRDM9 allele inferred for that hotspot, respectively. The number of single-nucleotide polymorphisms around the hotspot centre, which is defined as the centre of the PRDM9 motif within it, is denoted by m. The p-value reported in the main manuscript (0.06) is based on counting SNPs within a window ± 100 bp from the motif centre. Please see p-values from tests with additional window sizes in Table S1.

Similarly, we fit for asymmetry:

$$\log(\mathbb{E}[C|H,P,d]) = \alpha + \gamma \log(H) + \eta P + \tau a.$$

The p-values are reported in Table S1. Finally, we fit for heterozygosity and asymmetry jointly:

$$\log(\mathbb{E}[C|H,P,d]) = \alpha + \gamma \log(H) + \eta P + \beta m + \tau a.$$

Their individual p-values are reported in Table S1 under the columns “heterozygosity conditional on asymmetry” and “asymmetry conditional on heterozygosity”.

In Figs. 3C, 4B, S16, S20, S21, and S42, the following definition of crossover resolution probability is used, with the same intent of estimating the probability of crossover resolution per DSB or per unit recombination initiation. For a given set of hotspots $\mathbb{H}$, the crossover resolution probability $p = \frac{\sum_{j \in \mathbb{H}} C_j}{\sum_{j \in \mathbb{H}} H_j}$,where C_j is the number of crossovers overlapping hotspot $j \in \mathbb{H}$, and H_j is H3K4me3 intensity for hotspot j.

2.7 Inference of the homologue on which the DSB initiating the crossover occurred

While crossovers are mainly reciprocal exchanges of DNA between homologous chromosomes, they are accompanied by short gene-conversion tracts where a segment of DNA from the *DSB-initiating* chromosome is lost and copied from the uncut template homologue *(31)*. If we could identify the precise gene-conversion tract for each crossover, we could identify which of the two homologues it matched and thus infer which homologue had the initiating DSB. However, identifying both endpoints of gene conversion tracts requires knowledge of all four products of a single meiosis *(31)*, and that information is lost by the time we harvest sperm.

Therefore, we take an alternative approach. Lange et al *(29)* showed that DSBs are concentrated in the nucleosome-depleted region (NDR) around the PRDM9 binding motif, with additional, much weaker, secondary peaks centered approximately 277 bases from the motif centre, and extending till about 300-320 bases from the motif centre. We take a conservative approach and restrict to hotspots with a unique high-quality match for the appropriate PRDM9 motif. Next, we look for crossovers that have evidence of only one haplotype within the central region around the motif, including the secondary DSB peaks (± 350 bp). We assigned a crossover to have initiated on the B6 haplotype if and only if:

1. The haplotype call for the first SNP to the left of the site -350 bp from the motif centre, and the first SNP to the right of the site +350 bp from the motif centre both match the CAST haplotype AND further SNP calls, if any, within the central 700 bp region all also match the CAST haplotype, OR
2. All SNP calls made in the central 700 bp region matched the CAST haplotype, with a minimum of 3 unambiguous SNP calls.

Conversely, a crossover was inferred to have initiated on the CAST haplotype, if the SNP calls above matched the B6 reference.

We were able to infer the initiating chromosome for 685 crossovers (n) using this procedure. Amongst extremely asymmetric hotspots where the more bound homologue had, on average, more than 95% of the H3K4m3, only 47 out of 60, i.e., 78% (f) of the crossovers initiated on it. To check that our findings are robust to the choice of parameters used for inferring the initiating homologue of the crossover, we repeat the procedure above for several additional parameters. The total number of crossovers, n, for which the inference could be made, and the fraction of crossovers initiating from the more-bound homologue, f, in extremely asymmetric hotspots, are reported below (from most conservative to least conservative parameters):

- Central region of 1000 bp, and at least 5 SNP calls: $n = 513, f = 77\%$;
- Central region of 700 bp, and at least 5 SNP calls: $n = 614, f = 80\%$;
- Central region of 700 bp, and at least 3 SNP calls: $n = 685, f = 78\%$;
- Central region of 400 bp, and at least 2 SNP calls: $n = 869, f = 78\%$;
- Central region of 200 bp, at least 1 SNP call: $n = 1004, f = 79\%$.

The results in Fig. 3C and Fig. S16 are also robust to these biologically reasonable parameter choices. We conclude that the inference is not sensitive to parameter choice.

To get confidence intervals and p-values, we performed 10,000 bootstrap-resampling iterations over the set of hotspots and re-estimated the quantities of interest (the number of crossovers originating on each homologue, and the H3K4me3 on each homologue).

2.8 More active hotspots have a disproportionately large number of crossovers

As noted in the main manuscript, the effect of PRDM9 binding on the template may explain why there are more crossovers than expected in more active hotspots, as PRDM9 binding on the template is more likely at more active hotspots (4-fold difference between the extreme bins, as shown in Fig. 3F). It is also possible that more active hotspots are disproportionately more likely to have DSBs. Direct measurements of DSBs in B6 mice show this effect, although it is smaller (2-fold difference between the extreme bins, with same number of bins, n=7). A combination of both factors may explain the observed effect.

2.9 Constructing matched hotspot sets with and without crossovers

To identify further effects on crossover resolution after accounting for known factors, we created two matched sets of hotspots, the first of which had a crossover while the other did not.

To estimate the effect of PRDM9 variant, we performed the following steps for each hotspot that had a crossover. Only hotspots where the activating PRDM9 variant could be identified, and which did not show evidence of PRDM9-independent H3K4me3 were included. Let the hotspot with crossover, H, be on autosome $c \in \{1, 2, \ldots, 19\}$, with total H3K4me3 enrichment h and the fraction of its H3K4me3 on the B6 chromosome $b \in [0, 1]$. Let the matched sets with and without crossovers be $\mathbb{H}$ and $\mathbb{N}$, respectively.

1. We identified the set of hotspots which did not have a crossover, which occurred on the same autosome c, and whose B6 H3K4me3 fraction $b_i \in [b - 0.04, b + 0.04]$.

2. If this set was empty, no match was found and the hotspot H was not included in $\mathbb{H}$.

3. If the set was non-empty, the hotspot N_i with the closest H3K4me3 enrichment was identified, i.e., $\texttt{argmin}_i \texttt{abs}(h_i - h)$.

4. If the hotspot N_i had H3K4me3 enrichment within 5% of the hotspot H, i.e. if $\texttt{abs}(h_i - h)/h \leq 0.05$, H was included in the set $\mathbb{H}$ and N_i was included in $\mathbb{N}$. H

and N_i were added with the multiplicity of the number of crossovers in H. If the difference was greater than 5%, then neither hotspot was added to either set.

The sets $\mathbb{H}$ and $\mathbb{N}$ were then compared for the number of hotspots that were activated by each PRDM9 variant (Table S1). The findings were robust to the choices of parameters used in the matching procedure above. For example, in the procedure above, the asymmetry tolerance is 0.04 and the enrichment tolerance is 0.05, which we denote as $tol = (0.04, 0.05)$, and the number of matched pairs was 1592. For more stringent settings, e.g., $tol = (0.02, 0.02)$, we get odds ratio (OR)= $1.28, 95\%\ CI = [1.04, 1.56], n = 881$, or for $tol = (0.03, 0.04), OR = 1.33, 95\%\ CI = [1.14, 1.56], n = 1429$. For less stringent settings, e.g., $tol = (0.05, 0.10)$, we get $OR = 1.26, 95\%\ CI = [1.09, 1.45], n = 1788$, or for $tol = (0.07, 0.10)$, we get $OR = 1.30, 95\%\ CI = [1.13, 1.49], n = 1833$.

To check for the effect of GC-content after accounting PRDM9 variant, a further constraint was added in step 1 above, requiring the hotspots without crossover to have the same PRDM9 variant as the hotspot with crossover under consideration. The number of matched pairs was 1355. The local GC-content was calculated as the fraction of non-N/n bases that are G/g/C/c in the ± 500 bp from the hotspot centre. These matched hotspots were used to plot Fig. 4A.

In order to check whether the GC-content effect is distinct from the allele effect, we estimated the effect sizes of both factors. Each hotspot, whether or not it has a crossover, was matched with another hotspot, again whether or not it has a crossover, but which is on the same autosome, activated by the same PRDM9 variant and very similar H3K4me3 on both homologues (same parameters as above). However, instead of picking a single closest match as in step 3, we randomly picked a hotspot from amongst these close matches. For each such pair of hotspots, the hotspot with higher local GC-content was placed in a high-GC bin, and the other hotspot was placed in a low-GC bin. This sampling was performed 100 times for each hotspot. We then compared the number of crossovers in the high-GC bin with the number in the low GC-bin (Fig. S24). The mean difference between the high- and low-GC bins was 5.7% for GC-content and 33% for the number of crossovers.

The local GC-content is higher in hotspots activated by PRDM9$^{\mathrm{HUM}}$ (mean local GC-content in PRDM9$^{\mathrm{HUM}}$ hotspots=44.7%, for PRDM9$^{\mathrm{CAST}}$ hotspots=43.3%, difference= 1.4%). We estimated what the expected effect size on crossover would be for this magnitude of GC-difference. We repeated the procedure above with the difference that hotspots assigned to the high-GC and low-GC bins were randomly swapped with probability 24% in order to reduce the difference in GC-content between the high- and low-GC bins. We then compared the number of crossovers in the high-GC bin with the number in the low GC-bin (Fig. S24). The mean difference between the high- and low-GC bins was 1.4% for GC-content, as intended, and 8% for the number of crossovers. We conclude that the allele effect (32%, see main text) is greater than the effect expected from GC-content between the hotspots of the two alleles (8%) and is therefore unlikely to simply be a consequence of GC differences.

2.10 Modelling the effect of PRDM9 variant on homologue engagement time

We took a similar approach to modelling homologue engagement time as we did for crossover resolution probability in Section 2.6. We used a GLM with a quasi-poisson model for modelling DMC1 conditional on H3K4me3. We employed the default log-link function for the GLM:

$$\log(\mathbb{E}[D|H,P,a]) = \alpha + \gamma\log(H) + \eta_{CAST}\mathbb{1}_{\{P=CAST\}} + \eta_{HUM}\mathbb{1}_{\{P=HUM\}} + \beta a + \tau d$$

where D is the DMC1 intensity in a hotspot, and H and a are the H3K4me3 intensity and asymmetry (defined in Section 2.6) respectively. d is the distance of the hotspot from the centromere-distal telomere on that chromosome. P is a categorical variable encoding the PRDM9 variant, and $\mathbb{1}_{\{P=CAST\}}$ is the indicator function of whether the hotspot is activated by PRDM9$^{\text{CAST}}$, and $\mathbb{1}_{\{P=HUM\}}$ is similarly the indicator for PRDM9$^{\text{HUM}}$. As before, hotspots were filtered to exclude hotspots on the X chromosome and those without an allelic assignment. Hotspots that had evidence of overlap with PRDM9-independent H3K4me3 were also excluded, as before. $\tilde{\eta}_{CAST}$ and $\tilde{\eta}_{HUM}$ are normalised so that $\tilde{\eta}_{CAST} = 1$, wlog. The left pair of bars in Fig. S32 show the normalised $\tilde{\eta}_{CAST}$ and $\tilde{\eta}_{HUM}$, together with their standard errors. The association with distance from the telomere is also significant ($p = 10^{-37}$).

To model the effect of the PRDM9 variant while accounting for differences in local GC-content, we add an additional variable ϕ. The local GC-content ϕ is defined as the fraction of non-N/n bases that are G/g/C/c in the $\pm$ 500 bp from the hotspot centre. We fit the GLM:

$$\log(\mathbb{E}[D|H,P,a]) = \alpha + \gamma\log(H) + \eta_{CAST}\mathbb{1}_{\{P=CAST\}} + \eta_{HUM}\mathbb{1}_{\{P=HUM\}} + \beta a + \tau d + \theta\phi$$

where the other variables are unchanged.

The right pair of bars in Fig. S32 show the normalised $\tilde{\eta}_{CAST}$ and $\tilde{\eta}_{HUM}$, together with their standard errors. The association of local GC-content is also significant ($p = 2 \times 10^{-15}$), and the distance from the telomere continues to be significant after including GC-content in the model ($p = 10^{-31}$).

2.11 Relative effect sizes of factors influencing crossover resolution and homologue engagement

On crossover resolution, PRDM9-binding on the homologue has the biggest effect size ($\geq$6-fold, Figs. 3C. S16), followed by the impact of proximity to the distal telomere ($\sim$5-fold, Fig. 4B), GC-content ($\sim$33% between the highest and lowest GC hotspots, Fig. S24), and PRDM9 variant ($\sim$30% (24%-32%) difference between the two alleles, Table S1, Fig. S24). Consistent with our hypothesis, the impact of these factors on homologue engagement time follows the same order: PRDM9 binding on the homolog ($\sim$4-fold, Fig. 5D), proximity to the distal telomere ($\sim$24%, Fig. 5B), GC-content ($\sim$23%, Fig. 5C) and PRDM9 variant ($\sim$18%, Fig. S32). The relatively large effect size of telomere proximity on crossover resolution is consistent with the presence of additional factors influencing the spatial localisation of crossovers *(11, 12)*.

2.12 Distribution of crossover breakpoints and nucleosome positioning

Crossover breakpoints are known within a region of uncertainty, with each end point being the location of a SNP that is informative about the haplotype (whether B6 or CAST), as illustrated in Fig. 1C. To construct the distribution of breakpoints across crossovers, we position each crossover relative to the centre of the motif in the hotspot with which it overlaps. Only crossovers overlapping hotspots with a unique, high quality motif match were included, to minimise ambiguity. We assumed, for each crossover, that the true breakpoint is equally likely to occur anywhere in the region of uncertainty. For example, if the region is 10 bp long, a weight of 0.1 is added to each base interval within the region, while if it is 100 bp long, a weight of 0.01 is added to each base pair interval. Regions upstream of the motif were treated in the same way as regions downstream of the motif, i.e., the signal from each side was added to obtain the final distribution.

To identify the nucleosome positions around PRDM9^{CAST}-bound sites, we performed MNase ChIP-seq for H3K4me3 in the hybrid (Section 1.10). This approach cannot be used to identify nucleosomes when PRDM9 is not bound, as MNase ChIP-seq preferentially picks up sites that have nucleosomes with the H3K4me3 mark nearby. We reasoned that the chromatin environment in the unbound state would be better represented by Mnase-seq alone (without H3K4me3 ChIP) in the hybrid as it does not preferentially pick up sites with H3K4me3 (Section 1.10). While this is a better estimate of the chromatin environment in the unbound state, it nevertheless represents a mix of cells, including many in whom the hotspot site will be bound by PRDM9. Therefore, to further reduce the impact of sites that have PRDM9 bound, we show in Fig. 6B the average MNase-seq profile on the *less-bound chromosome* in asymmetric PRDM9^{CAST} hotspots. As for the other ChIP-seq measures above, we infer this by matching reads to known single-nucleotide polymorphisms in B6 and CAST. The MNase-seq profile was corrected for differences in the power to map reads to haplotypes due to differential SNP density around the hotspot centre.

An alternative approach to identify nucleosome positions at PRDM9^{CAST} sites when PRDM9 is not bound is to look at MNase-seq in PRDM9^{CAST} hotspot sites, but in a different mouse, which does not have the *Prdm9*^{CAST} allele. Such as experiment was performed in the wild-type B6 mouse by Baker *et al (39)*, and our findings were confirmed using their data in Fig. S34.

As for PRDM9^{CAST}, we used MNase ChIP-seq for H3K4me3 to infer nucleosome positions around PRDM9^{HUM}-bound sites (Fig. S35), and show it alongside crossover breakpoints for symmetric PRDM9^{HUM} hotspots. There were not enough crossovers to perform this analysis for asymmetric PRDM9$^{\text{HUM}}$ hotspots.

2.13 Analyses with het-PAR hotspots

In total, 40 DMC1 hotspots were called in the het-PAR, and we were able to infer the relative proportions of DMC1 on the B6 and CAST chromosomes in 38 of them. If d_i is the DMC1 measure of hotspot i, and the fraction of the signal on the B6 haplotype is b_i, then the DMC1 signal on the B6 chromosome for hotspot i is $d_i b_i$ and of the CAST haplotype is $d_i(1-b_i)$. We calculated the weighted average fraction across these hotspots on the CAST haplotype as $\sum_i d_i(1-b_i)/\sum_i d_i$. This value was 0.87, implying the fraction on the B6 haplotype is 0.13. The ratio of these quantities represents the fold-difference in DMC1 in het-PAR hotspots between the haplotypes, and is 6.7.

We calculated p-values for the above, as well as for the fractions of DMC1 and crossovers in PRDM9-independent hotspots, using bootstrap re-sampling with 10,000 iterations.

3 Supplementary Figures and Tables

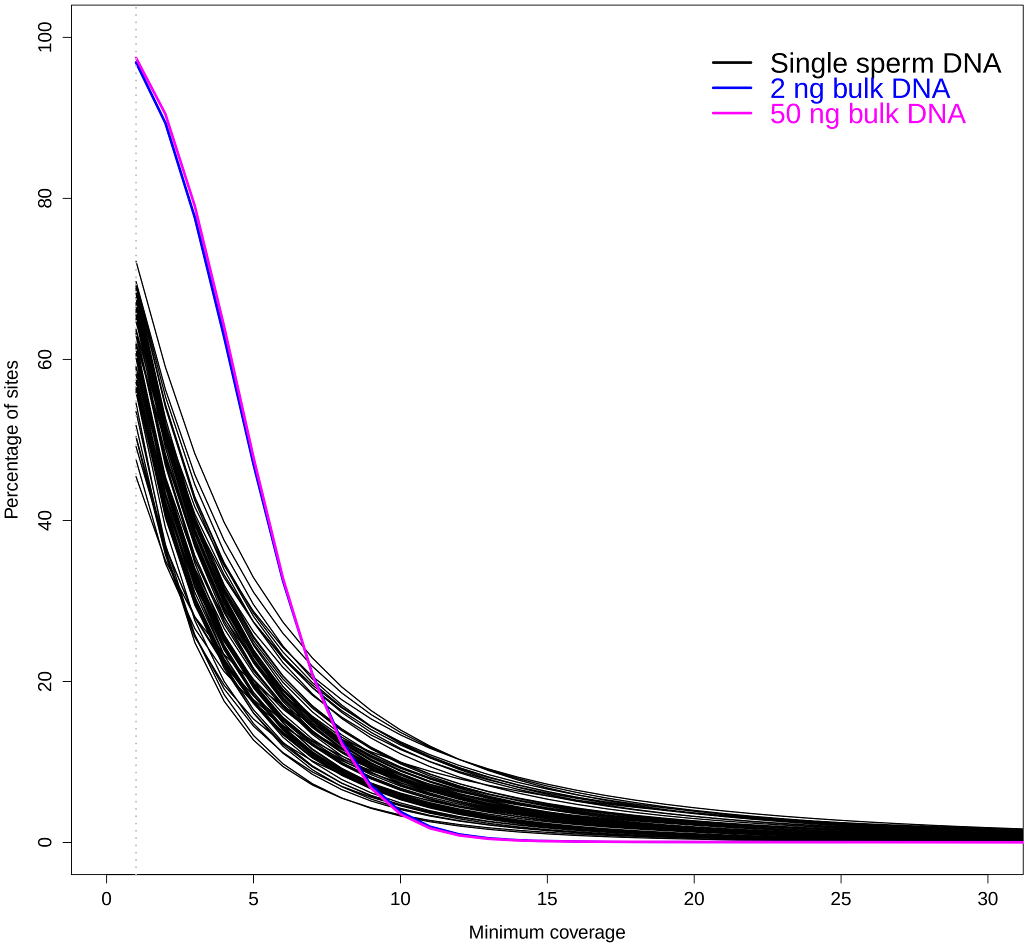

Figure S1: This figure shows the percentage of the genome covered at different depths for each of 217 sperm cells and with bulk DNA with different amounts of starting material. The bulk DNA samples were originally sequenced at higher depth (19.5X for the 2ng sample and 9.4X for the 50ng sample). For this figure, they were sampled down to match the median depth of coverage for the sperm samples.

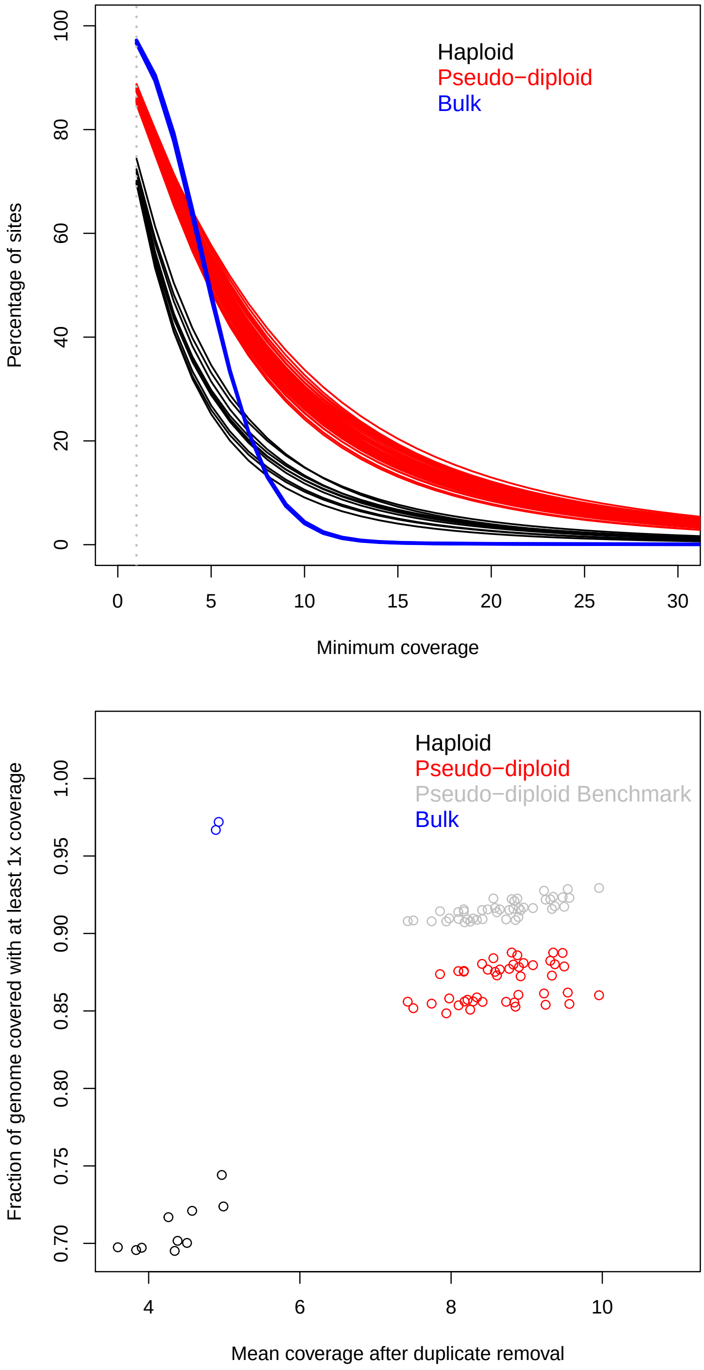

Figure S2: Illustration that genomic regions lost during single-sperm sequencing are lost almost at random, rather than clustered. (Top) 10 sperm samples with genome coverage around 70% (between 69.5% and 75%, shown in black), were paired-up to make 45 “pseudo-diploid” samples. The coverage of the pseudo-diploids is shown in red. (Bottom) If regions of the genome were lost entirely systematically, no increase in the fraction of genome covered would be observed in pseudo-diploids. If the regions were lost entirely uniformly at random, which is the best possible scenario, the median coverage would be as shown in gray. The actual coverage (red) is close to the best possible outcome (gray).

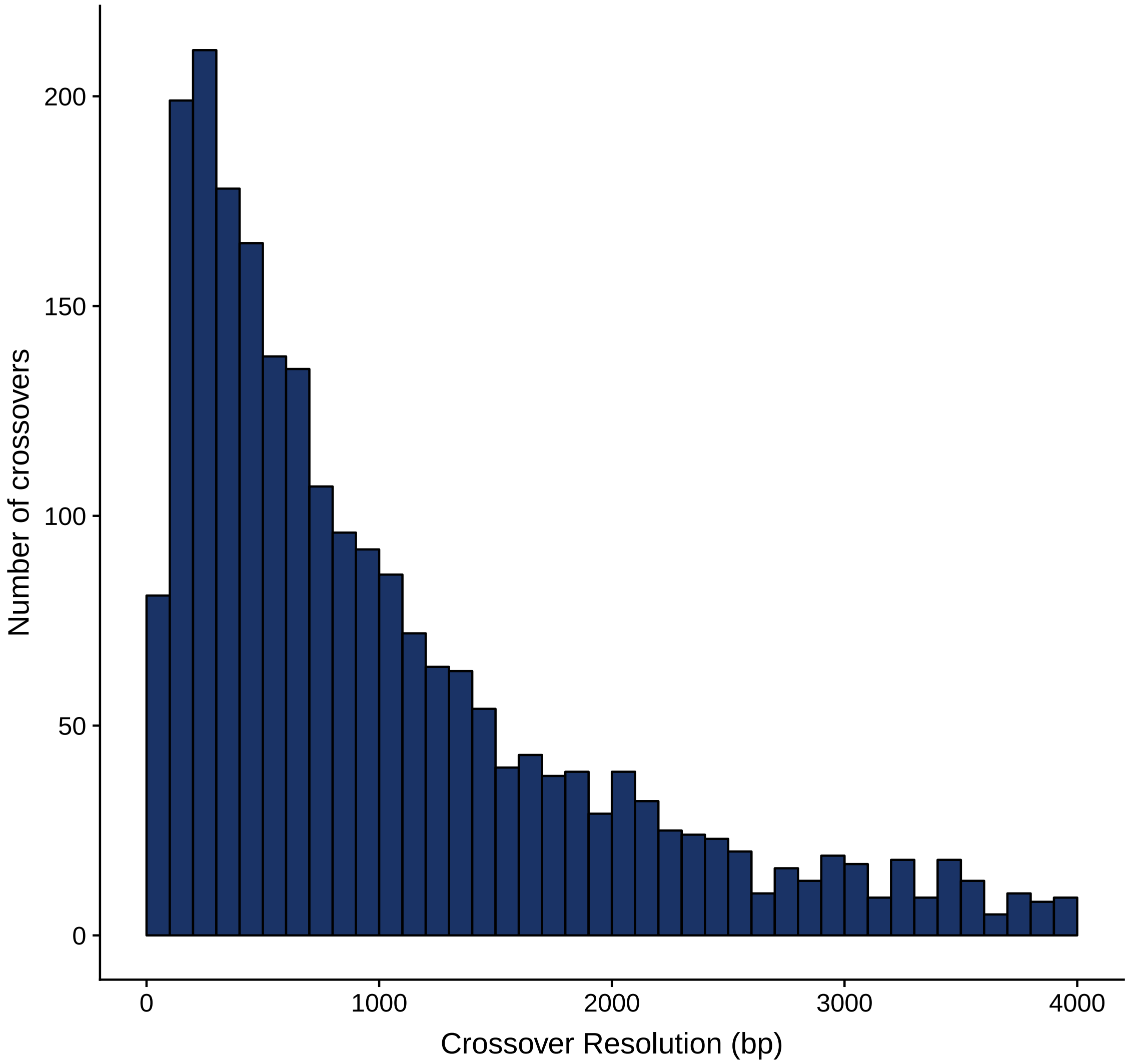

Figure S3: Distribution of the resolution of crossover breakpoints. The median resolution is 916 bp, with 386 crossovers resolved within 250bp.

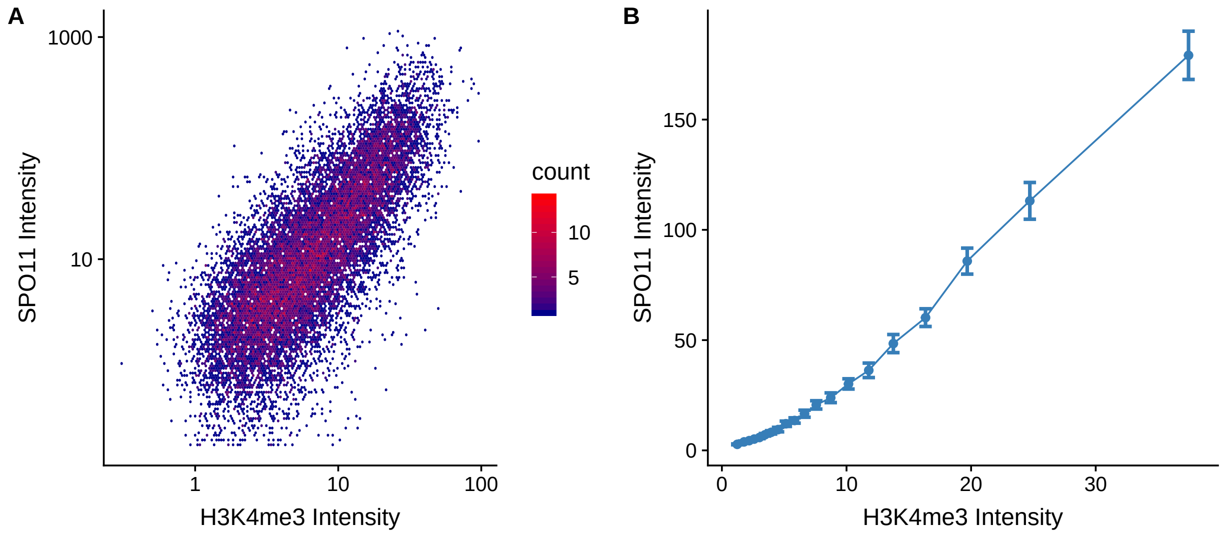

Figure S4: (**A**) Comparison of SPO11-oligos *(29)* and H3K4me3 intensities *(25)* in autosomal DMC1 hotspots in the wild-type B6 mouse (Pearson's $r = 0.77$, $n = 15,512$). The underlying 'biological' correlation after correcting for experimental error in H3K4me3 and SPO11-oligos is $r = 0.83$ *(25)*. SPO11 intensity is calculated as the number of SPO11-oligo reads overlapping ± 500 bp of the DMC1 hotspot centre, and re-scaled as per *(29)*. Hotspots that showed evidence of PRDM9-independent H3K4me3, for example, due to overlap with transcription start sites, were excluded *(25,26)*. Hotspots with an extremely low number of SPO11-oligo reads (fewer than 10 SPO11-oligo reads, corresponding to 0.2 RPM) were also excluded due to likely noise *(29)*.

(**B**) Comparison of SPO11 and H3K4me3 intensities on a linear scale suggests an approximately linear relationship between them (hotspots divided into 20 bins, 1 standard error bars shown)

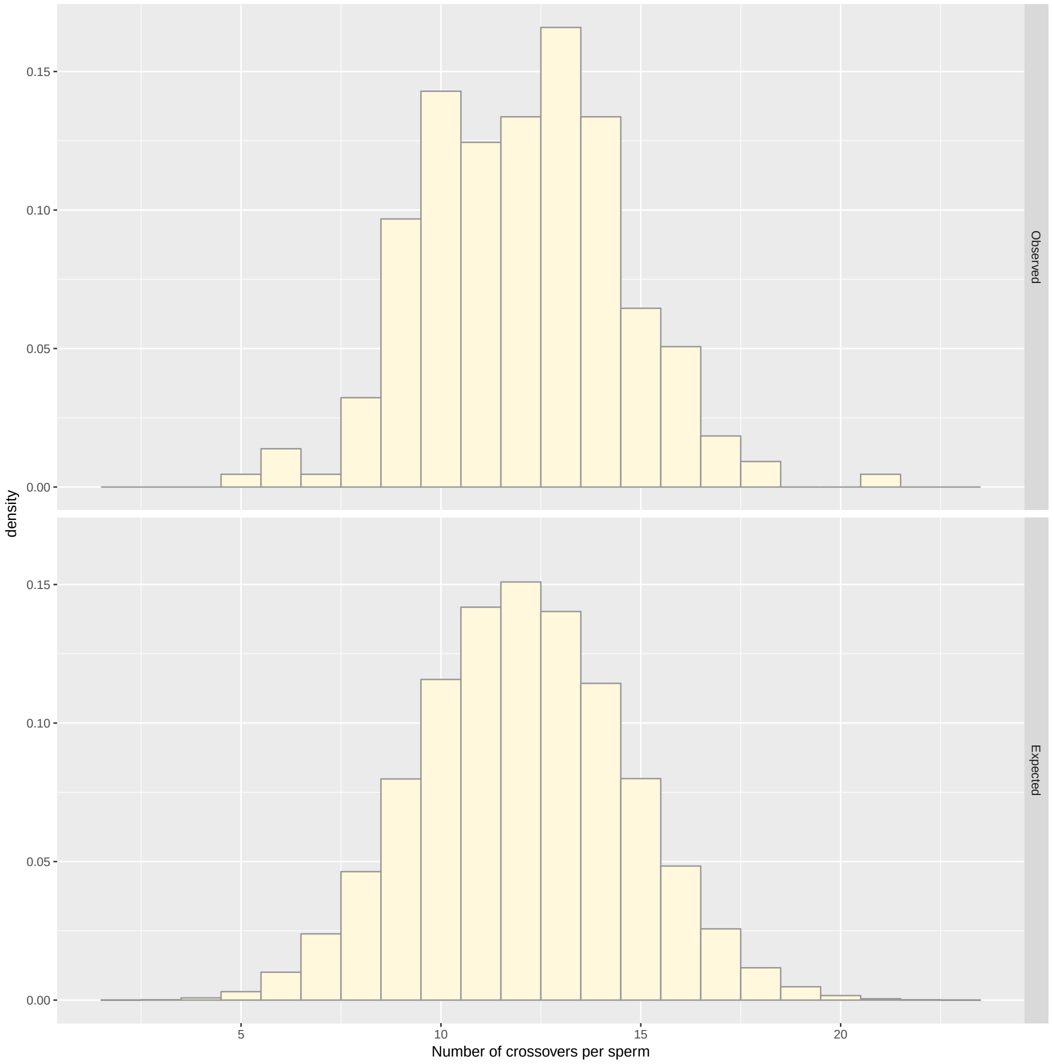

Figure S5: (Top) Distribution of the number of crossovers identified per sperm. (Bottom) Distribution of the number of crossovers expected per sperm if the chromatids segregate randomly. There is no evidence that some sperm have systematically greater number of crossovers than others, as assessed by the variance in numbers of crossovers (p=0.38, F-test). The two distributions are not significantly different (p=0.995, Kolmogorov-Smirnov test).

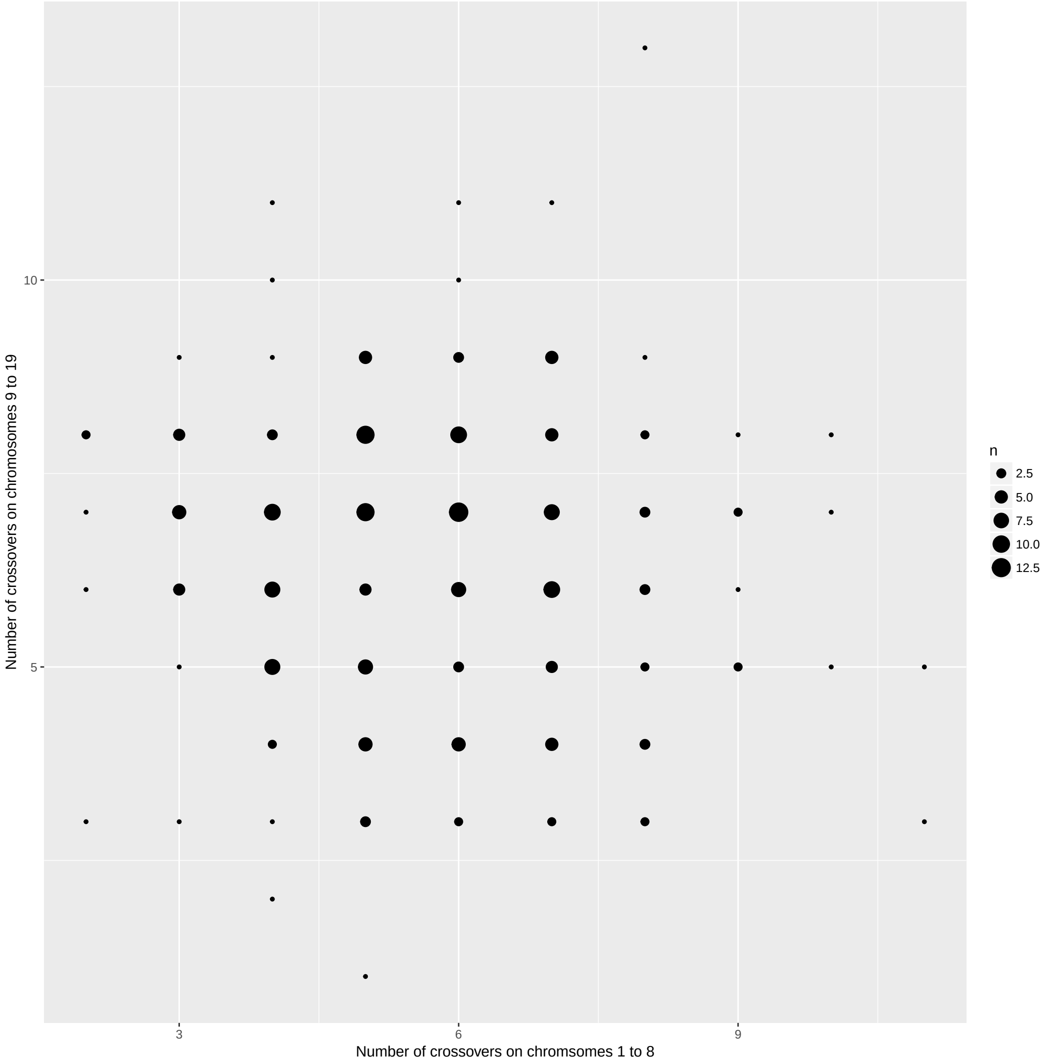

Figure S6: To test if some sperm have systematically greater or smaller numbers of crossovers than others, we calculate the number of crossovers per sperm in two groups of chromosomes: chromosome 1-8 and chromosomes 9-19. There is no evidence that some sperm have systematically greater number of crossovers than others, as assessed by the (lack of) correlation between these counts (Pearson's correlation coefficient = -0.04, p-value=0.53)

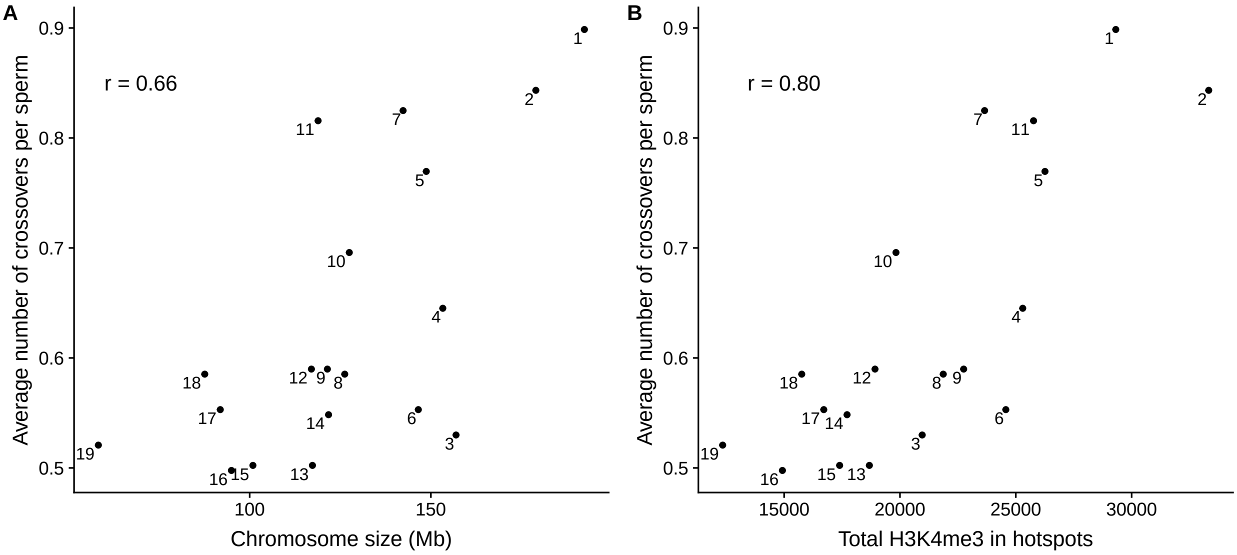

Figure S7: Total H3K4me3 in hotspots is a good predictor of the total number of crossovers, relative to chromosome size in base pairs. (**A**) Comparison of chromosome size in megabases and the average number of crossovers per chromosome per sperm in the hybrid. (**B**) Comparison of the total H3K4me3 in recombination hotspots per chromosome and the average number of crossovers per chromosome per sperm in the hybrid.

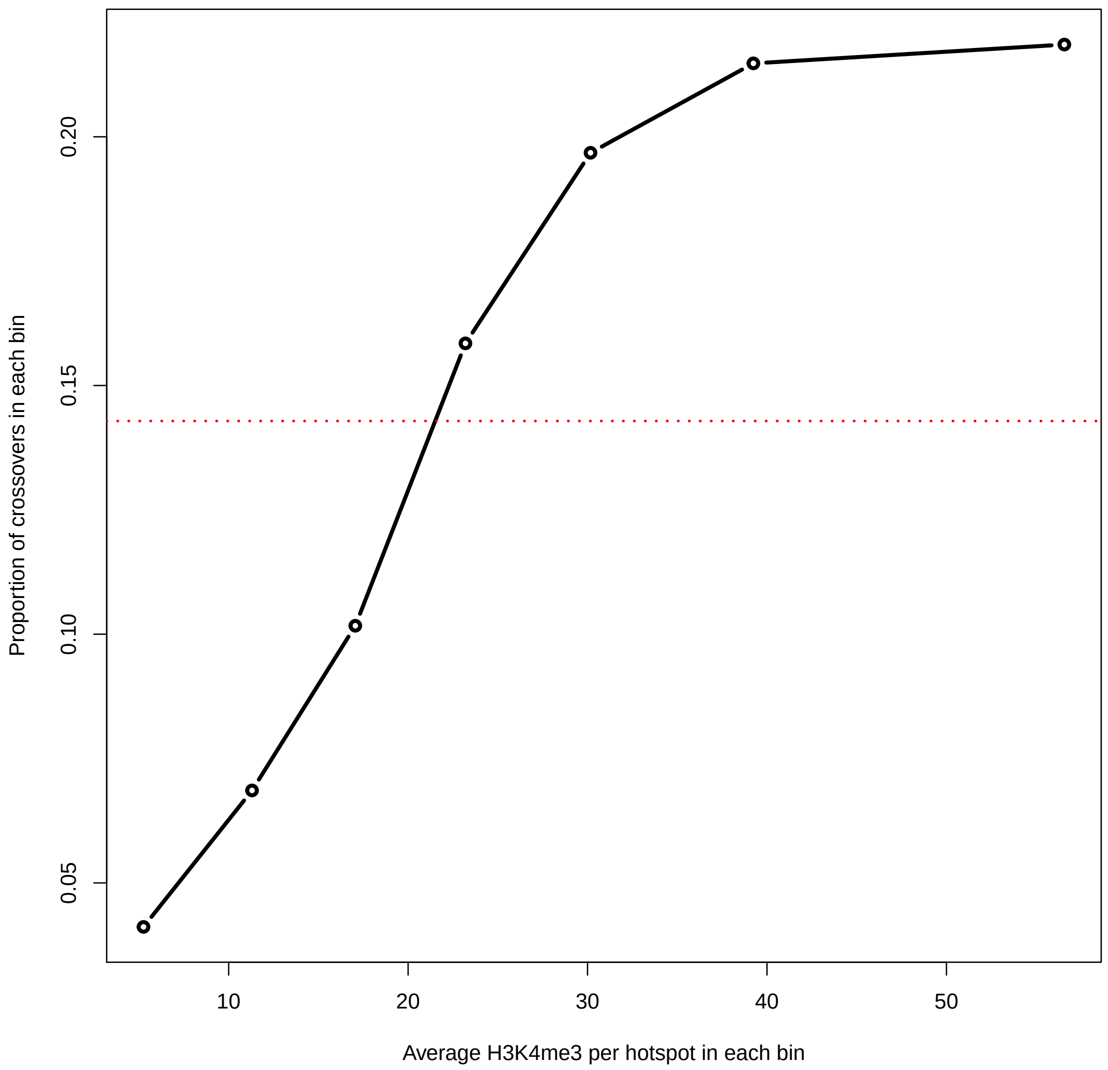

Figure S8: More active hotspots have a disproportionately greater number of crossovers. Hotspots were binned into 7 bins, so that the total H3K4me3 intensity in each bin was the same. The observed proportion of crossovers in the hotspots in each bin is shown (black, y-axis), relative to the average H3K4me3 intensity of hotspots in the bin (x-axis). The proportion of crossovers expected from the H3K4me3 in each bin is the same (red).

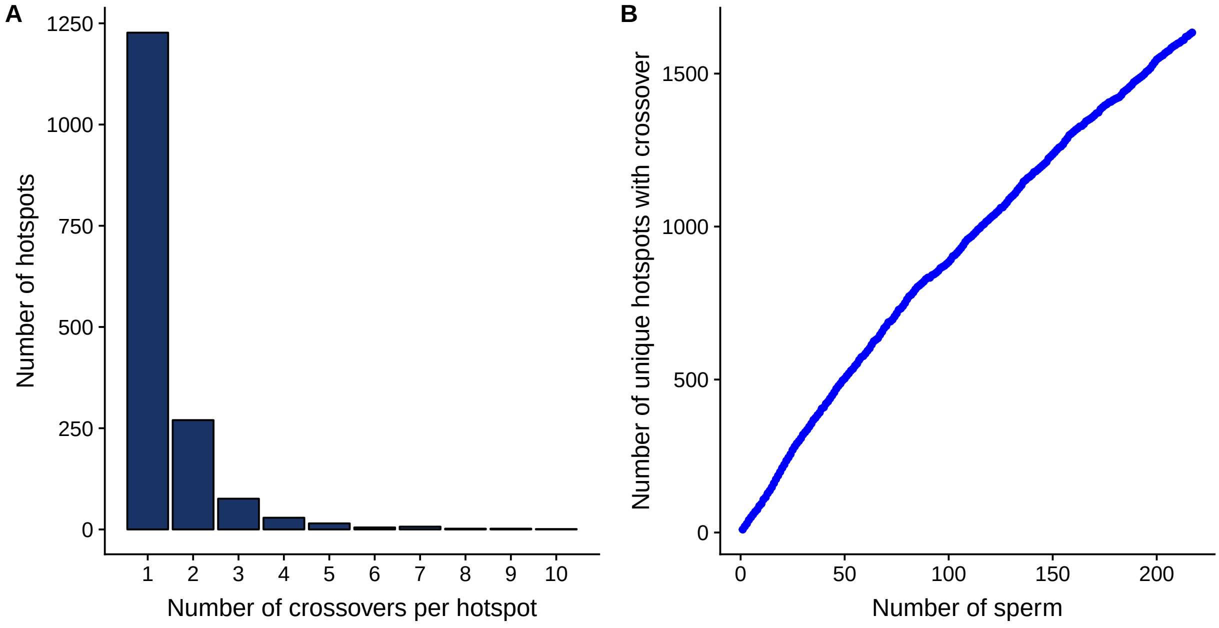

Figure S9: (**A**) The distribution of the number of autosomal crossovers per hotspot. (**B**) As the number of sperm samples is increased, the number of hotspots with at least one crossover increases almost linearly.

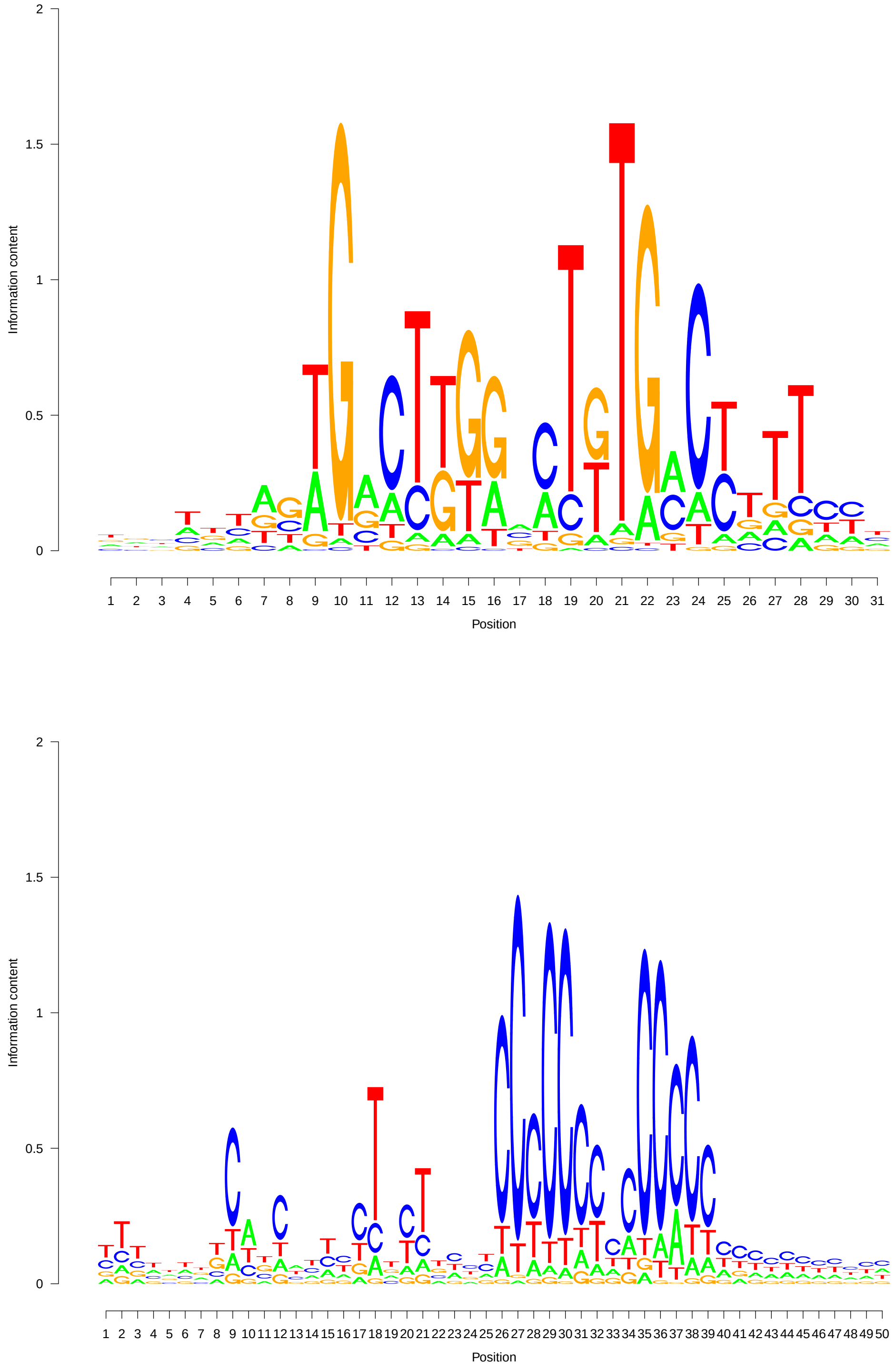

Figure S10: Logo plots for PRDM9-binding motifs identified in PRDM9$^{\mathrm{CAST}}$ (top) and PRDM9$^{\mathrm{HUM}}$ (bottom) hotspots. Stack height depicts the information content at each position, and the relative height of letters is proportional to their frequency in the sequences.

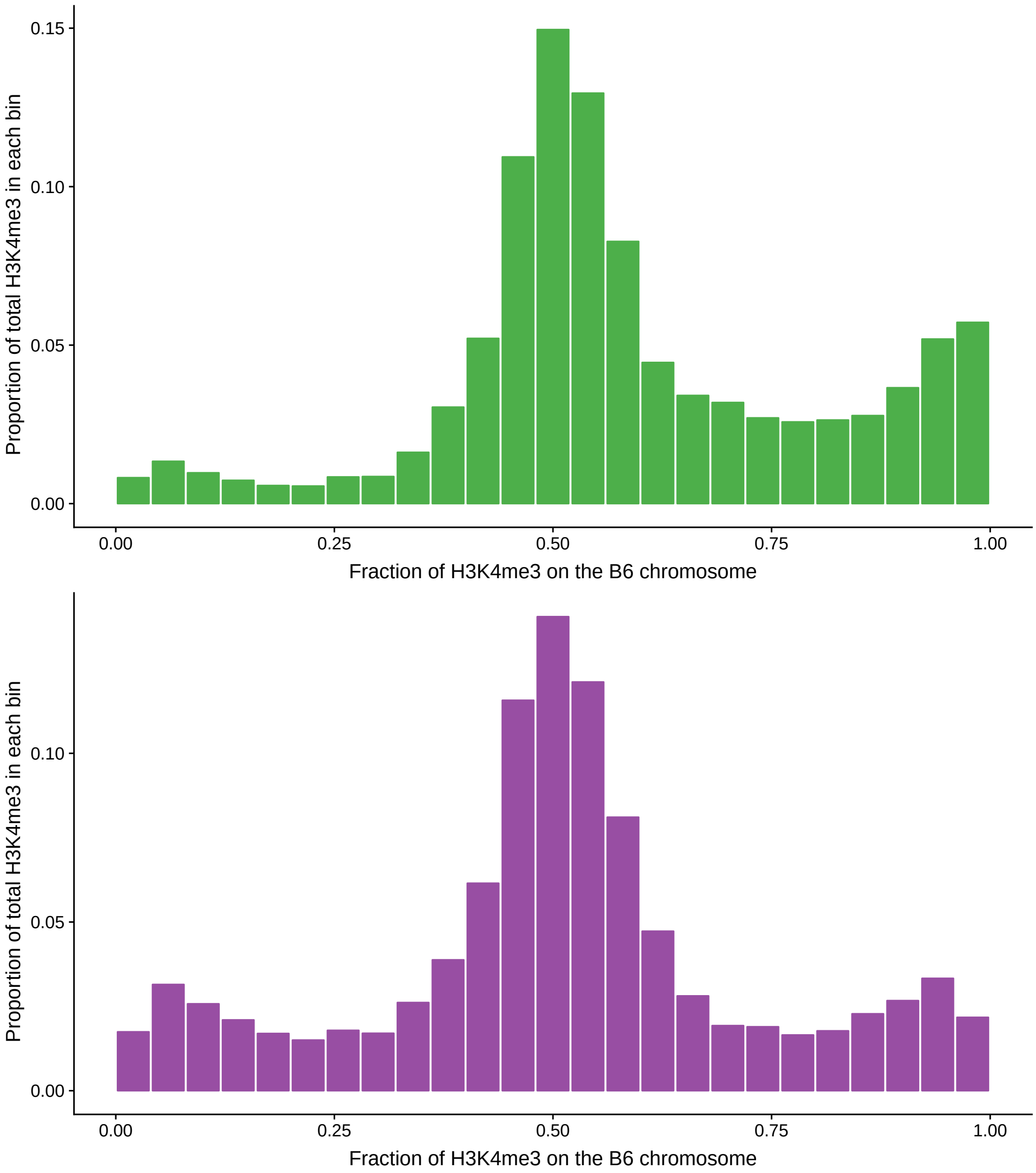

Figure S11: Comparison of the binding preferences of PRDM9$^{\mathrm{CAST}}$ (top) and PRDM9$^{\mathrm{HUM}}$ (bottom). Hotspots were binned into 25 bins, according to the fraction of H3K4me3 intensity on the B6 chromosome for each hotspot. The leftmost bin contains hotspots that show a strong preference for the CAST chromosome, for example, while the rightmost bin contains hotspots with a strong preference for the B6 chromosome (which we call asymmetric hotspots). The bin in the middle contains hotspots in which PRDM9 binds both chromosomes equally (symmetric hotspots). The heights of the bars show the fraction of the total PRDM9-dependent H3K4me3 that is present in the hotspots in each bin. The fraction of H3K4me3 in the two most asymmetric bins is 6.5% for PRDM9$^{\mathrm{CAST}}$ (from 5.5% of hotspots) and 3.9% for PRDM9$^{\mathrm{HUM}}$ (from 3.7% of hotspots). PRDM9$^{\mathrm{CAST}}$ shows a strong bias overall for binding the B6 chromosome, while PRDM9$^{\mathrm{HUM}}$ does not show an overall bias for either chromosome.

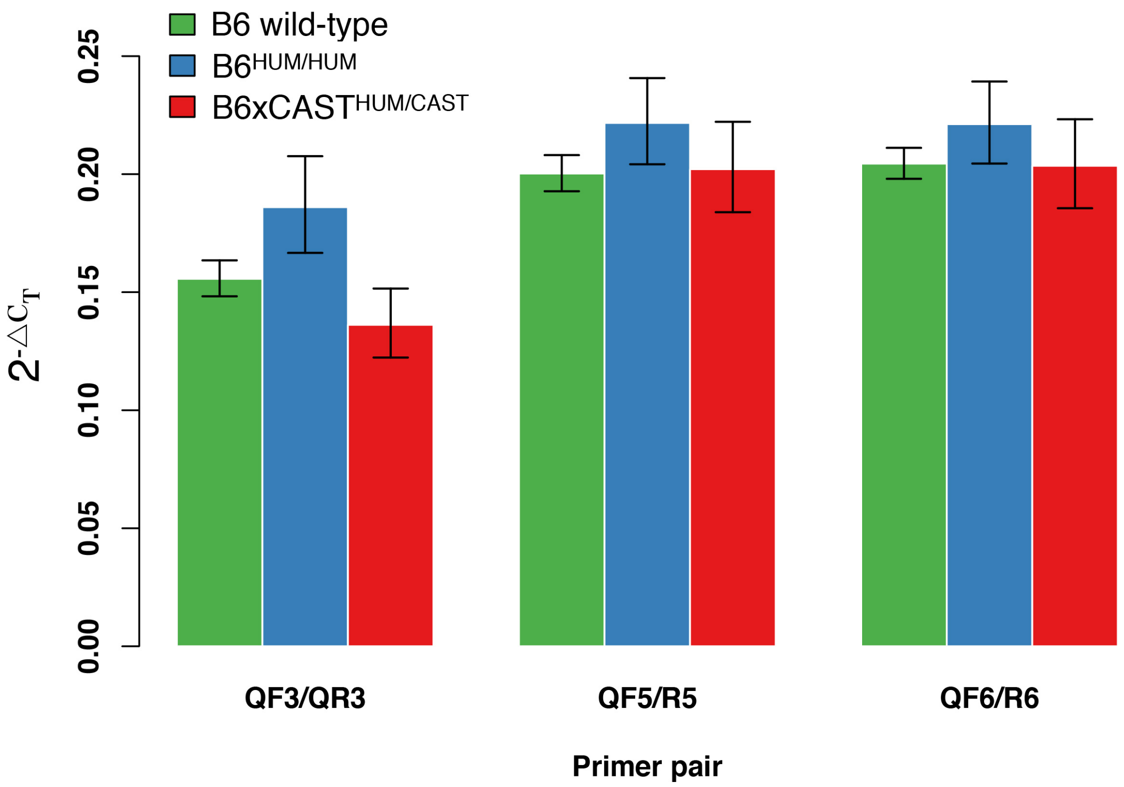

Figure S12: Expression levels of the *Prdm9* transcript within testes of wild-type B6 mice (green), B6 mice homozygous for the humanised *Prdm9* allele *(26)* (blue), and our hybrid mice (red) measured with three independent primer pairs *(25)*. There are no significant differences in the expression level of *Prdm9* between these mice, indicating that the expression level of *Prdm9* alleles is unchanged on each background. Specifically, there is no evidence for a higher level of expression of $Prdm9^{CAST}$ relative to $Prdm9^{\mathrm{HUM}}$ in the hybrid. C_T refers to the fractional PCR cycle number at which a fixed threshold of amplified target is reached *(67)*, and ΔC_T refers to the same quantity relative to a reference gene *(25)* ($n = 3$ for each genotype, quantity shown is $2^{-\mu}$ where μ is the average ΔC_T, bars show $2^{-\mu\pm\sigma}$ where σ is 1 standard error in the inference of μ).

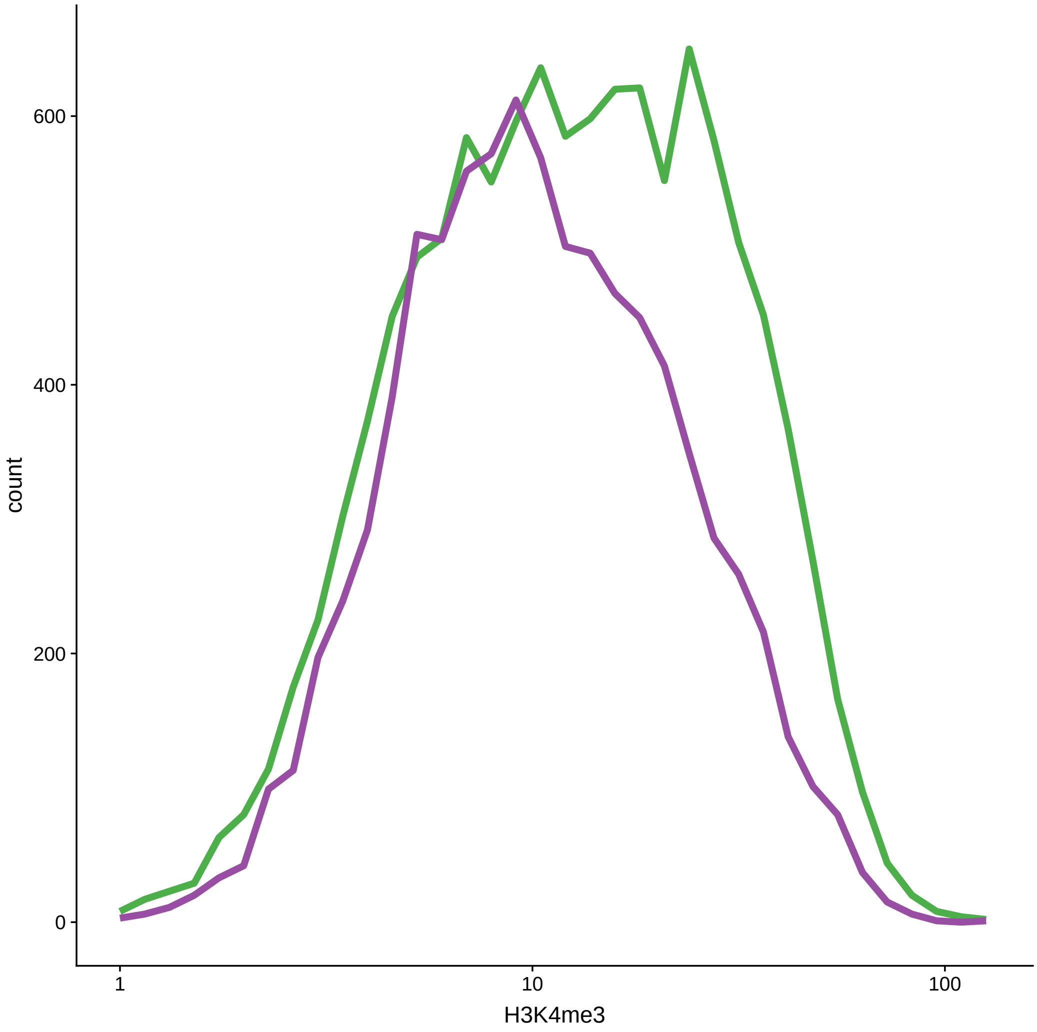

Figure S13: Histograms of H3K4me3 intensities in PRDM9^{CAST} (green) and PRDM9^{HUM} (purple) hotspots.

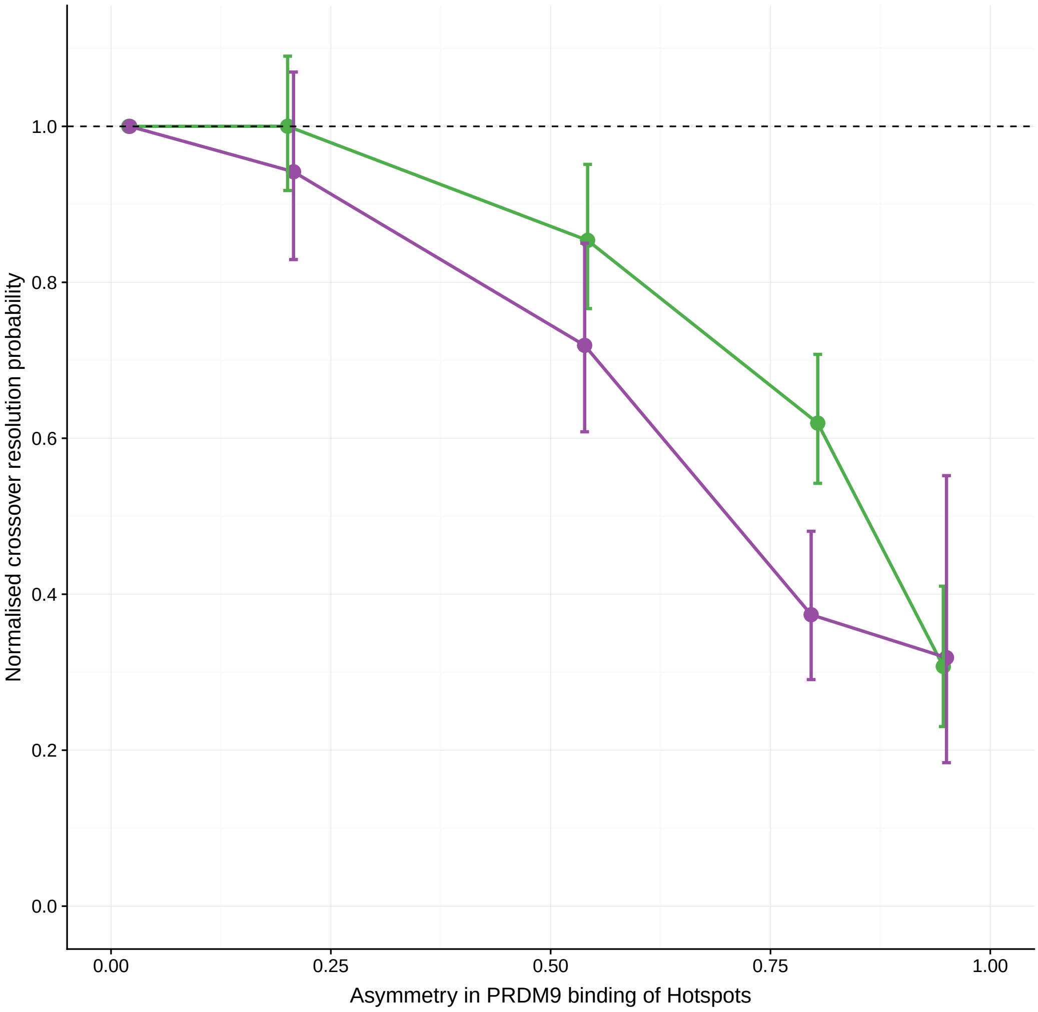

Figure S14: PRDM9^{CAST} (green) and PRDM9^{HUM} (purple) hotspots were binned into five groups depending on the level of asymmetry in H3K4me3 on both homologues. The crossover resolution probability in each bin (y-axis, 1 standard error bars) is plotted against the mean asymmetry of hotspots in that bin (x-axis). The crossover resolution probability was inferred relative to the bin containing the most symmetric hotspots (which was arbitrarily fixed at 1), while taking into account differences in total H3K4me3.

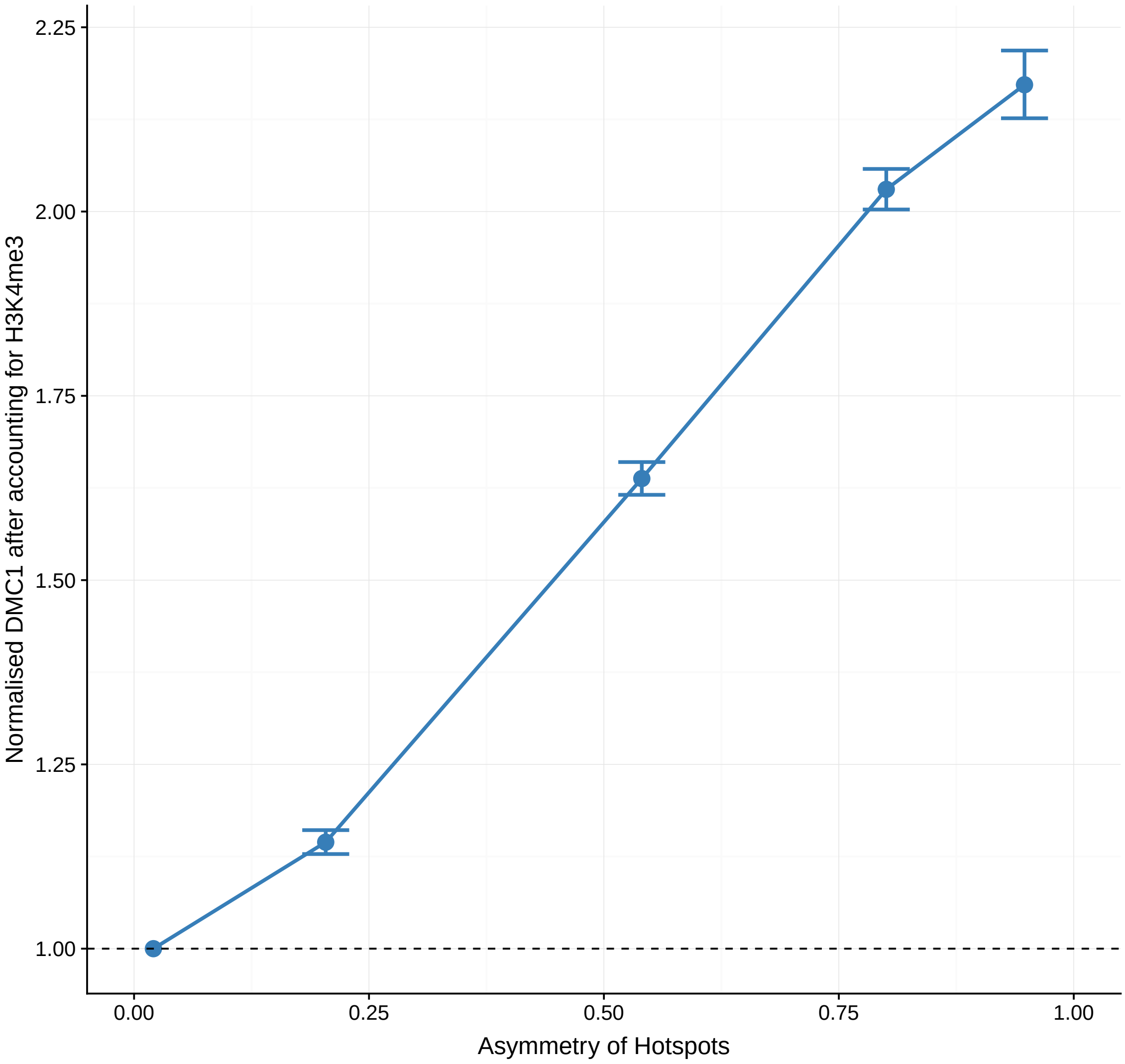

Figure S15: For the same total H3K4me3, asymmetric hotspots have greater DMC1 than symmetric hotspots. Hotspots were binned into five groups depending on the level of asymmetry in PRDM9 binding of the homologues (the same bins as in Fig. 3A). The DMC1 measure in each bin (y-axis, 1 standard bars) is shown against the mean asymmetry of hotspots in that bin (x-axis). DMC1 measure was normalised relative to the bin containing the most symmetric hotspots (which was arbitrarily fixed at 1), while taking into account differences in total H3K4me3.

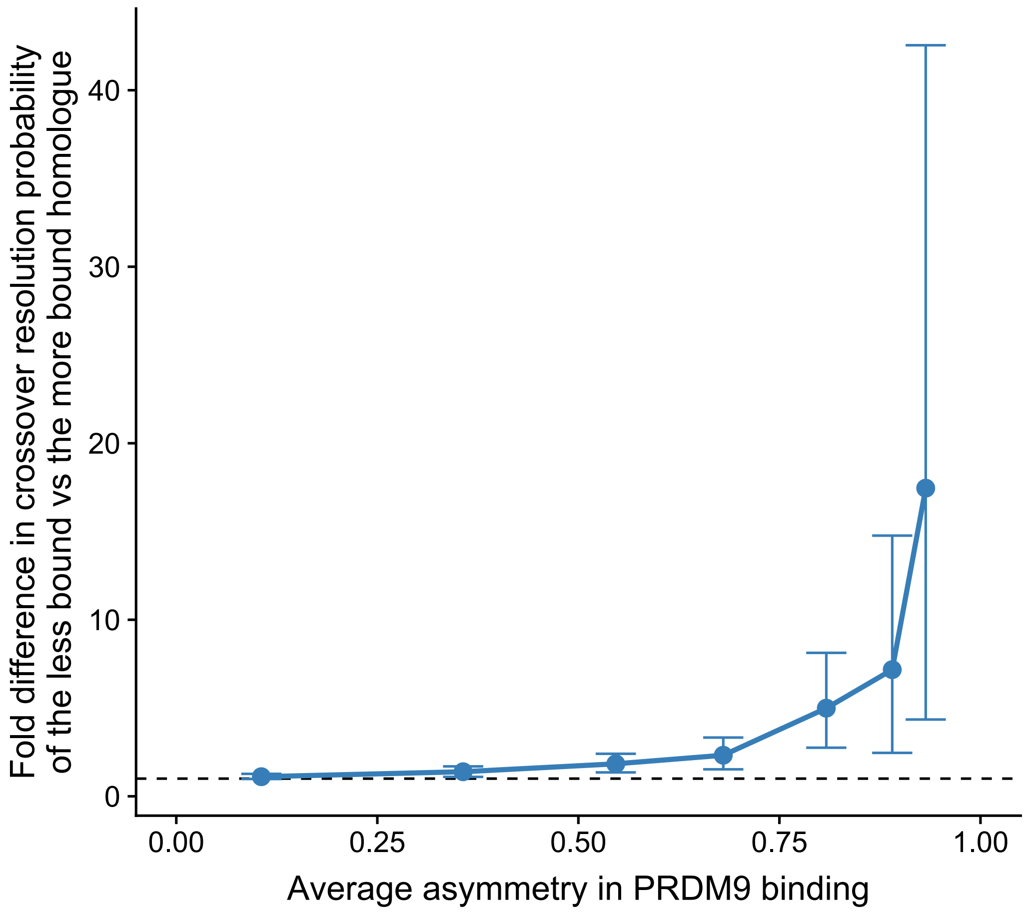

Figure S16: Fold-difference in crossover resolution probability on the less-bound and more-bound homologues in asymmetric hotspots. We bin hotspots with different levels of PRDM9 binding asymmetry, and plot the ratio of the crossover resolution probability for the less-bound homologue relative to the more-bound homologue for hotspots in each bin. If both homologues were equally affected by asymmetry, the ratio of the crossover resolution probabilities would be 1 (dashed black line). Crossover resolution probability is higher on the less-bound homologue relative to the more-bound homologue for more asymmetric hotspots (90% confidence intervals estimated by bootstrap re-sampling).

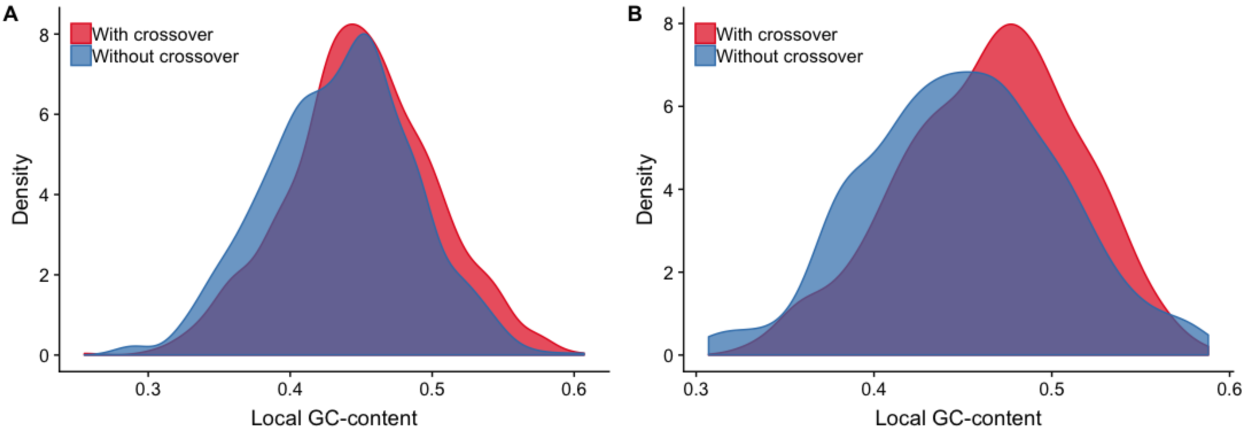

Figure S17: The effect of local GC-content (defined as the fraction of GC-bases in the ±500 bp around the hotspot centre) on crossover outcome in (**A**) PRDM9$^{\mathrm{CAST}}$ hotspots (n=894, paired t-test, p=9.6×10^{-10}) and (**B**) PRDM9$^{\mathrm{HUM}}$ (n=471, paired t-test, p=1.7×10^{-6}) hotspots. Each hotspot which had a crossover was paired with another hotspot which lacked a crossover but was on the same autosome and had very similar H3K4me3 on both homologues *(25)*. The local GC-content was compared between these two matched sets.

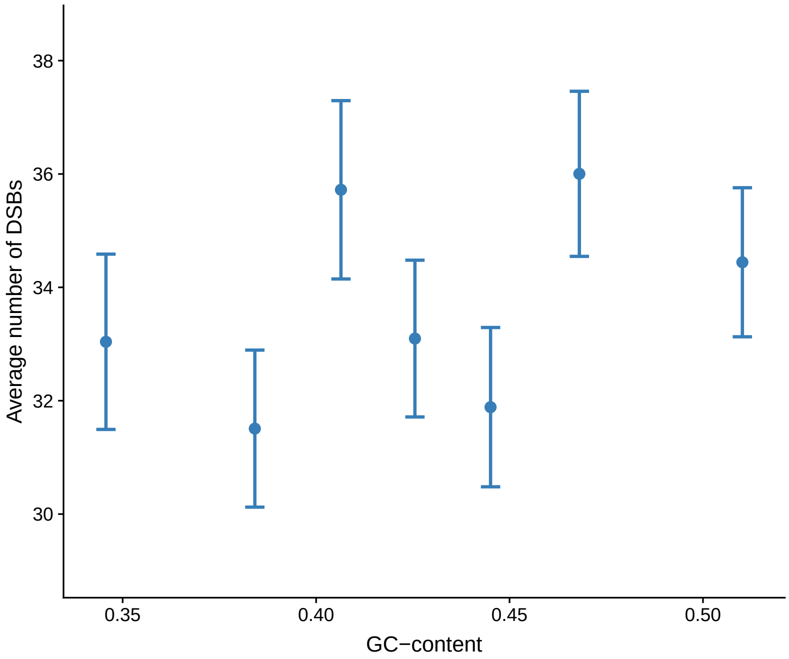

Figure S18: Local GC-content (± 500 bp around hotspot centre) and the average number of DSBs in PRDM9-dependent hotspots, as measured by SPO11-oligos in the B6 wild-type mouse (SPO11-oligos data from *(29))*. Hotspots with evidence of PRDM9-independent H3K4me3 were excluded. There is no evidence for a correlation between the number of DSBs per hotspot and the local GC-content (p=0.25, test for Pearson's correlation). Bars show 1 standard error.

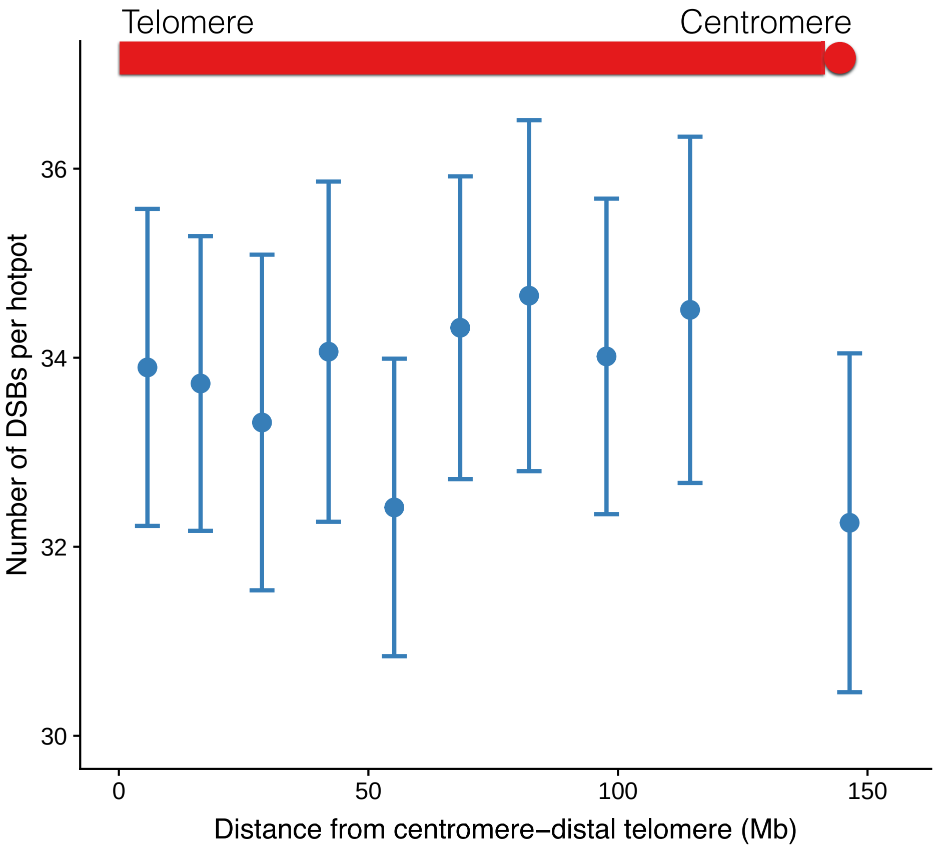

Figure S19: Distance from the centomere-distal telomere and the average number of DSBs, as measured by SPO11 oligos, in hotspots in the B6 wild-type mouse (data from *(29)*). Hotspots with evidence of PRDM9-independent H3K4me3 were excluded. The number of DSBs per hotspot is not correlated with the distance from telomere (p=0.80, test for Pearson's correlation). Bars show 1 standard error.

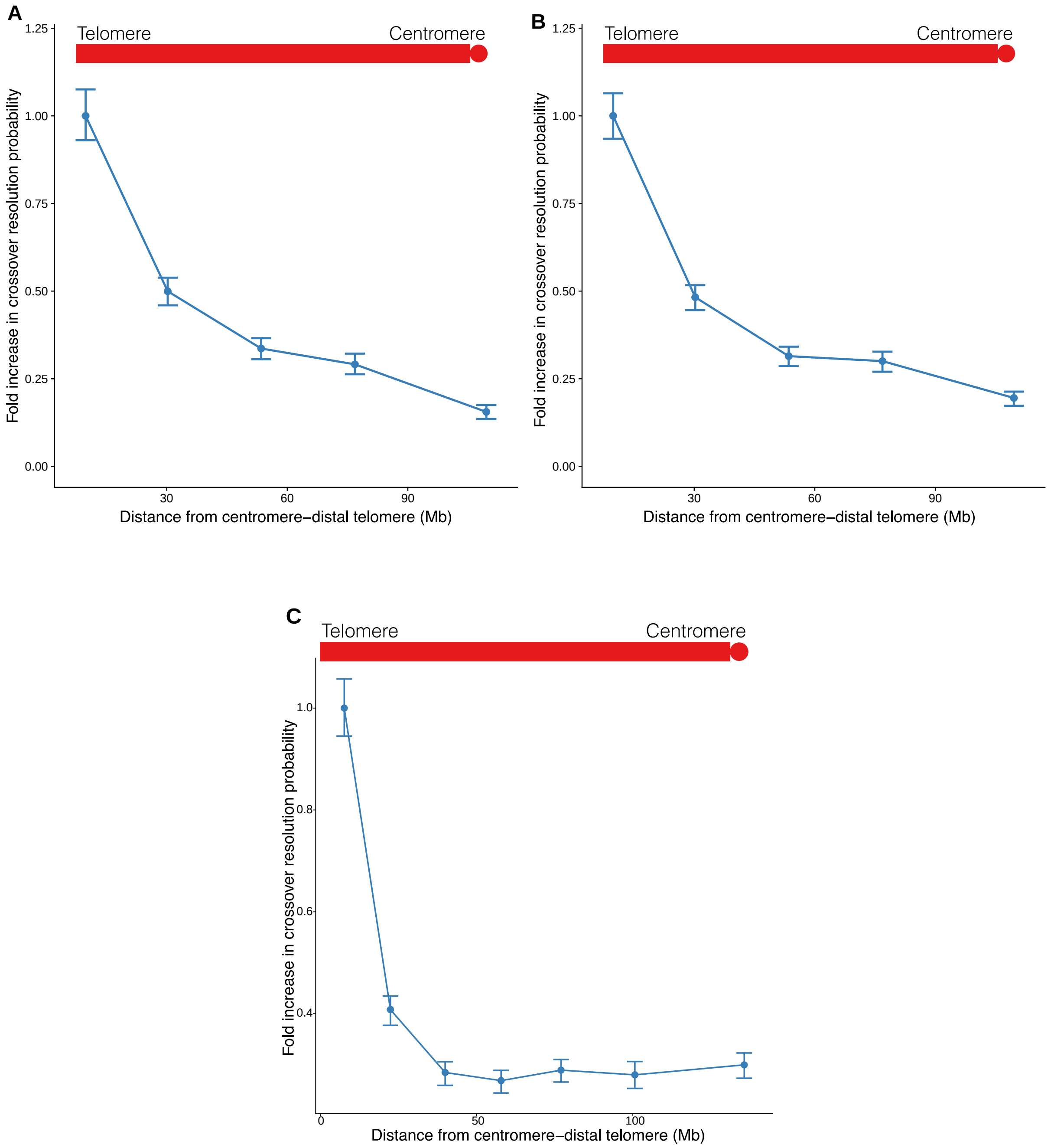

Figure S20: Crossover resolution probability is affected by proximity to the centromere-distal telomere. In Fig. 4B, we had filtered out chromosomes that had more than one crossover in an individual sperm, as we reasoned that the placement of crossovers in those situations would be affected by crossover interference. Here, we examine alternative views, with and without filtering out those chromosomes: (**A**) As in Fig. 4B, but restricting to autosomes which have >80% chance of having only one crossover per chromosome: chromosomes 3, 6, 8, 9, 12-19. Restricting to these autosomes naturally minimises the impact of crossover interference. (**B**) As in **A**, but without filtering out chromosomes with more than one crossover in a sperm. (**C**) As in Fig. 4B, but without any filtering, i.e. including all the autosomes and including chromosomes with one or more crossovers in a sperm.

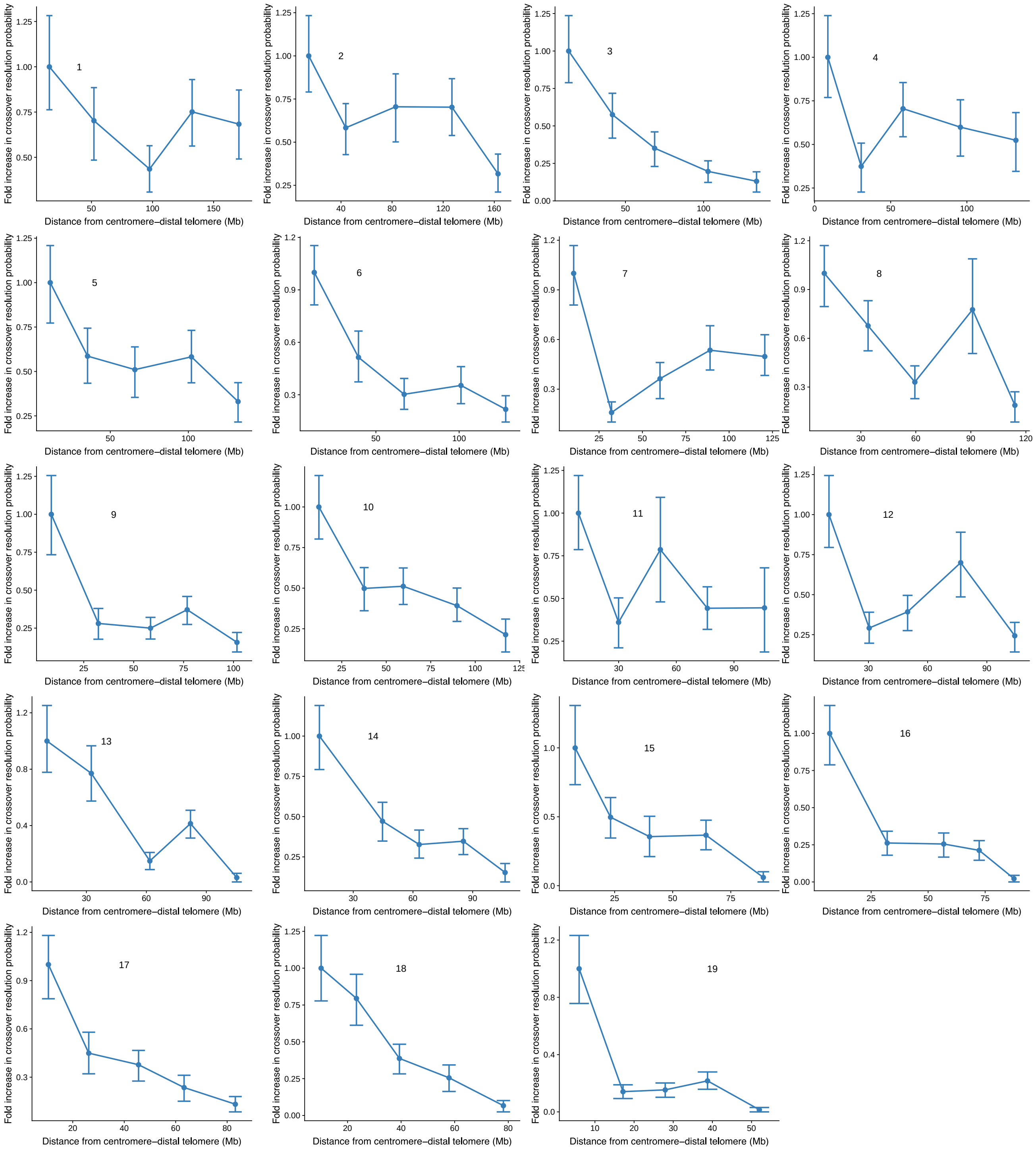

Figure S21: The effect of telomere proximity on crossover resolution probability, as in Fig. 4B but shown separately for each autosome. For all panels, the x-axis is the distance from the centromere-distal telomere in megabases, and the y-axis is the fold-increase in crossover resolution probability. The chromosome number is shown as an inset in each panel.

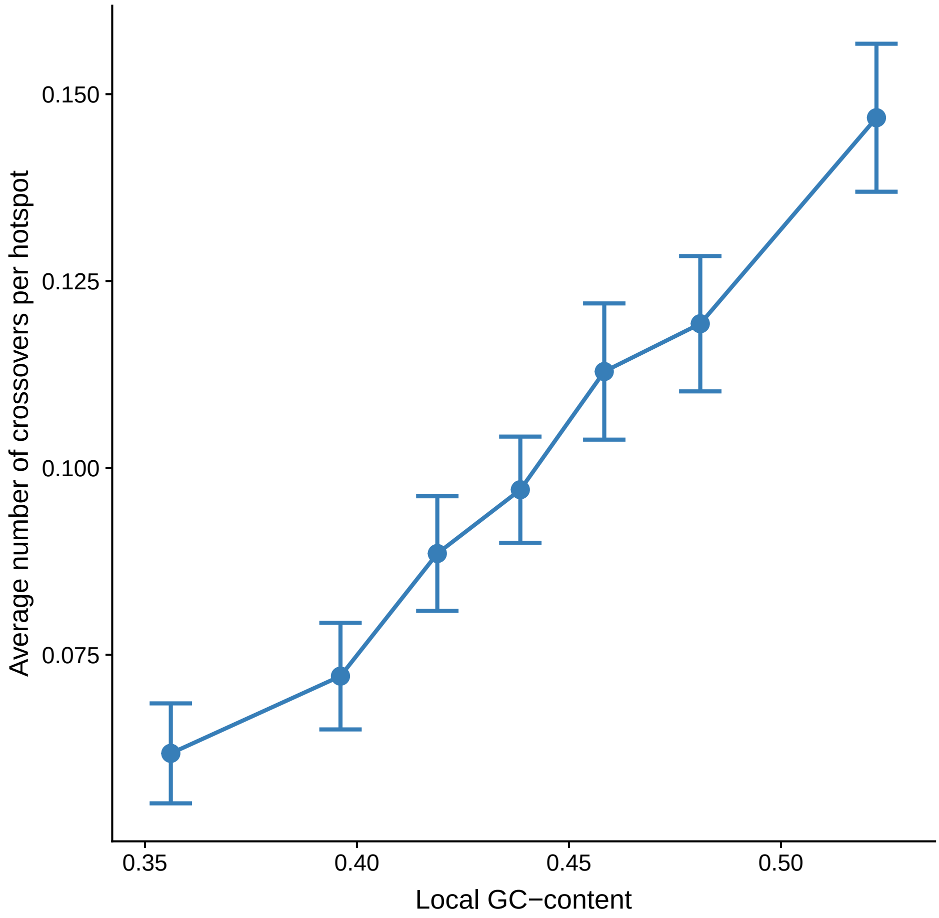

Figure S22: Local GC-content (± 500 bp around hotspot centre) and the average number of crossovers per hotspot (without accounting for H3K4me3) are correlated (p=5×10^{-18}, test for Pearson's correlation). PRDM9-dependent hotspots were divided in to 7 bins according to their local GC-content, and the number of crossovers overlapping them were counted. Hotspots with evidence of PRDM9-independent H3K4me3 were excluded. Bars show 1 standard error.

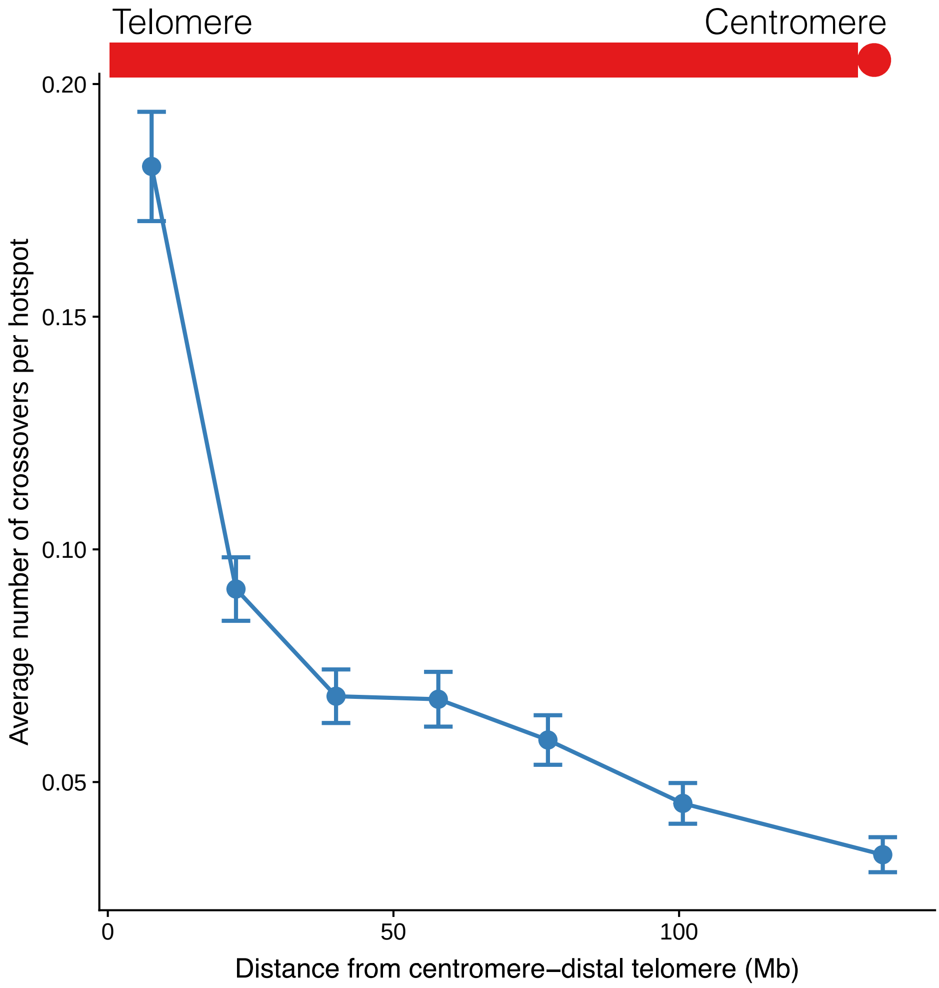

Figure S23: The average number of crossovers per hotspot (without accounting for H3K4me3, compare with Fig. 4B, which does account for H3K4me3) shown against the distance from the centromere-distal telomere. They are significantly negatively correlated ($p=2\times10^{-46}$). Hotspots with evidence of PRDM9-independent H3K4me3 were excluded. Bars show 1 standard error.

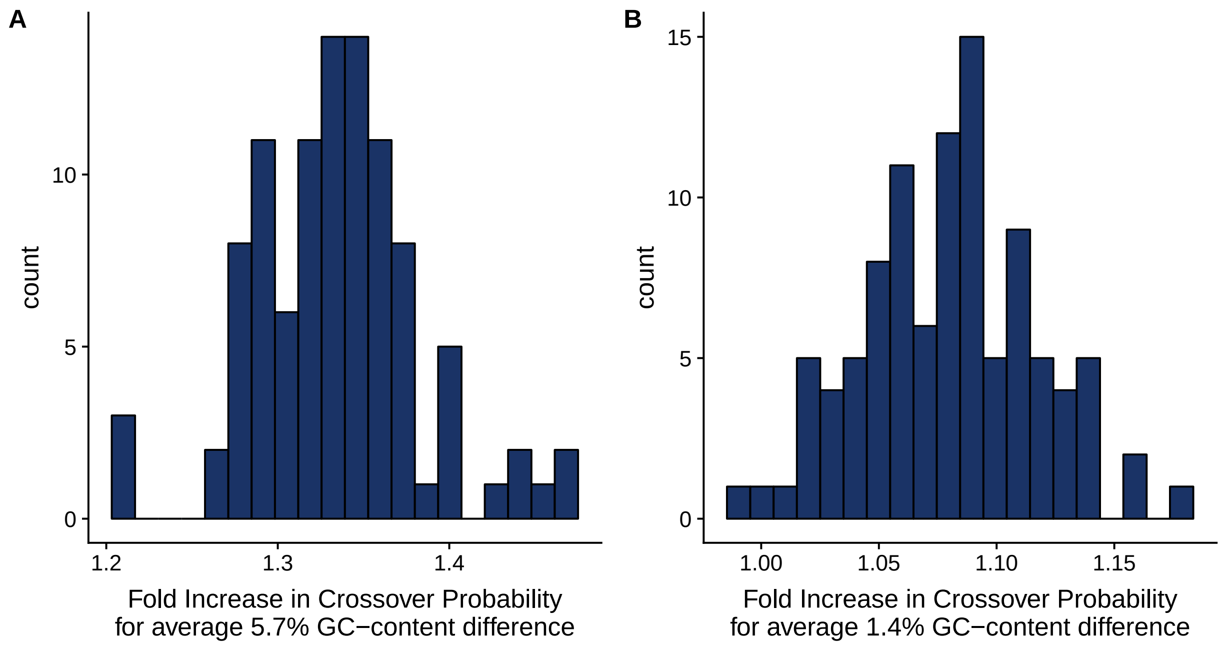

Figure S24: The PRDM9-allele effect on crossovers is distinct from the GC-effect and cannot be explained solely by differences in GC-content in the hotspots activated by PRDM9^{HUM} and PRDM9^{CAST}.

(**A**) We randomly matched each hotspot, regardless of whether it has a crossover, with another hotspot on the same autosome, activated by the same PRDM9 variant and with very similar H3K4me3 on both homologues *(25)*. We placed the hotspot with higher local GC-content in a high-GC bin and the other in a low-GC bin, and repeated the sampling procedure 100 times *(25)*. The average difference in the GC-content between these two bins was 5.7%. We show here the fold-difference in the number of crossovers in the high-GC bin relative to the low-GC bin (median=1.33, mean=1.33).

(**B**) As **A**, with the exception that hotspots assigned to the high-GC and low-GC bins were randomly swapped with probability 24% in order to match the average GC-content difference between PRDM9^{HUM} and PRDM9^{CAST} hotspots *(25)*. The mean and median fold-difference in the number of crossovers between the two bins is 1.08. The allele effect that may be attributable to GC-content (8%) is smaller than the overall size of the allele-effect (32%, see main text).

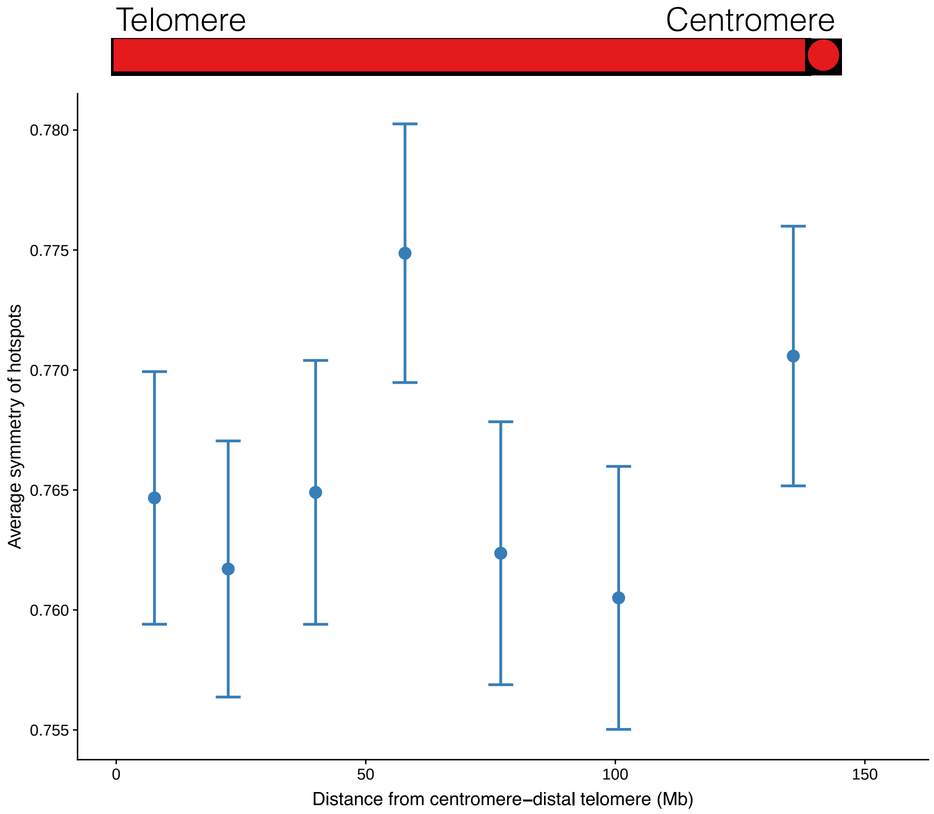

Figure S25: The effect of telomere proximity is distinct from the effect of hotspot asymmetry. Here we show the average symmetry of hotspots relative to the distance of the hotspot from the centromere-distal telomere. Hotspots in the hybrid mouse were divided into 7 bins depending on their distance from the distal telomere. Hotspots with evidence of PRDM9-independent H3K4me3 were excluded. The symmetry of hotspots is not correlated with the distance from telomere (p=0.77, test for Pearson's correlation). Bars show 1 standard error.

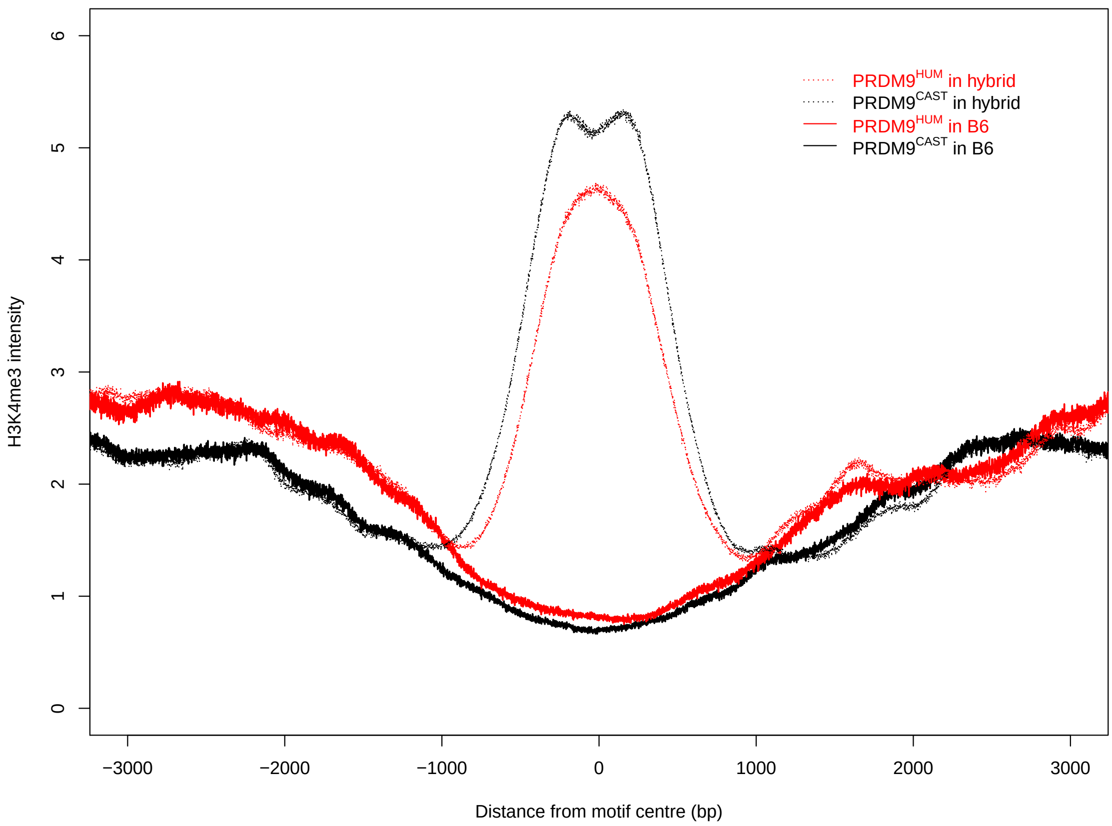

Figure S26: The effect of PRDM9 variant on crossovers is not explained by differences in *a priori* or PRDM9-independent H3K4me3 at their respective hotspot sites. Here we show a comparison of average H3K4me3 level in PRDM9^{CAST} (black) and PRDM9^{HUM} (red) hotspots in this hybrid (dotted lines). The level of H3K4me3 in the testes tissue at the same sites in a wild-type B6 mouse, which lacks both alleles, is also shown (solid lines) to compare their levels of H3K4me3 in the absence of PRDM9 binding. The data in the hybrid mouse were re-scaled (divided by 1.74) to match the background read-depths in the B6 mouse. The hotspots of both variants show a low level of H3K4me3 at sites that become hotspots in the presence of PRDM9, as has been previously noted for the B6 allele *(26)*.

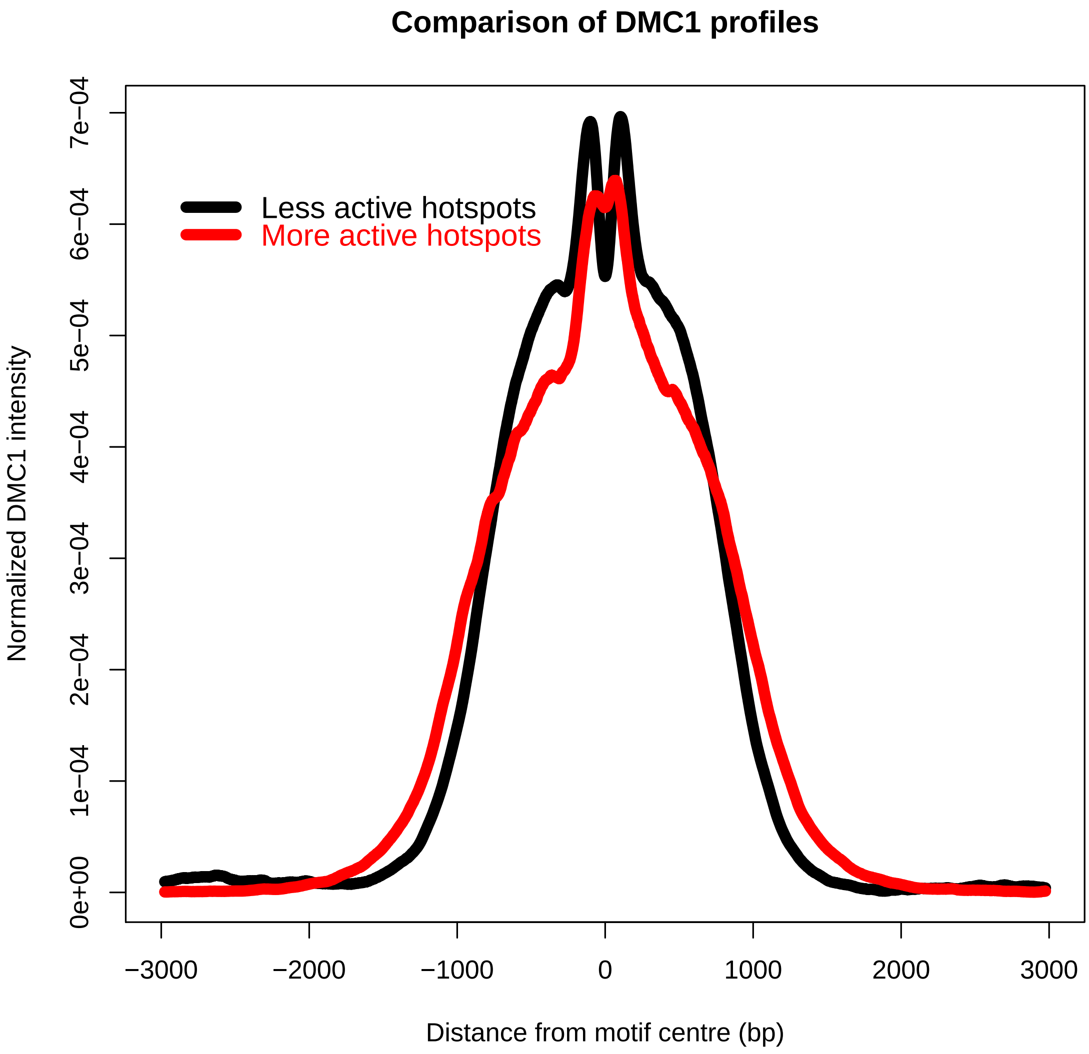

Figure S27: Lower DMC1 per DSB in more active B6 hotspots is not explained by differences in end-resection or the widths of DMC1 loading. Here we show the widths of DMC1 presence in more active (red) and less active (black) hotspots in the wild-type B6 mouse. Hotspots were ordered by H3K4me3 intensity and split into 4 bins (the two most extreme bins are shown), such that the total H3K4me3 in each bin was the same. Hotspots with evidence of PRDM9-independent H3K4me3 were excluded. To get the DMC1 profile for each bin, ChIP-seq reads relative to the motif centre in each hotspot were added up for the hotspots in that bin. To compare the overall shapes, the profiles were normalised to have the same area under the curve for each bin (arbitrarily set to 1). The profile of more active hotspots is subtly wider than that for less active hotspots. This rules out the effect of H3K4me3 on the *initiating* chromosome in reducing the degree of end resection or width of DMC1 loading on it, suggesting that there may instead be a subtle effect in the opposite direction.

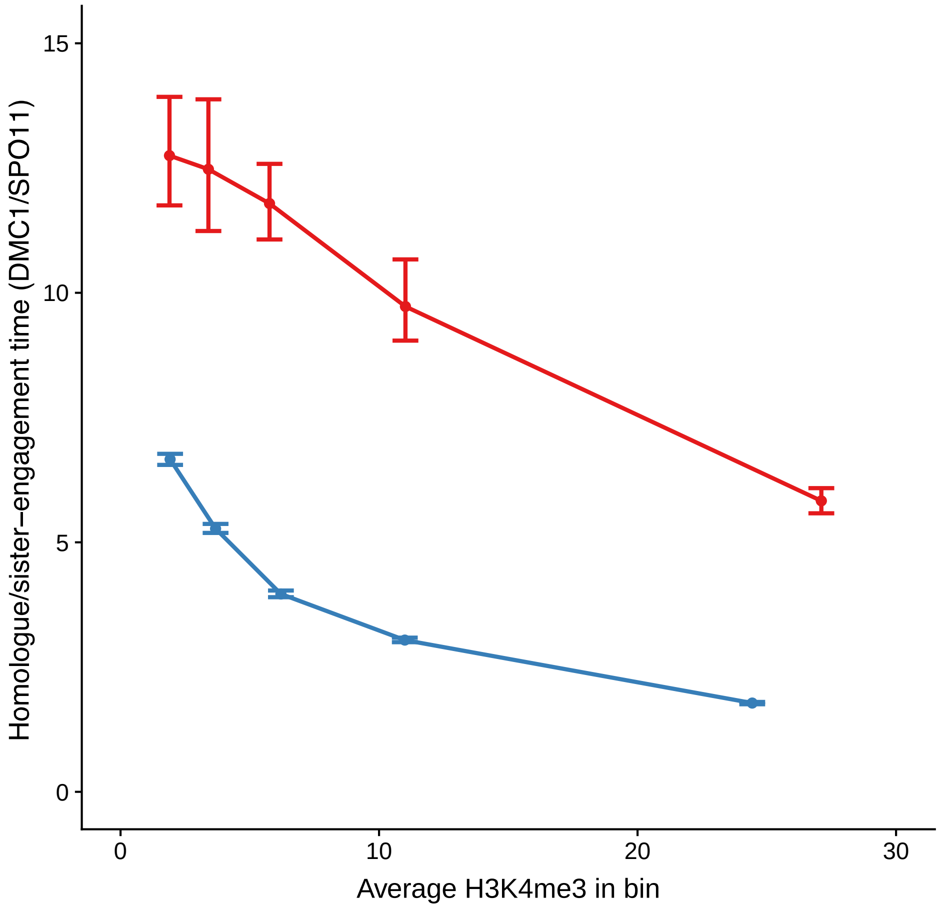

Figure S28: Homologue-(or sister-) engagement time in the wild-type B6 mouse for the X chromosome (red) and the autosomes (blue). Hotspots were ordered by their H3K4me3 intensity and divided into 5 bins with equal numbers of hotspots. The ratio of total DMC1 with the total SPO11 in each bin (y-axis) is shown relative to the mean H3K4me3 (x-axis) in each bin. Hotspots with evidence of PRDM9-independent H3K4me3 or with zero SPO11-oligo reads were excluded. Bars show 1 standard error.

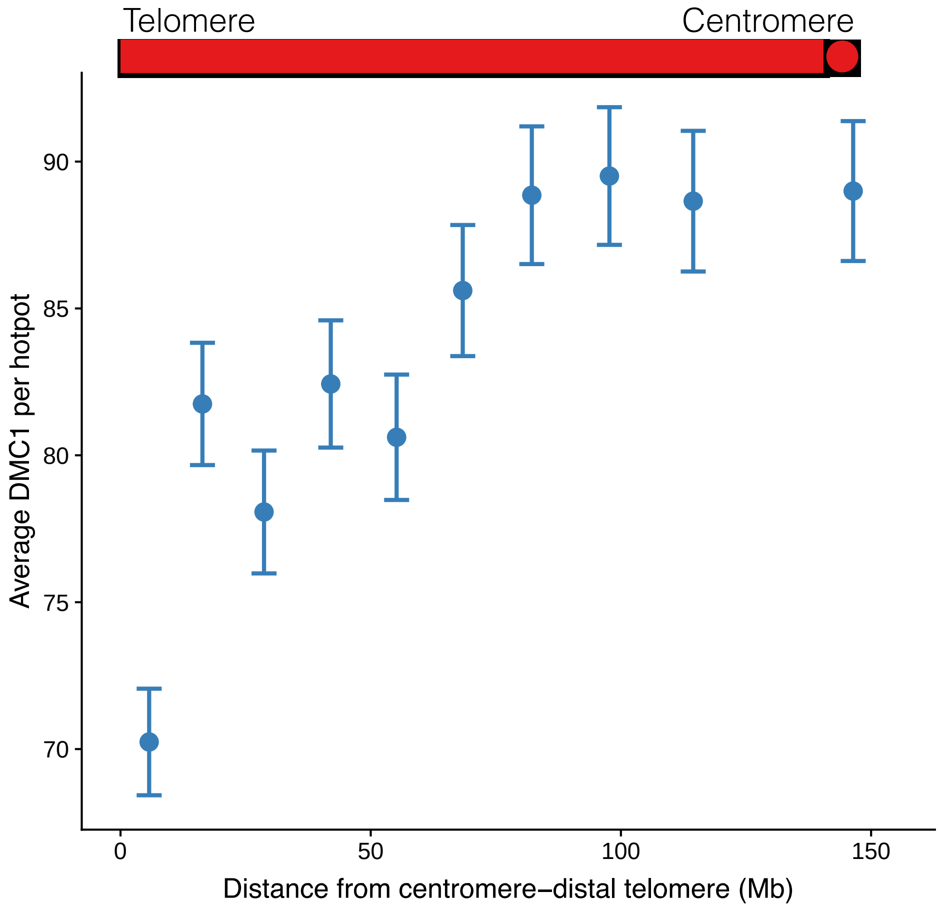

Figure S29: Distance from the centomere-distal telomere and the average DMC1 measure in hotspots in the B6 wild-type mouse (data from *(26)*, 1 standard error bars). Hotspots with evidence of PRDM9-independent H3K4me3 were excluded. DMC1 per hotspot is correlated with the distance from the telomere (p=2×10^{-12}, test for Pearson's correlation).

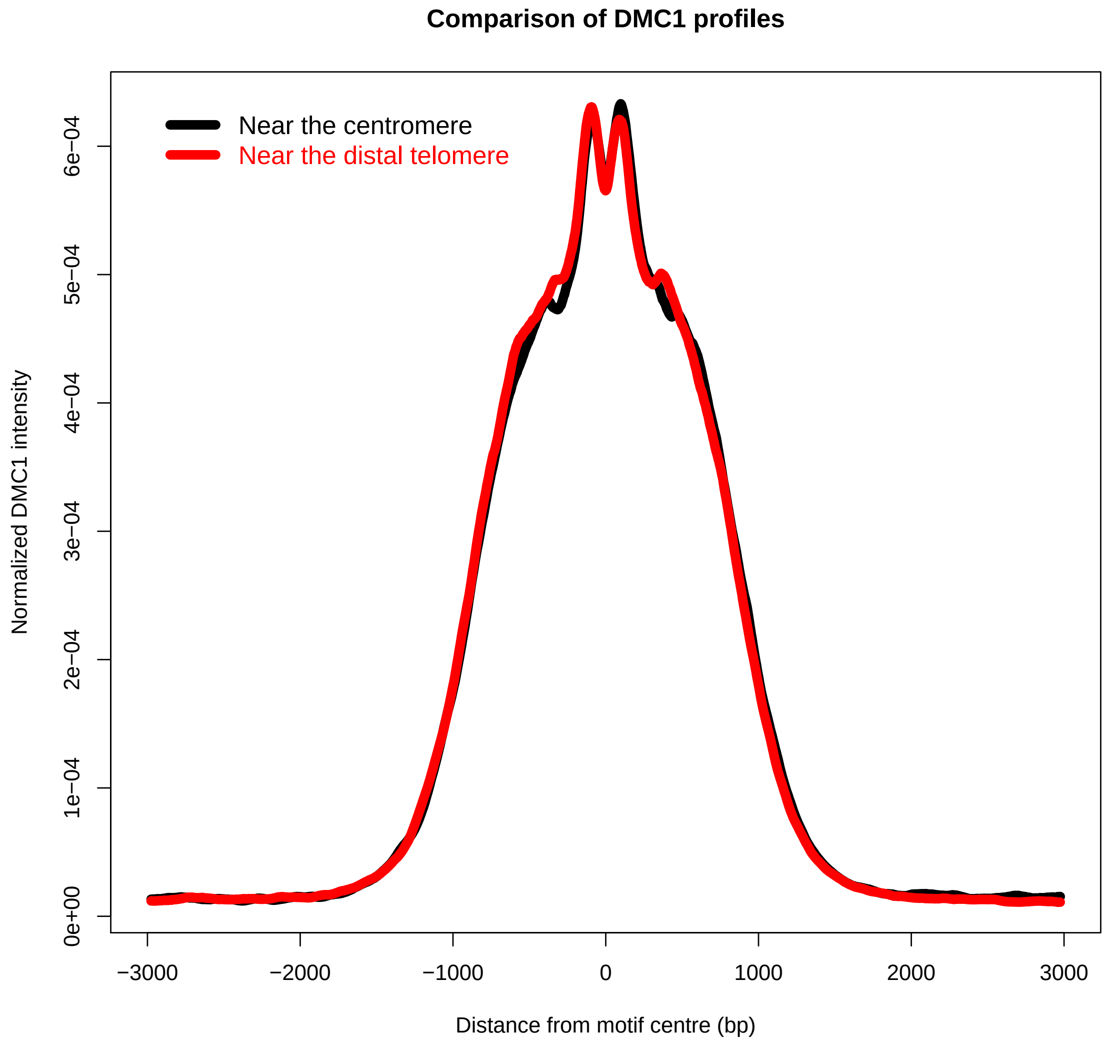

Figure S30: Comparison of the widths of DMC1 presence in hotspots closer to the centromere (black) and those closer to the centromere-distal telomere (red) in the B6 wild-type mouse. Each autosome was split into 4 equal regions by length, with one quarter containing hotspots closest to the centromere, and another quarter containing hotspots closest to the distal telomere. To get the DMC1 profile for each quarter, DMC1 ChIP-seq reads relative to the motif centre in each hotspot were added up for the hotspots in that quarter. To compare the overall shapes, the profiles were normalised to have the same area under the curve (arbitrarily set to 1). There is no evidence to suggest a difference in width of DMC1 loading or end-resection between the two groups of hotspots.

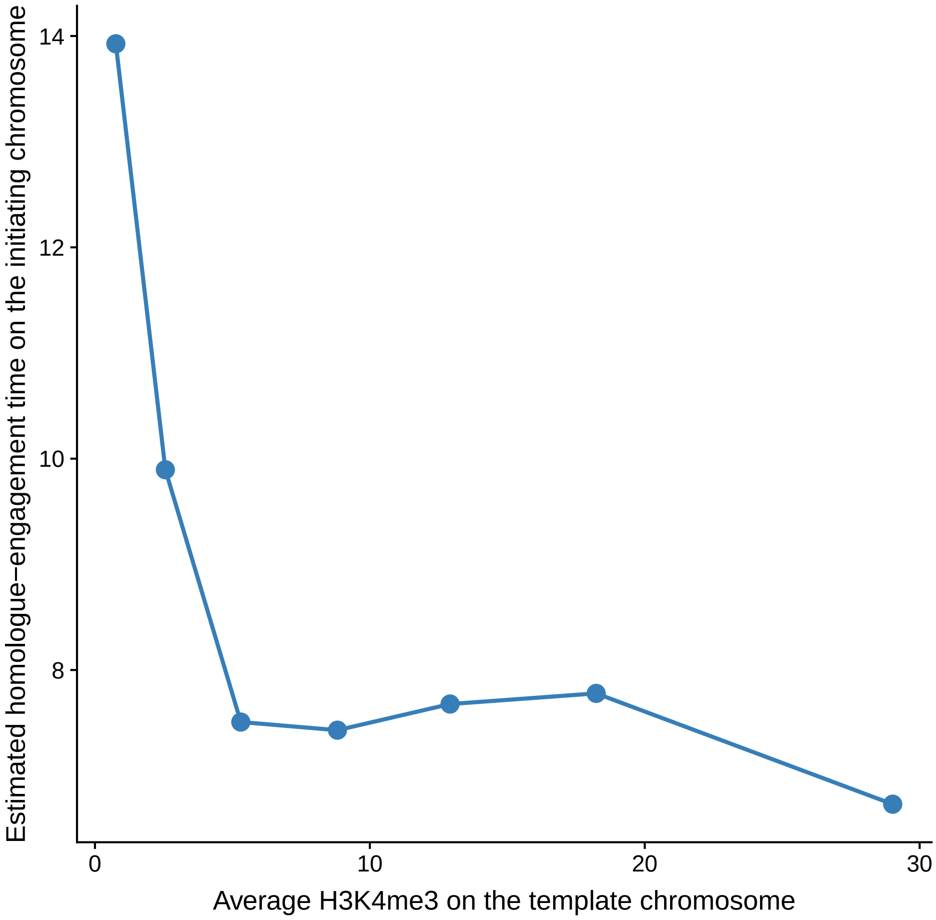

Figure S31: Estimated homologue-engagement time on the initiating chromosome against H3K4me3 on the template chromosome in the hybrid. All potential sites for recombination initiation were binned into 7 bins, so that the total H3K4me3 intensity on the initiating chromosome in each bin was the same. The estimated homologue-engagement time (blue, y-axis) is shown against the mean H3K4me3 on the corresponding template chromosomes (x-axis).

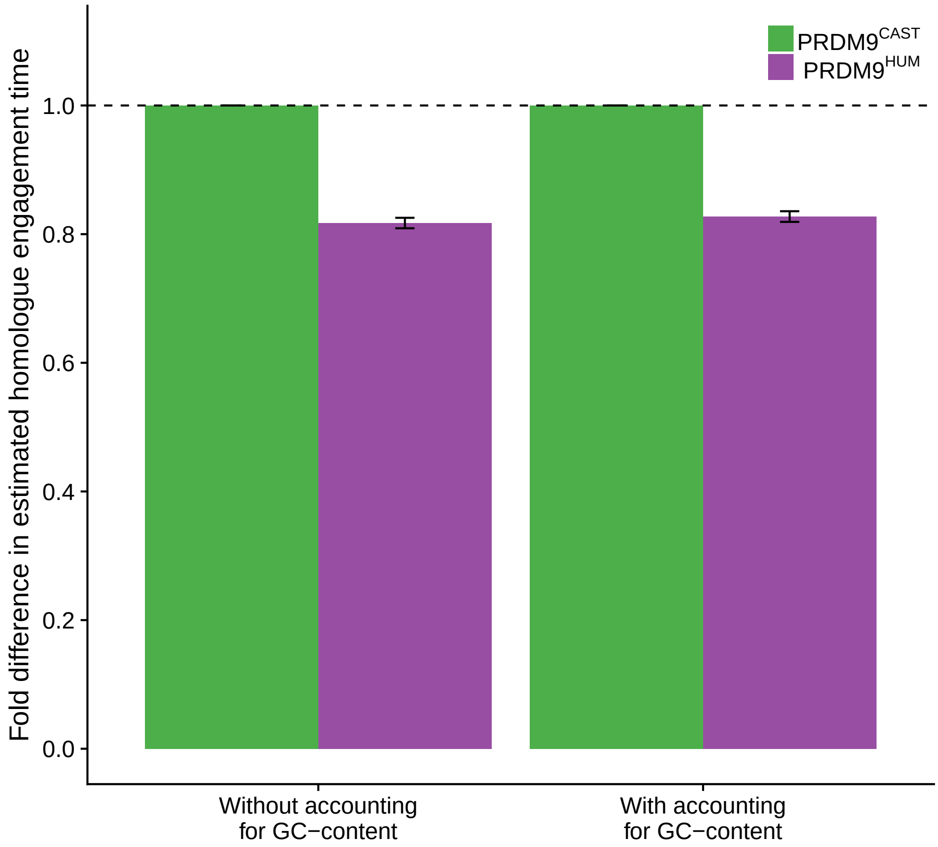

Figure S32: PRDM9$^{\mathrm{HUM}}$ (purple) hotspots have 18% lower estimated homologue engagement time than PRDM9$^{\mathrm{CAST}}$ hotspots (green) after accounting for H3K4me3 on both homologues (left pair of bars, $p = 10^{-90}$). Standard errors and p-values were obtained from generalised linear modelling *(25)*. The effect remains after correcting for local GC-content, indicating that it is in addition to the impact of GC-content (right pair of bars).

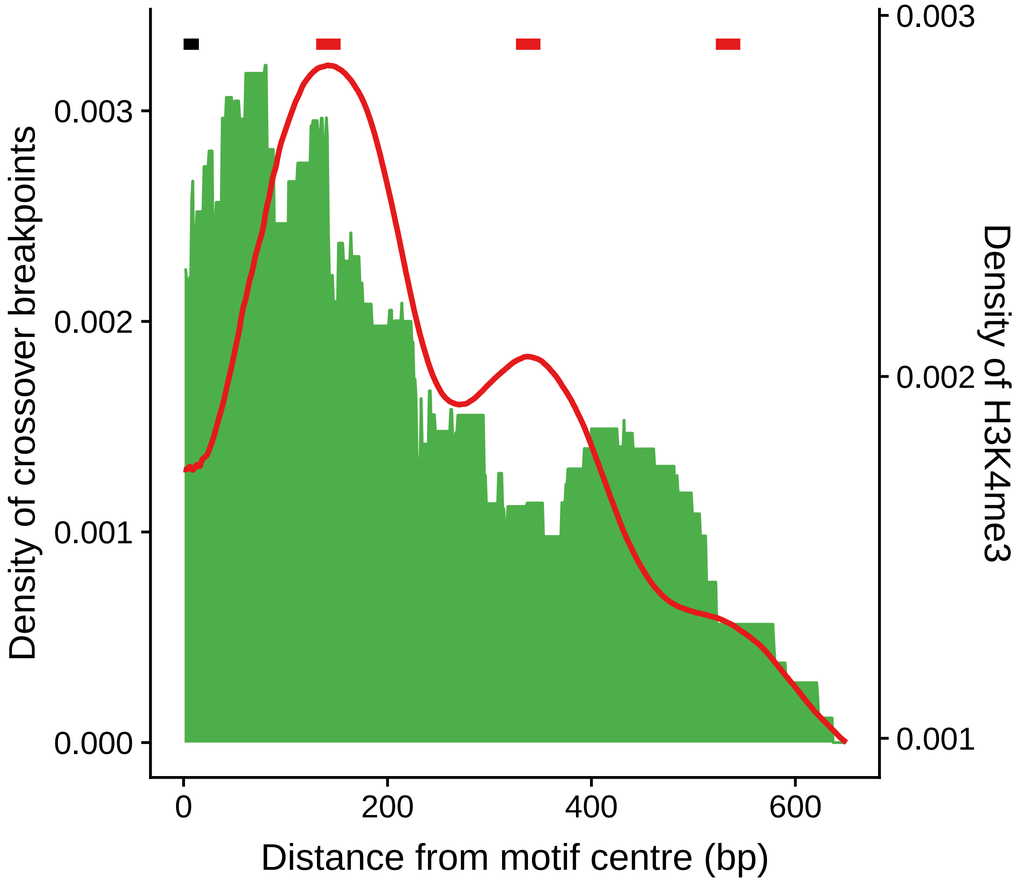

Figure S33: Distribution of crossover breakpoints from the motif centre for crossovers (green) that overlap PRDM9^{CAST} hotspots that are neither symmetric nor asymmetric (intermediate) and contain a well-identified motif site. Crossovers with breakpoint resolution $\leq$ 250 bp are included (n=57). H3K4me3 ChIP-seq with MNase averaged over PRDM9^{CAST} hotspots is shown in red (20 bp smoothing). The red bars at the top show average inferred positions of nucleosomes with the H3K4me3 mark, black bar shows the PRDM9^{CAST} binding site.

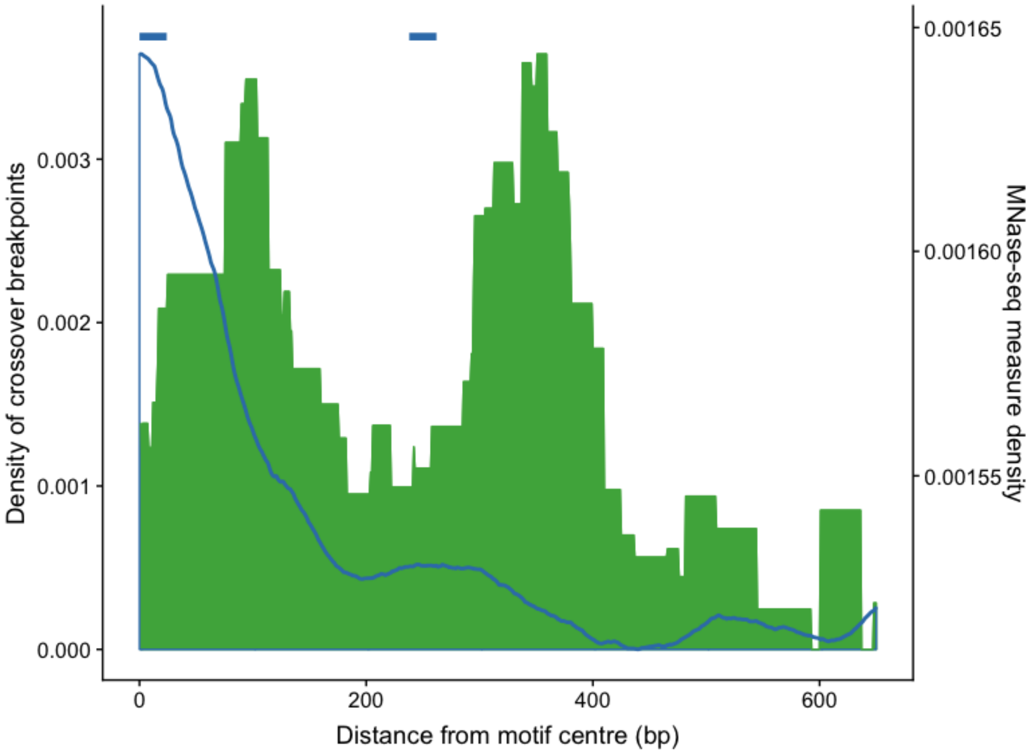

Figure S34: Distribution of crossover breakpoints from the motif centre for crossovers (green) that overlap asymmetric PRDM9$^{\text{CAST}}$ hotspots with a well-identified motif site, and have breakpoint resolution $\leq$ 250 bp (n=33). The density of the measure of MNase-seq in the B6 wild-type mouse at PRDM9$^{\text{CAST}}$ hotspot locations is shown in blue (50 bp smoothing, data from *(38)*). This is an alternative estimate of the nucleosome positioning at hotspot sites when PRDM9 is not bound. Blue bars at the top show average inferred nucleosome positions in B6.

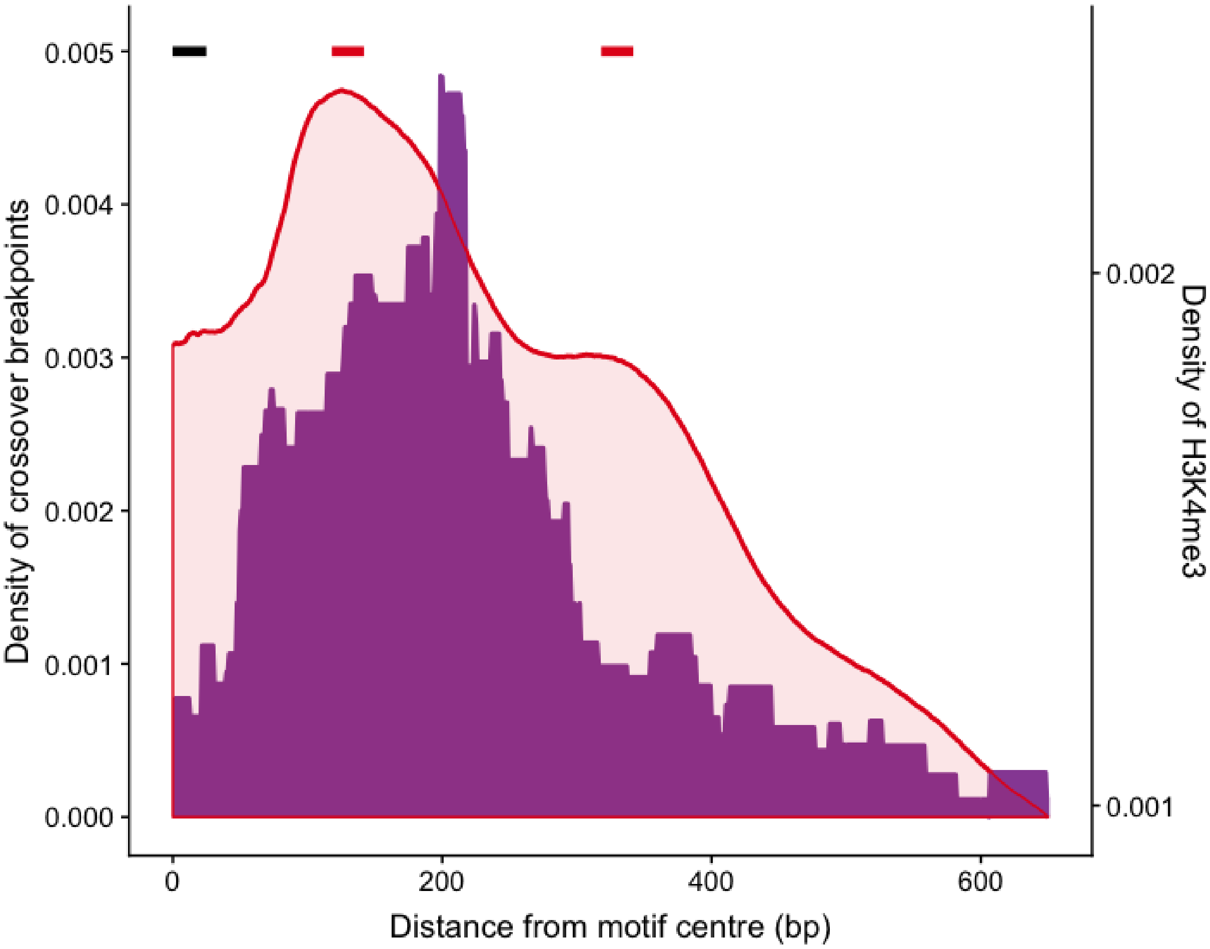

Figure S35: Distribution of crossover breakpoints from the motif centre for crossovers (purple) that overlap symmetric PRDM9^{HUM} hotspots with a well-identified motif site, and have breakpoint resolution $\leq$ 250 bp (n=51). H3K4me3 ChIP-seq with MNase averaged over PRDM9^{HUM} hotspots is shown in red (20 bp smoothing). The red bars at the top show average inferred positions of nucleosomes with the H3K4me3 mark, black bar shows the PRDM9^{HUM} binding site.

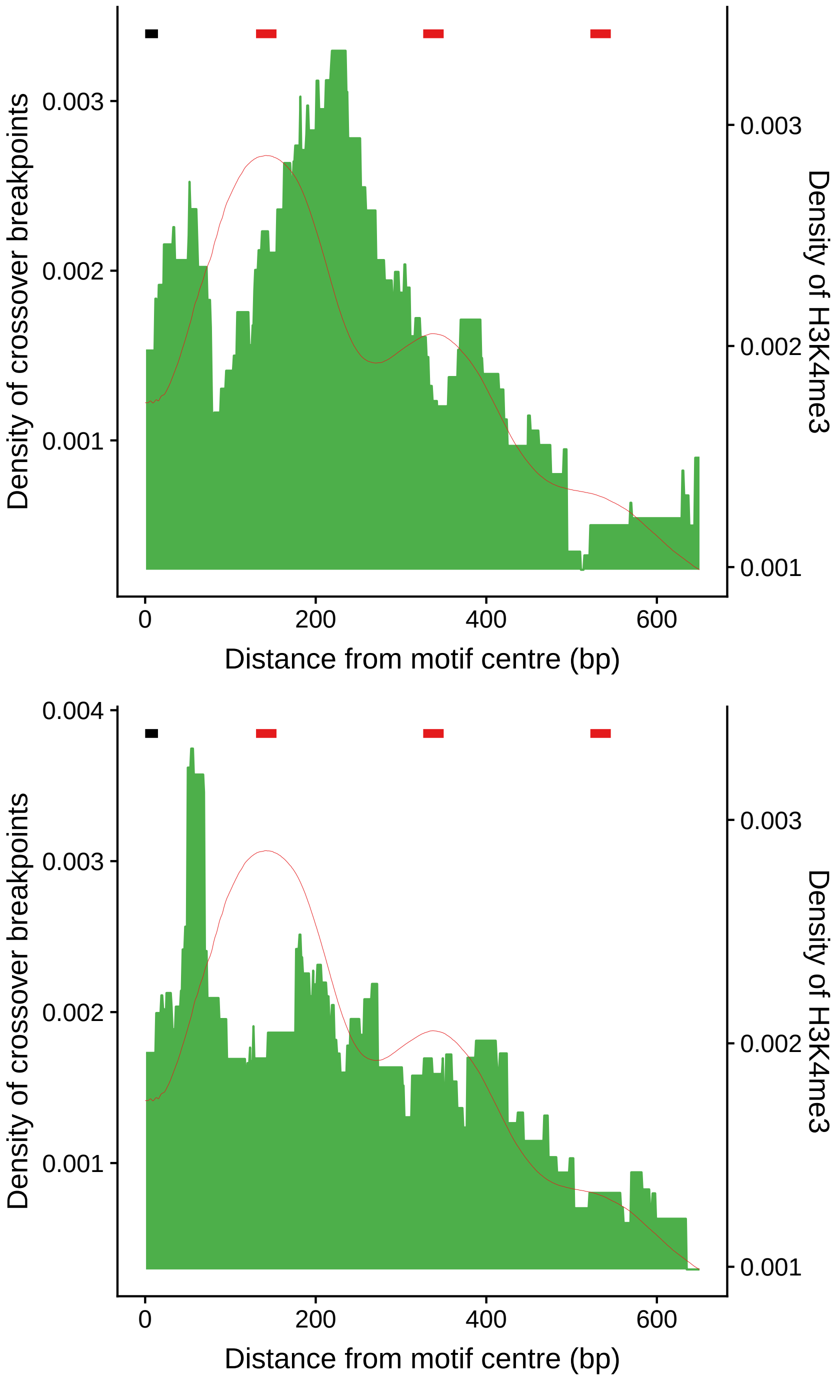

Figure S36: As in Fig. 6A, but with a comparison of crossover breakpoints from the more active (top, n=51) and less active (bottom, n=50) symmetric PRDM9^{CAST} hotspots. The breakpoint distribution for PRDM9^{HUM} hotspots is more similar to that of the more active symmetric PRDM9^{CAST} hotspots.

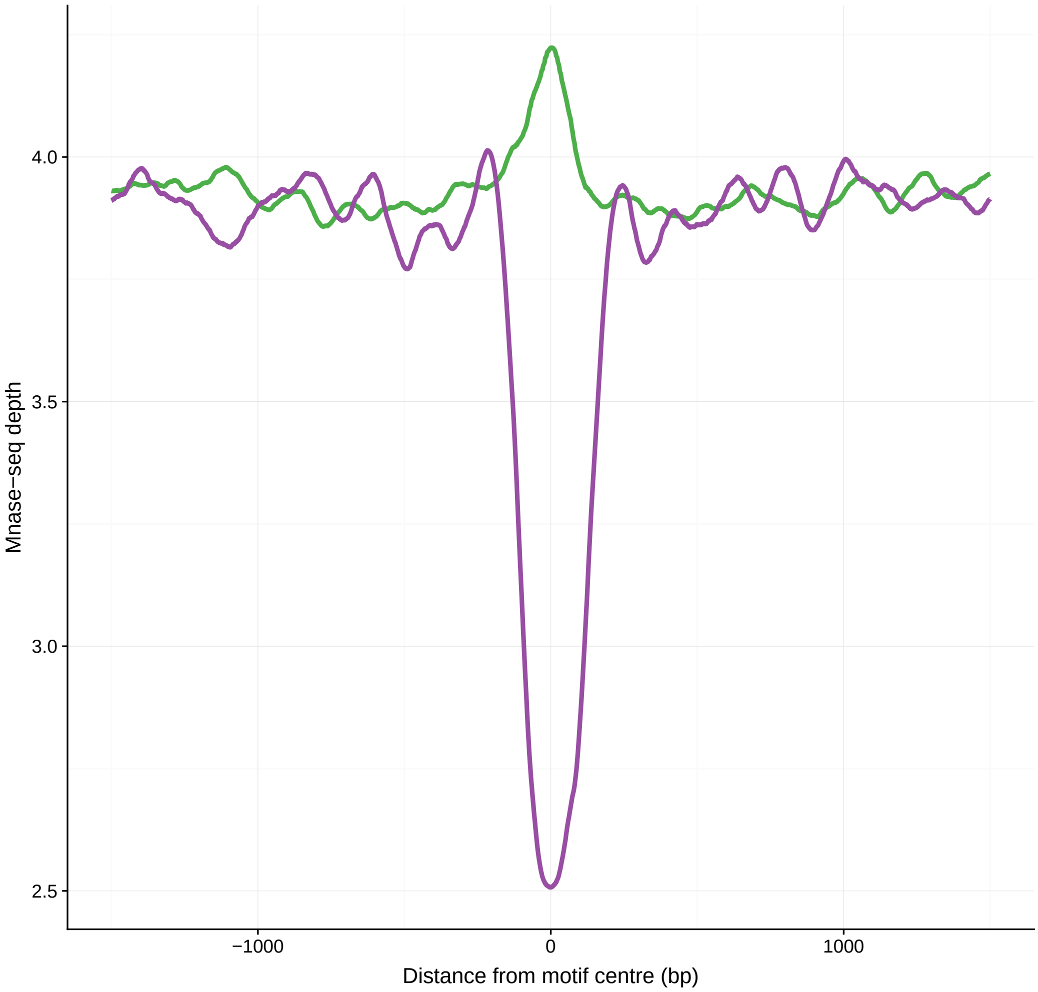

Figure S37: The *a priori* nucleosome occupancy at PRDM9$^{\text{CAST}}$ (green) and PRDM9$^{\text{HUM}}$ (purple) hotspots in the hybrid mouse. The *a priori* nucleosome occupancy was inferred indirectly from Mnase-seq in B6, which that lacks both of these PRDM9 alleles. The plot shows the average MNase-seq measure at PRDM9$^{\text{CAST}}$ and PRDM9$^{\text{HUM}}$ hotspot locations in the B6 mouse testes (data from *(38))* with 50 bp smoothing. Only hotspots with a unique high-quality motif match were included (n=12,224 for PRDM9$^{\text{CAST}}$ and n=5,507 for PRDM9$^{\text{HUM}}$).

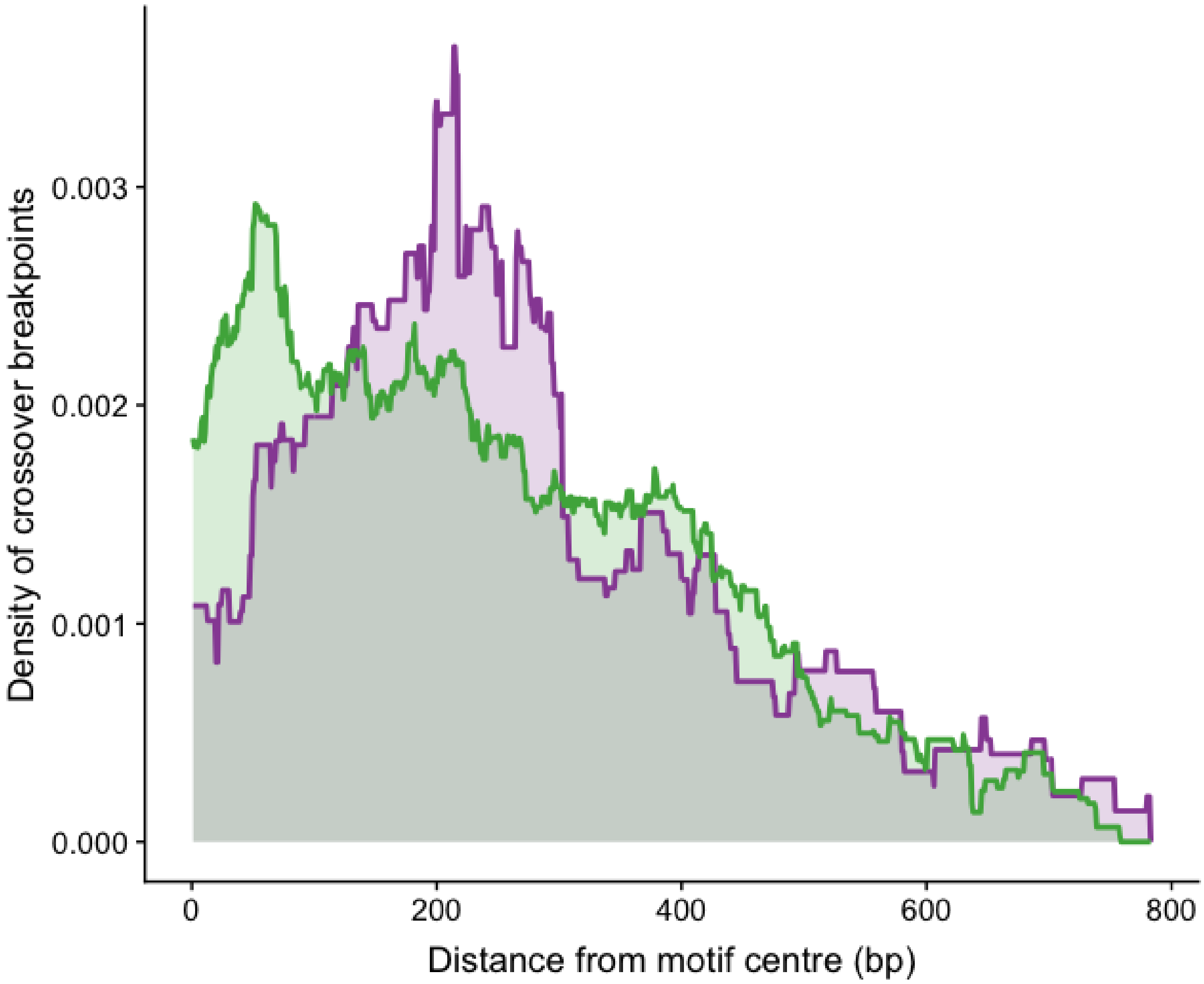

Figure S38: Distribution of the distance of crossover breakpoints from the hotspot center for PRDM9^{CAST} (green) and PRDM9^{HUM} (purple) hotspots for crossovers that were resolved within 250bp (n=222). Crossover breakpoints are known within a region of uncertainty (see Fig. 1C), and we assumed that the true breakpoint is equally likely to occur anywhere in this region (details in *(25)*). The center of a hotspot is defined as the center of the PRDM9-binding motif identified within it, and only hotspots with a unique high-quality motif match were included.

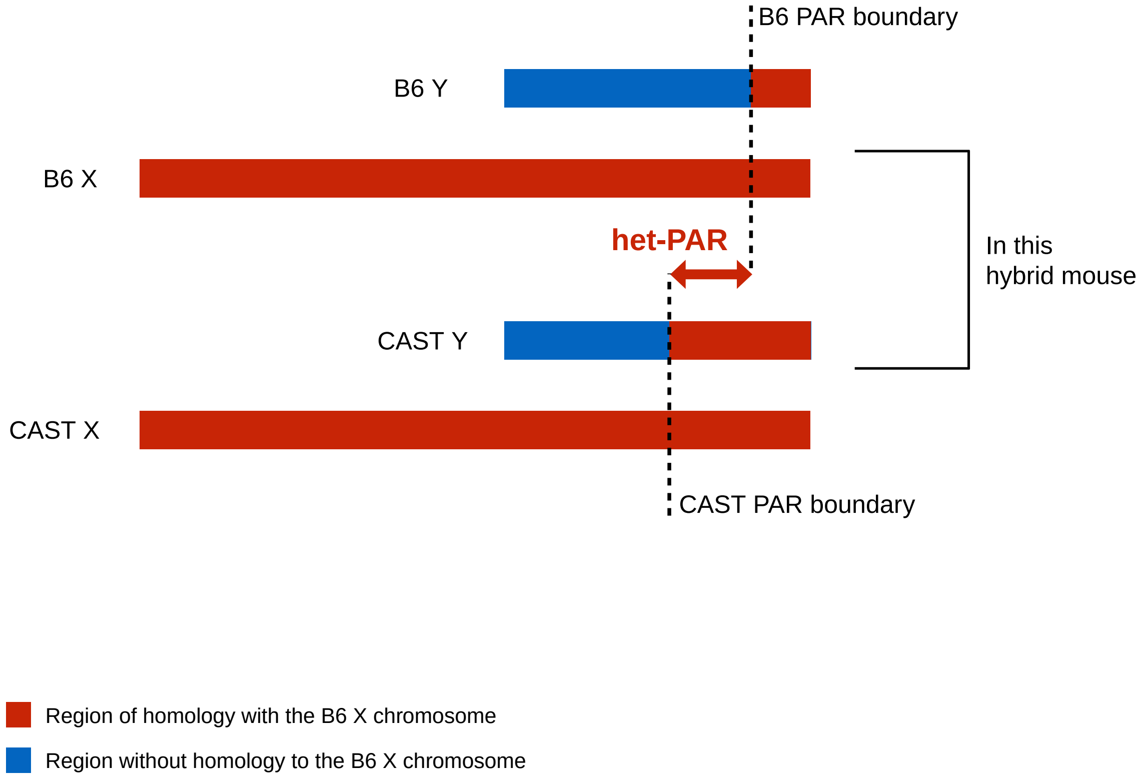

Figure S39: A schematic diagram of the B6 and CAST X and Y chromosomes (sizes are not to scale). The hybrid mouse in this study has a B6 mother and CAST father. The B6 PAR is approximately 700 kb long. The PAR is 430 kb longer in CAST, which creates a region that is PAR in CAST but not in the B6 lineage (marked het-PAR). This region is homologous with the B6 X chromosome, but not with the B6 Y chromosome.

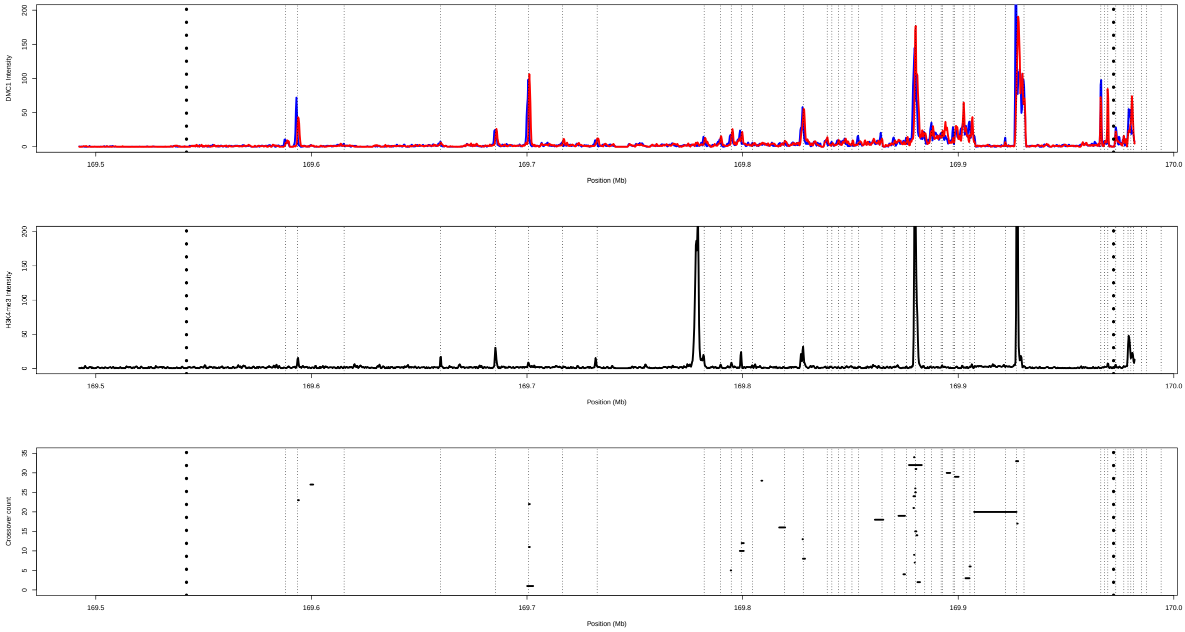

Figure S40: Crossovers in the het-PAR. (Top) DMC1 in the PAR with reads on the forward strand (blue) and reverse strand (red). The thick dotted lines represent the CAST PAR boundary to the left and the B6 PAR boundary to the right. Regions that were identified as DMC1 hotspots are marked with thin dottted lines. (Middle) As above, but with H3K4me3. (Bottom) Horizontal black lines show regions that include the crossover breakpoints identified in the het-PAR.

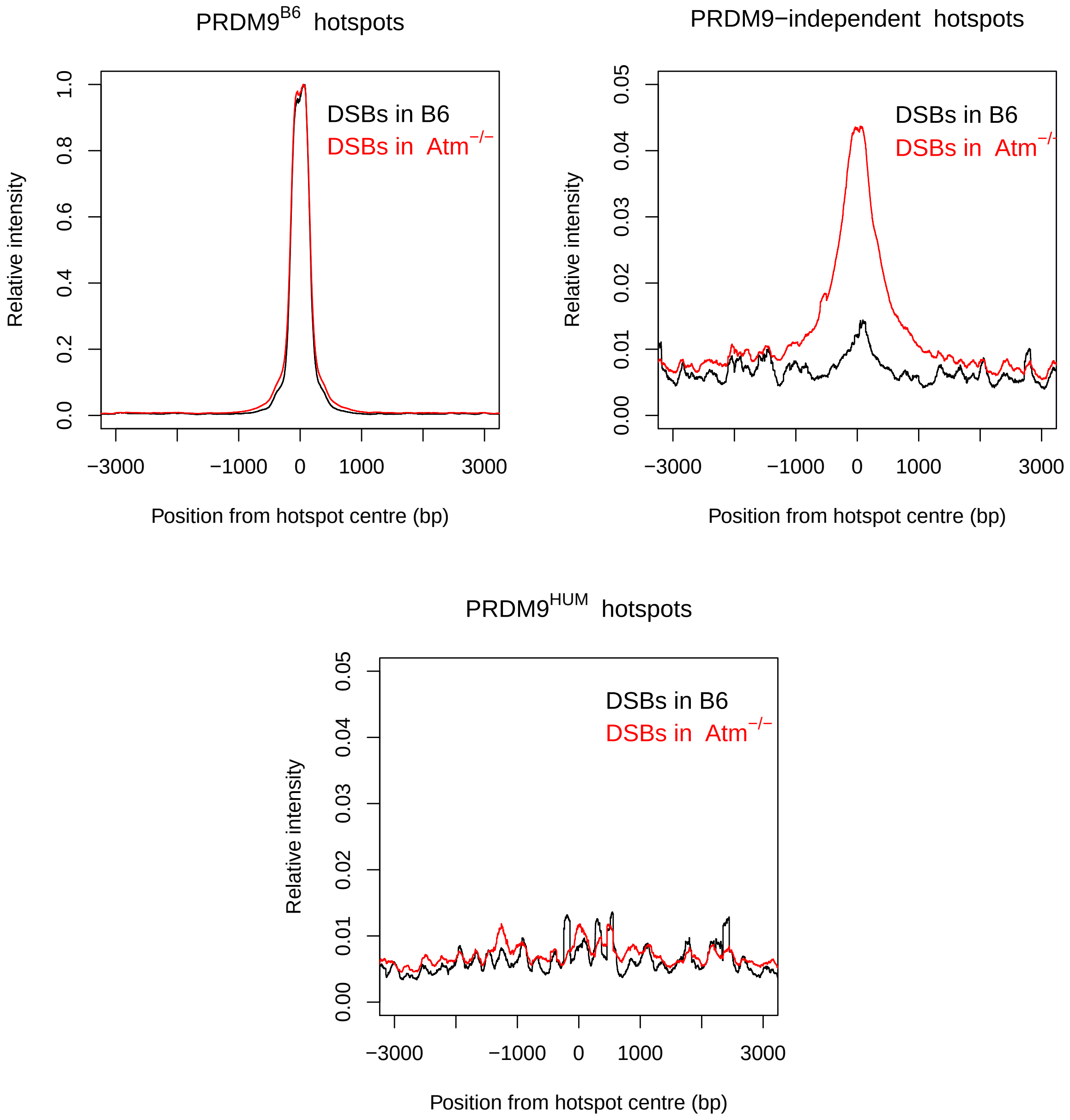

Figure S41: PRDM9-independent hotspots show a localised increase in DSBs in *Atm*$^{-/-}$ mice, over and above any general increase in background rates. Here we show a comparison of DSBs as measured by SPO11-oligos in a B6 wild-type mouse relative to an *Atm*$^{-/-}$ mouse (using data from *(29)*). (Top left) The majority of breaks still happen in PRDM9^{B6} hotspots in both mice genome-wide. All curves were re-scaled such that the average peak intensity at PRDM9^{B6} hotspots is 1 for both mice, to facilitate comparison. (Top right) There is a ∼4-fold increase in the intensity of breaks in PRDM9-independent hotspots in the *Atm*$^{-/-}$ relative to the B6 mouse (Bottom) Comparison of DSBs at PRDM9^{HUM} hotspot locations. These hotspots are not active in either mouse, and are presented as a background control.

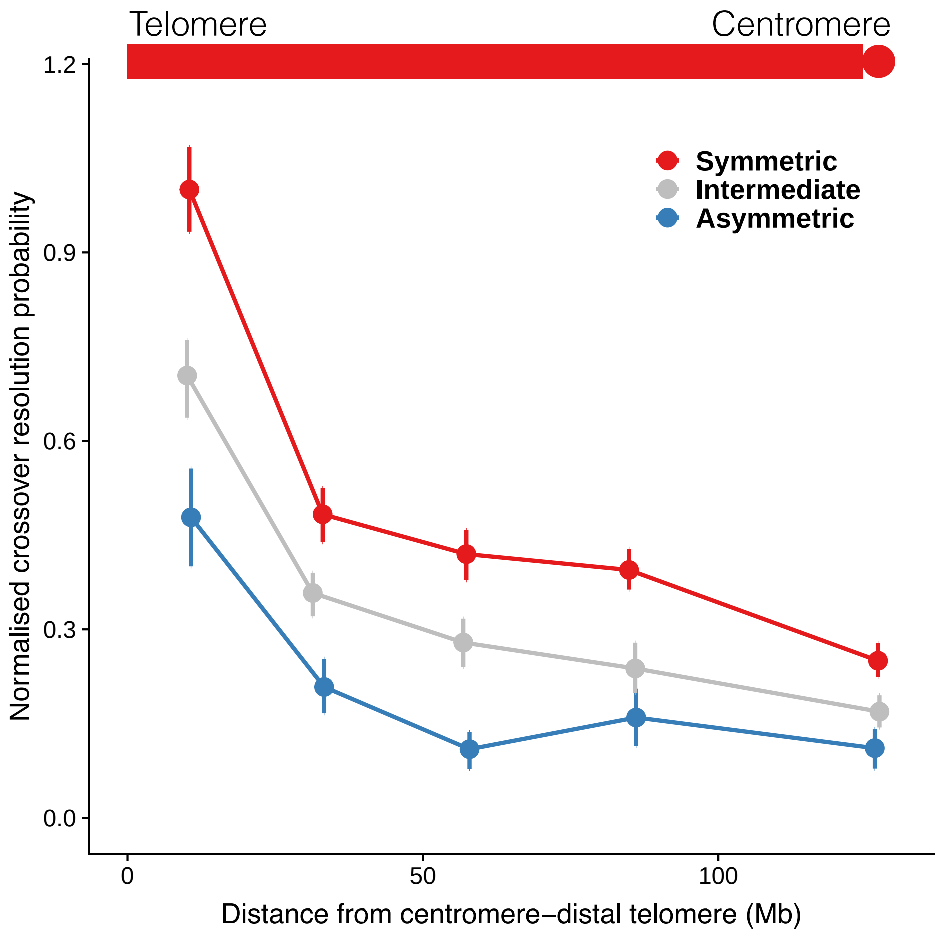

Figure S42: The effects of telomere-proximity and PRDM9 binding on the template on crossover formation are cumulative. Here we show crossover resolution probability in symmetric, asymmetric and intermediate hotspots (5-equal sized bins per category, all scaled relative to the average for the leftmost symmetric bin) against distance of the hotspot from its centromere-distal telomere (bars show 1 standard error). Hotspots with evidence of PRDM9-independent H3K4me3 were excluded.
Symmetric hotspots near the telomere show the highest crossover resolution, while asymmetric hotspots away from the telomere show the lowest degree of crossover resolution. The effects also act in a compensatory manner: asymmetric hotspots *near* the telomere have greater crossover resolution than symmetric hotspots *away* from the telomere.

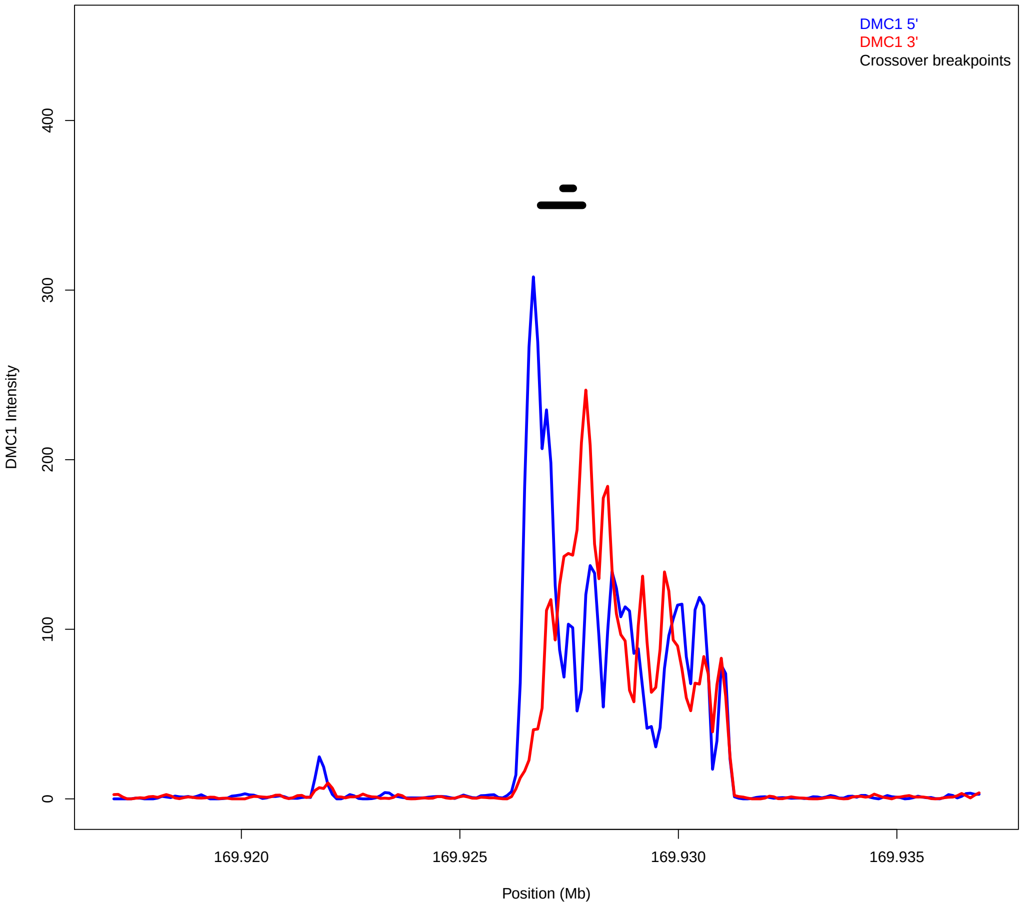

Figure S43: A hotspot in the PAR with 5% sequence divergence between B6 and CAST chromosomes (25 bases among the central 500 bases differ), has crossovers. DMC1 intensity (forward strand in blue, reverse strand in red) and crossover breakpoint locations in each sperm (black bars) are shown. The heterozygosity in this hotspot is 7.5 times the average heterozygosity between the two genomes, and 6-fold the median heterozygosity across all hotspots.

	Heterozygosity	Asymmetry	Heterozygosity conditional on asymmetry	Asymmetry conditional on heterozygosity
± 50 bp	0.10	2×10^{-13}	0.4	3×10^{-13}
± 100 bp	0.06	2×10^{-13}	1.0	8×10^{-13}
± 250 bp	0.01	2×10^{-13}	0.2	3×10^{-12}
± 400 bp	0.01	2×10^{-13}	0.2	2×10^{-12}

Table S1: This table shows p-values of the association between heterozygosity and PRDM9 binding asymmetry with crossover resolution probability. Heterozygosity is defined as the number of SNPs in different window sizes around the hotspot centre (as defined by the PRDM9 binding motif). Columns 1 and 3 report the p-values of the association of heterozygosity with crossover resolution probability with and without including asymmetry in the model, respectively *(25)*. Columns 2 and 4 report the p-values of the association of asymmetry with crossover resolution probability with and without including heterozygosity in the model, respectively. In all of these tests, heterozygosity is not significant in predicting crossover resolution once asymmetry is introduced in the model. In contrast, asymmetry continues to be highly significant.

	PRDM9$^{\text{CAST}}$	PRDM9$^{\text{HUM}}$	Total
Without crossover	1086 (52%)	506 (46%)	1592
With crossover	987 (48%)	605 (54%)	1592
Total	2073	1111	

Table S2: Effect of PRDM9 variant on crossover outcome. Here we show a comparison of the number of PRDM9$^{\text{CAST}}$ and PRDM9$^{\text{HUM}}$ hotspots in matched pairs of hotspots with and without crossover, after matching for H3K4me3 on both homologues and the autosome on which they occur ($n = 1592$, *(25)*). The percentages of hotspots with and without crossover amongst the hotspots for each PRDM9 variant are shown in parentheses. Only hotspots which are PRDM9-dependent, and lacking evidence of PRDM9-independent H3K4me3 were included.

In both sets (with and without crossover), the number of PRDM9$^{\text{CAST}}$ hotspots is greater than PRDM9$^{\text{HUM}}$ hotspots, which reflects the dominance of PRDM9$^{\text{CAST}}$ over PRDM9$^{\text{HUM}}$ (see main text). However, the proportion of PRDM9$^{\text{HUM}}$ hotspots that have crossovers is greater than the corresponding proportion for PRDM9$^{\text{CAST}}$ hotspots (54% vs 48%). (Odds of crossover in PRDM9$^{\text{HUM}}$ hotspots $= 605/506 = 1.196$, odds of crossover in PRDM9$^{\text{CAST}}$ hotspots= $987/1086 = 0.909$, Odds ratio $(OR) = \frac{1.196}{0.909} = 1.32$, 95% CI= $[1.13, 1.53]$, $p = 2.67 \times 10^{-4}$, Fisher's exact test).

Table S3A

	$\text{PRDM9}^{\text{CAST}}$	$\text{PRDM9}^{\text{HUM}}$	Total
Without crossover	585 (52%)	228 (45%)	813
With crossover	530 (48%)	283 (55%)	813
Total	1115	511	

Table S3B

	$\text{PRDM9}^{\text{CAST}}$	$\text{PRDM9}^{\text{HUM}}$	Total
Without crossover	521 (52%)	295 (47%)	816
With crossover	487 (48%)	329 (53%)	816
Total	1008	624	

Table S3: As in Table S2, but with crossovers split into two bins – crossovers originating from the more active hotspots (Table S3A) and crossovers originating from the less active hotspots (Table S3B). The effect size is greater for more active hotspots ($n = 813, OR = 1.37, 95\%\ CI = [1.10, 1.70], p = 0.004$) relative to less active hotspots ($n = 816, OR = 1.19, 95\%\ CI = [0.97, 1.46], p = 0.09$).